STELLINGEN

behorende bij het proefschrift

Constitutive modelling of the large strain behaviour of rubbers and amorphous glassy polymers

door

Wu Pei-Dong

1. Phenomenological models for rubber elasticity have the distinct advantage of being relatively easy to implement in numerical analyses of large strain problems. However, they bear no relationship to the actual deformation mechanisms on the macromolecular level. For this purpose, non-Gaussian network models for rubber elasticity are required.

2. If the number of links *N* in a molecular network is large, the orientation distribution of the individual links with respect to the end-to-end vector has been given by Kuhn and Grun (1942) analytically. Furthermore, a closed-form solution for the molecular chain orientation distribution function (CODF) has been derived by Wu and Van der Giessen (1993). Therefore, it is possible to obtain analytically a so-called Link Orientation Distribution Function (LODF), which would be expected to contain the complete information of the orientation distribution of molecular links at any stage of the deformation.
   Kuhn, W. and Grun, F. (1942). *Kolloidzeitschrift* **101**, 248-271.
   Wu, P.D. and Van der Giessen, E. (1993). *J. Mech. Phys. Solids* **41**, 427-456.

3. The constitutive model available for large strain viscoplastic deformation of amorphous glassy polymers assumes that the orientations of the individual chains affect plasticity only indirectly by introducing a back stress tensor. The predicted flow potential surface maintains its shape during the deformation. However, several observed plasticity phenomena exhibit changes of the shape of this surface during the deformation process. For the description of this phenomena, a network model for polymer plasticity, which accounts accurately for the actual spatial orientation distribution of chains, is required.

4. To some extent, a researcher in mechanics is a translator who translates the knowledge (usually at a microscopic level) provided by material scientists and physicians into mathematical language by developing a constitutive model.

5. In the context of polymer engineering there are different definitions of plasticity. Following G'Sell (1986), we call plastic deformation the component of the total deformation which is not recovered after the material has been unloaded during a time equivalent to the loading duration. This definition is valid provided the time scales for other mechanisms (such as physical aging) are irrelevant to the time scale for plasticity.
   G'Sell, C. (1986). In *Strength of Metals and Alloys.* (Edited by H.J. McQueen *et al.*), pp. 1943-1982, Pergamon Press, Oxford.

6. A torsion test seems to be ideally suited for the experimental determination of material parameters in the range of large strains. The behaviour in torsion is sufficiently sensitive to the constitutive assumptions of the analysis to be capable of discriminating among candidate constitutive models.

7. The elegant simple shear test carried out by G'Sell and co-workers [see e.g. G'Sell and Gopez, 1985] showed initiation and propagation of a shear band. The intrinsic softening is the driving force to promote initiation of the shear band and its propagation in the shear direction, while the orientation hardening is the driving force for widening of the shear band.

   G'Sell, C. and Gopez, A.J. (1985). *J. Mat. Sci.* **20**, 3462–3478.

8. In a tensile test, orientation hardening is the driving force to promote neck propagation along the specimen; the intrinsic softening is a sufficient condition for necking, but not necessary.

9. Not all complicated mechanical problems have to be solved by using complicated tools. The most important thing is that a solver understands his problem and has a very clear physical picture of his problem in his mind.

10. Finding a good student for mechanics is even more difficult than mechanics itself.

CONSTITUTIVE MODELLING OF THE LARGE STRAIN BEHAVIOUR OF RUBBERS AND AMORPHOUS GLASSY POLYMERS

CONSTITUTIVE MODELLING OF THE LARGE STRAIN BEHAVIOUR OF RUBBERS AND AMORPHOUS GLASSY POLYMERS

PROEFSCHRIFT

ter verkrijging van de graad van doctor
aan de Technische Universiteit Delft,
op gezag van de Rector Magnificus Prof. ir. K.F.Wakker,
in het openbaar te verdedigen ten overstaan van een commissie,
door het College van Dekanen aangewezen,
op maandag 25 april 1994 te 10.30 uur

door

PEI-DONG WU,

Master of Science,

geboren te Jiangyin, Jiangsu Province, China.

Dit proefschrift is goedgekeurd door de promotor:
Prof. dr. ir. E. van der Giessen

CIP-DATA KONINKLIJKE BIBLIOTHEEK, DEN HAAG

Wu, Pei-Dong

Constitutive modelling of the large strain behaviour of rubbers and amorphous glassy polymers /
P.D. Wu. - Delft: Delft University of Technology,
Faculty of Mechanical Engineering and Marine Technology. -Ill.
Thesis Technische Univeristeit Delft. - With ref. - With summary in Dutch.
ISBN 90-370-0099-1
Subject headings: large strain constitutive modelling /
rubbers / polymers.

To Ruibo & Xiaoyu

To my parents & my old aunt

ACKNOWLEDGEMENTS

I would like to gratefully acknowledge my supervisor Professor Erik van der Giessen for his comprehensive guidance, numerous discussions and constant encouragement as well as his helping me to get accustomed to working and living in The Netherlands.

My sincere gratitude is also due to Professor Z.D. Chen (China University of Mining and Technology, Beijing), who introduced me to nonlinear continuum mechanics.

Also, I would like to direct acknowledgments to Professors J.F. Besseling and P. Meijers (Delft University of Technology), Professor Wang Ren (Peking University), Professor Kenneth W. Neale (University of Sherbrooke, Canada), Professor C. G'Sell (University of Nancy, France) and Professor L.C.E. Struik (DSM research), for their interest and encouragement during the study.

The partial financial support provided by DSM research, Geleen is acknowledged.

Finally, I am profoundly grateful my wife, my parents and my old aunt for their ungrudging support. I am greatly indebted to my daughter, especially when writing has frequently overrun into time which I should have been spent with her.

SUMMARY

This thesis considers two subjects concerning constitutive modelling of large-strain behaviour of polymeric materials, namely large-strain elastic deformation of rubbers and large-strain inelastic deformation of amorphous glassy polymers.

Three-dimensional molecular network theories are studied which use a non-Gaussian statistical mechanics model for the large strain extension of molecules. Invoking an affine deformation assumption, the evolution of the network—consisting of a large number of molecular chains per unit volume, which are initially randomly oriented in space—is shown to be governed by a balance equation in orientation space. Eulerian and Lagrangian type formulations of these balance equations are given, and the closed-form analytical solution for the so-called Chain Orientation Distribution Function is derived. This full network model is then used to describe the large-strain elastic hehaviour of rubbers. Detailed comparisons with experimental results and with two approximate models, namely the classical three-chain model and a very recently proposed eight-chain model, are provided for different types of deformation and rubbers.

Furthermore, the full network model for rubber elasticity is re-formulated in a more efficient and more micromechanics motivated manner. Based on such a full network description, a so-called full network model for rubber photoelasticity is proposed, by introducing directional polarizabilities into the individual links of the idealized randomly-jointed chain. This optical theory can be used to study the optical properties or birefringence-strain behaviour of rubbers in arbitrary 3-D deformation states. Detailed comparisons with two approximate models, namely the classical three-chain model and a so-called eight-chain model for rubber photoelasticity, which is also developed in this thesis, are provided for different types of deformation. The predicted numerical results are compared with experimental data found in the literature.

The network model is further applied to describe the orientation hardening in amorphous glassy polymers caused by stretching of the entanglement network. A 3-D constitutive model is then developed to describe the large strain inelastic deformation behaviour of amorphous glassy polymers, featuring time-, temperature- and pressure-dependent yield, softening and subsequent orientational hardening.

Large-strain elastic-viscoplastic torsion of circular tubes and solid bars of glassy polymers is investigated under fixed-end as well as free-end conditions. The solution of the problem is obtained numerically by means of simple, special purpose finite elements. The differences between free-end and fixed-end torsion are emphasized. Numerical results predicted by the model are compared with experimental results for polycarbonate found in the literature.

Neck propagation, or commonly termed cold drawing, is a standard technique used to orient the molecular chains of the polymers and thereby harden the polymer products. Finite element analysis is used to numerically simulate plane strain tension, focussing attention on necking and neck propagation. The effects of initial imperfection, strain softening, orientation hardening, strain-rate as well as the geometry and boundary conditions are discussed in detail.

The mechanisms of necking and neck propagation are discussed in some detail based on the detailed parameter study.

Similar to the well-known neck propagation phenomenon, shearing of polymer materials often reveals the initiation and subsequent propagation of a shear band. Finite element analysis is used to numerically simulate large plane strain, simple shear tests, focussing attention on the initiation and propagation of the shear band. The mesh sensitivity and effects of initial imperfection, strain softening, orientation hardening, strain-rate as well as the edge effects are discussed in detail. It appears that the intrinsic softening is the driving force to promote initiation of the shear band and its propagation in the shear direction, while the orientation hardening is the driving force for widening of the shear band. The predicted numerical results are compared with experimental data for polycarbonate found in the literature.

This thesis is based on the following publications:

Chapter 2. Wu, P.D. and Van der Giessen, E. (1993). On improved network models for rubber elasticity and their applications to orientation hardening in galssy polymers. *Journal of the Mechanics and Physics of Solids* **41**, 427-456.

Chapter 3. Wu, P.D. and Van der Giessen, E. (1993). On network descriptions of mechanical and optical properties of rubbers. *Philosophical Magazine* (submitted for publication).

Chapter 4. Wu, P.D. and Van der Giessen, E. (1993). On large-strain inelastic torsion of glassy polymers. *International Journal of Mechanical Sciences* **35**, 935-951.

Chapter 5. Wu, P.D. and Van der Giessen, E. (1993). Analysis of shear band propagation in amorphous glassy polymers. *International Journal of Solids and Structures* (in print).

Chapter 6. Wu, P.D. and Van der Giessen, E. (1993). On neck propagation in amorphous glassy polymers under plane strain tension. *International Journal of Plasticity* (submitted for publication).

Contents

Chapter 1

General Introduction

Many industrial and commercial products manufactured from polymers are done so in the solid state by relatively 'cold' mechanical forming processes such as extrusion, deep drawing and blow molding. These processes involve large to very large local deformations in the solid state which give rise to a very significant texture in the final product. This allow us for the manufacturing of so-called self-reinforced polymers. The design of such a forming process for a certain product is usually based on an expensive and time-consuming trial-and-error procedure. The main reason for this is that the material behaviour of the polymers used at large deformations is not yet adequately understood or characterized for 3-D deformation processes. A mathematical description of such behaviour in terms of constitutive models which include the effects of texture development is essential for a reliable simulation of the forming processes as well as for the prediction of the mechanical properties of the final product.

Discussions of the mechanical properties of solid polymers often contain two interrelated objectives. The first of these is to obtain an adequate macroscopic model of the particular aspect of polymer behaviour under consideration. The second objective is to seek an explanation of this behavior in molecular terms, which may include details of the chemical composition and physical structure.

It is difficult to classify polymers as particular types of materials such as a glassy solid or a viscous liquid, since their mechanical properties are so dependent on the conditions of testing, e.g. the rate of application of load, temperature, amount of strain. In fact, a polymer can show features of a glassy, brittle solid or of an elastic rubber or of a viscous liquid depending on the temperature and time scale of measurement. Polymers are usually referred to as viscoelastic materials, but it should be realized that this is only a generic term which emphasizes there intermediate position between viscous liquids and elastic solids. At low temperatures or high strain rates, a polymer may be glass-like with a Young's modulus E of 10^9 - 10^{10} Nm^{-2} and will break or flow at strains of around 5%. At high temperatures or low strain rates, the same polymer may be rubber-like with a modulus of 10^6 - 10^7 Nm^{-2} withstanding large extension without permanent deformation. At still higher temperatures, permanent deformation occurs under load, and the polymer behaves more like a highly viscous liquid. In an intermediate temperature range, commonly called the glass transition range, the polymer is neither glassy nor rubber-like. It shows an intermediate modulus, is viscoelastic and may dissipate a considerable amount of energy during straining.

In terms of microstructure, polymers can be divided into amorphous and semi-crystalline solids. The amorphous ones are glassy up to a temperature called the glass transition temperature T_g, whereupon they change into a rubbery material, the viscosity of which falls as the temperature is raised further. Amorphous polymers are usually considered to be a random tangles of molecules. Polycarbonate (PC), Polymmethyl Methacrylate (PMMA), Polystyrene (PS) and Polyvinyl Chloride (PVC) are the most popular amorphous polymers. Semi-crystalline polymers can be regarded as two phase materials, with an amorphous phase, and a crystalline phase with a melting temperature T_m. Polyethylene (PE) is a typical semi-crystalline polymer.

Although semi-crystalline polymers are of considerable industrial interest, their properties are those of composite materials and thus depend, in a complex way, on the elementary properties of their constitutive phases, which are necessary to be first characterized separately. The aim of this study was originally was the constitutive modelling of large plastic deformations of amorphous polymers. Such constitutive modelling has a dual significance. On one hand, the search for basic plastic deformation mechanisms in amorphous polymers is of conceptual importance. In contrast to crystalline materials where the relation between plasticity and crystal lattice dislocations is well established and in many cases can be observed directly, the deformation mechanisms in amorphous solids are not yet well understood. On the other hand, large to very large local plastic deformations are involved in many mechanical forming processes and it is of considerable importance to determine the intrinsic constitutive equations for large plastic deformation of polymers.

During the study of large plastic strain behaviour of amorphous polymers, we have become deeply involved in the development of network models for rubber elasticity. The effort is animated by two lines of motivations. On one hand, the distortion of the microstructure of an initially isotropic amorphous polymer during large plastic deformations is very similar to that of rubber. The so-called orientation hardening behaviour observed in large plastic deformations of amorphous glassy polymers could be simulated in terms of the network models for rubber elasticity as suggested by Harward and Thackray (1968). On the other hand, the available network models for rubber elasticity at that time were not able to pick up some aspects of large strain behaviour observed experimentally.

This thesis considers two subjects concerning constitutive modelling of large-strain behaviour of polymeric materials, namely large-strain elastic deformation of rubbers and large-strain inelastic deformation of amorphous glassy polymers. For a general discussion of deformation of polymers we refer to Treloar (1975), Ferry (1980), Ward (1983) and Struik (1990).

Each chapter of this thesis, except for this chapter, is an independent paper, which has been published or submitted to an international journal for publication. However, we shall use a uniform layout and referencing system throughout the thesis, with all references collected at the end.

1.1. NETWORK MODELS FOR RUBBER ELASTICITY AND RUBBER PHOTOELASTICITY

Rubber elasticity has been studied extensively for more than 100 years. Various constitutive models have been proposed. Most of them are phenomenological models, which have been successfully used in engineering designs (see e.g. Ogden, 1984). Phenomenological models have the distinct advantage of being relatively easy to implement in numerical analyses of large strain problems. However, they bear no relationship to the actual deformation mechanisms on the macromolecular level. For this purpose, non-Gaussian network models for rubber elasticity are required.

1.1.1. Network models for rubber elasticity

The present understanding of mechanical behaviour of amorphous polymers owes much to early advances in the network theory of rubber elasticity [see e.g. Kuhn and Grun, 1942; Treloar, 1975]. These theories are based upon the concept of a network of chains of randomly oriented rigid links that are connected at junction points which in rubber-like materials are provided by the chemical cross-links between macromolecules (see Fig. 1.1). Furthermore, these network theories use a so-called affine deformation scheme, which is based on two key assumptions: (*i*) Statistical fluctuations of the position of the junction points about their mean position can be neglected, (*ii*) the end-to-end vector of a chain between junction points co-deforms with the local deformation of the continuum it is embedded in. According to this scheme, as deformation progresses each chain stretches while rotating towards a preferred direction. At all stages each chain attempts to maximize its entropy by disorienting the elements or random links, subject only to the constraints imposed by the end-to-end vectors. Another important assumption involved in these network models is that intermolecular interactions are negligible in comparison to intramolecular effects. The overall properties of the network are then obtainable by simply summing the contributions of the individual chains. Furthermore, the exact non-Gaussian treatments of a single chain, both for mechanical and optical behaviour, are available (developed originally by Kuhn and Grun, 1942; and James and Guth, 1943). However, exact treatment of the transition from an individual chain to network behaviour is very difficult owing to its mathematical complexity. In principle, this transition (through an averaging process) needs the orientations of the individual chains of the network, which was not available for arbitrary 3-D deformations until very recent (see Chapter 2).

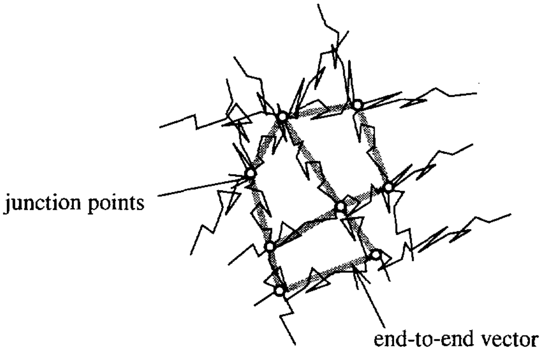

Fig. 1.1. Schematic representation of a macromolecular network of rubbers.

Various simplified averaging procedures to obtain the network response have been proposed (see Chapter 2). Among these simplified models, the so-called three-chain model, originally suggested by James and Guth (1943), has become the most widespread and almost standard non-Gaussian network model for rubber elasticity. This model assumes that a network containing n chains per unit volume is equivalent to three independent sets of $n/3$ single chains in three orthogonal directions (see Fig. 2.3a). Thus, the actual spatial distribution of chains is sampled in three orthogonal orientations. Similarly, Treloar (1946) proposed the idea of a four-chain Gaussian network representation (Flory and Rehner, 1943) to sample four spatial chain orientations. Very recently, Arruda and Boyce (1991, 1993a) proposed a so-called eight-chain model, which considers a set of eight chains connecting the central junction point and each of the eight corners of the unit cube (see Fig. 2.3b). Obviously, these models are but approximate representations of the actual spatial distribution of molecular chains. All these models can be regarded to sample a set of particular directions among all possible orientations. As a consequence, the three-chain model would overestimate the contribution of the chain collection oriented along the direction of major principal extension, while the eight-chain model would underestimate the stiffness of the network (Dahoun *et al.*, 1993). The four-chain model does not exhibit the symmetry required of the principal strain space (Arruda and Boyce, 1991). Furthermore, the accuracy of these approximations has not been established until very recently (see Chapter 2).

The full network formulation to be presented in Chapter 2 accounts accurately for the actual spatial orientation distribution of molecular chains. Treloar and Riding (1979a) had already developed a rubber elasticity theory based on such a full network description, but their considerations were limited to deformations with biaxial extension along fixed axes under plane stress conditions. The model proposed in Chapter 2 extends the theory of Treloar and Riding (1979a) to a general formulation valid for 3-D deformation processes. The modelling centres around a general treatment of the orientation distribution of molecular chains and their evolution as deformation progresses. This description utilizes the idea of Chain Orientation Distribution Function (CODF), which is governed by balance equations that express physically well-understood conservation features. Assuming the network to deform affinely with the deformation of the continuum it is embedded in, closed-form solutions are derived for this CODF, which thus contain the complete information of the orientation distribution of molecular chains at any stage of the deformation. This solution is then used to develop the rubber elasticity model by averaging out the contribution to the free energy of individual chains over all chain orientations. The model has been found to be able to pick up the mechanical behaviour of rubbers at various different large deformations (see Chapter 2; Dahoun, 1992; Wu *et al.*, 1993). Furthermore, it has been demonstrated that, the stress response predicted by the full network model is for the same values of the material parameters N and C^R always in between that predicted by the three-chain model and eight-chain model, respectively (see Wu and Van der Giessen, 1992a and Chapter 2).

In Chapter 3, we re-formulate the full network model for rubber elasticity in a more efficient and more micromechanics motivated manner. The so-derived equations are mathematically equivalent to those given in Chapter 2. But, the new representation of the model allows us to avoid calculating principal stretches and principal directions of deformations. Furthermore, this micromechanics motivated new derivation will turn out to be convenient for further development of the so-called full network model for rubber photoelasticity as demonstrated in Chapter 3.

The limitations of the network models for rubber elasticity are also discussed in some detail in Chapter 2.

1.1.2. Network models for rubber photoelasticity

The development of molecular chain segment orientation in rubber-like materials under deformation has been extensively studied experimentally, often by the optical anisotropy or birefringence [see e.g. Treloar, 1975; Brown and Windle, 1984; Mitchell *et al.*, 1985].

It is well-known that many materials show the phenomenon of double refraction, which arises from the fact that they are optically anisotropic. In other words, they have different refractive indices, or polarizabilities in different directions. The refractive index of a material is a function of its response to the electric field in the light wave, or, more specifically, of its polarizability, which is defined as the induced dipole moment per unit field strength. Rubber-like materials are usually assumed to be random in their structure and isotropic in their physical properties; such materials do not show double refraction in the initial undeformed state. But in the deformed state, their structures are no longer random; they cease to be isotropic and begin to show double refraction or birefringence.

Usually, the development of a network model for rubber photoelasticity follows closely the lines taken in the treatment of the corresponding network model for rubber elasticity. The actual macromolecule is replaced by a chain of randomly jointed equal links. The optical properties are introduced by assuming that each link has a polarizability α_1 in the direction of its length and a mean polarizability α_2 in the transverse directions. Suppose each chain, having n links each of length l, be held with its ends separated by a end-to-end vector distance r. The resultant polarizability γ_1 in the direction of its end-to-end vector and the mean polarizability γ_2 in the transverse directions, for a whole chain, can be calculated from the statistical distribution of link angles. Finally, the so-called total polarizability tensor **B** of the network is obtained by averaging out over all chains.

The polarizabilities of a material may be efficiently represented by a polarizability ellipsoid whose principal axes represent the values of the three principal polarizabilities, $\tilde{B}_i$, or alternatively, by a refractive index ellipsoid, whose principal axes are similarly oriented and represent the three principal refractive indices $\tilde{\mu}_i$. The conversion of polarizabilities $\tilde{B}_i$ (per unit volume) to refractive indices $\tilde{\mu}_i$ makes use of the Lorentz-Lorenz relation

$$\frac{\tilde{\mu}_i^2 - 1}{\tilde{\mu}_i^2 + 2} = \frac{4\pi}{3}\tilde{B}_i.$$

A so-called non-Gaussian full network model for rubber photoelasticity is proposed in Chapter 3 where the actual averaging out over all chains is carried out in terms of the CODF. Again, Treloar and Riding (1979b) had already developed a non-Gaussian optical theory based on such a full network description; but, just as for the mechanical properties, their considerations were limited to deformations with biaxial extension along fixed axes under plane stress conditions. Our model extend the theory of Treloar and Riding (1979b) to a general formulation valid for 3-D deformation processes. For the purpose of comparison, we also give two simplified optical theories corresponding to the so-called three-chain model [see e.g. Wang and Guth, 1952] and eight-chain model (Arruda and Boyce, 1993a) originally for rubber elasticity.

Before discussing the modelling of viscoplastic deformation in glassy polymers, it is worthwhile to consider more closely the term *plasticity* in polymer physics, since the nonelastic deformation is known to cover a variety of deformation mechanisms in polymers. Following G'Sell (1986), we call plastic deformation the component of the total deformation which is not recovered after the material has been unloaded during a time equivalent to the loading duration. In that sense, it distinguishes itself from viscoelastic component of the deformation which recovers to a major extent under the same conditions.

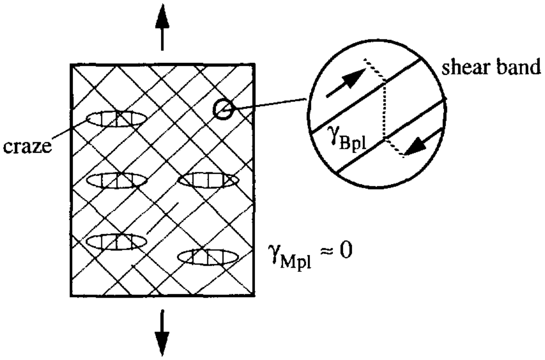

Fig. 1.2. Schematic representation of crazes and shear bands in an amorphous glassy polymer.

Another important distinction is between "discontinuous" and "continuous" forms of plastic deformation. Discontinuous plastic deformation is quite specific to polymers and is represented by the phenomenon of *crazing*, which has been identified by a locally confined mode of extensional plasticity accompanied by a decohension of the polymer. The damaged regions have the shape of flat lenses similar to flaws whose surfaces would be connected by plastically drawn fibrils. This kind of irreversible deformation is particularly favoured by hydrostatic pressure and the crazes are oriented perpendicular to the major principal stress axis (see Fig. 1.2). The other mode of irreversible deformation is *plastic shear*, which is characterized by the conservation of material continuity (no void formation). Due to the very slow diffusion rate of glassy polymer chains, the only deformation mode which is compatible with the continuity requirement is the plane simple shearing of the structure along favourably oriented surfaces. In uniaxial tension or compression, it was observed that plastic deformation tends to localize into oblique shear bands (see Fig. 1.2) in which the local plastic shear γ_{Bpl} is very high, while the shear strain γ_{Mpl} in the rest of the matrix remains nearly zero. In the present thesis, we will consider only this continuous plastic deformation mode and we shall do so within a macroscopic framework. In effect, we shall employ a continuum description in which the microscopic shearing is "smeared out" in the continuum sense, assuming that a material element represents a sufficiently large sample of polymer to allow for statistical averaging to be meaningful.

The microstructure of an initially isotropic amorphous polymer is usually assumed to consist primarily of long molecular chains, which are randomly coiled in space. Side groups protrude from the backbone chains at various locations and, in conjunction with overall chain trajectory, can act as nodes, or points of physical entanglement. This results in a network-like structure much like that of rubber (see Fig. 1.1), but with the chemical crosslinks replaced by physical entanglements.

The yield of initially isotropic glassy polymers has been found to depend on pressure, strain rate, and temperature. After yielding, glassy polymers often strain soften and subsequently strain harden. Following the pioneering work of Haward and Thackray (1968), it is assumed that a glassy polymer must overcome two physical distinct sources of resistance before large strain inelastic flow may occur. Below the glass transition temperature, prior to initial yield, the material must be stressed to exceed its *intermolecular resistance* to segment rotation. Once the material is free to flow, molecular alignment occurs, resulting in an *anisotropic internal resistance* to further inelastic deformation, which is called orientational hardening.

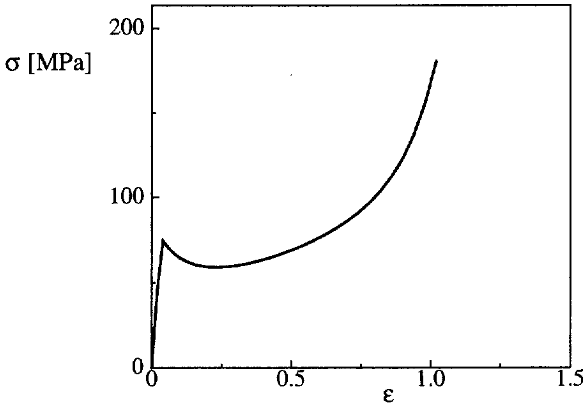

Fig. 1.3. A typical true stress-strain curve of polycarbonate under uniaxial compression.

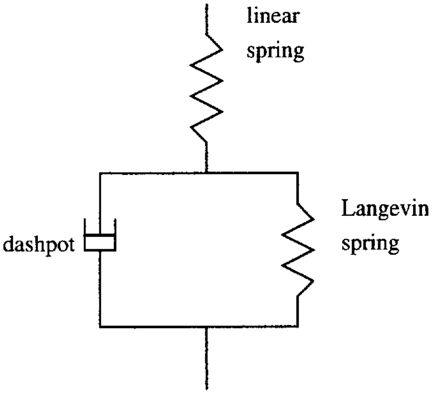

Fig. 1.4. Schematic representation for a 1-D analog to the polymer deformation model.

Figure 1.3 shows a typical stress response to uniaxial compression of polycarbonate at room temperature. To describe these yielding and postyield phenomenon of amorphous glassy polymers, a model requires three elements. These are illustrated schematically in Fig. 1.4. for a 1-D analog to the polymer deformation model. It describes the stress-strain curve in terms of three elements:

(1) A linear spring, which is used to characterize the initial elastic response;

(2) A viscous dashpot, which is used to represent rate and temperature dependent yield and to account for an isotropic resistance to chain segment rotation;

(3) A nonlinear rubber elasticity Langevin spring, which is used to account for the anisotropic resistance to chain alignment.

1.2.1. Modelling of plastic flow

Some early attempts to model the plasticity of glassy polymers were based on modifications of the concepts of viscoelasticity. Thus, the plastic deformability of polymers was first attributed to the heat generated accompanying the deformation which was assumed to raise the temperature above the glass transition temperature. Alternatively, it was suggested that stress-induced free volume would produce the same molecular mobility existing at the glass transition temperature.

One of the earliest quantitative models used to describe the flow of polymers is that due to Eyring (1936). This model assumes that molecular segments are vibrating over an energy barrier (of height E_0) and that the effect of the applied stress is to reduce the height of the barrier for a jump in the forward direction and to increase it for a jump in the reverse direction. It is further assumed that the macroscopic strain rate of the sample is proportional to the net jump rate of the segments in the forward direction.

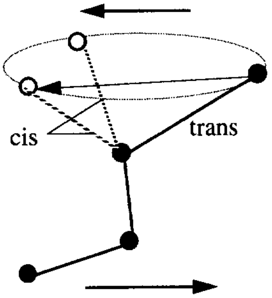

Fig. 1.5. Schematic representation of the different positions of four adjacent atoms in the backbone.

Robertson (1966) has developed a slightly more elaborate version of the Eyring viscosity theory. In a sense, this model is an attempt to express quantitatively the idea that the applied stress causes the molecules to seek a new, more rubber-like conformation and that yield occurs when the conformation becomes similar to that at the glass transition. This model is based on the assumption of a thermodynamic statistical distribution of inflexed and flexed bonds (*trans* and *cis* rotational conformations, respectively): at any time the molecular segments making up the polymer are distributed between a population of cis (high energy) and a population of trans (low energy) conformations (the different positions of four adjacent atoms in the backbone, see Fig. 1.5). The population of cis segments in equilibrium at the glass transition temperature is frozen-in the glassy state; and the effect of applied stress is to cause certain segments to change over from the trans to the cis conformation, increasing the population of cis sufficiently for yield to occur. The model has been extended by Duckett *et al.* (1970) to incorporate the effect of the hydrostatic component of the stress tensor on the yield stress. They suggest that a pressure will increase the energy difference between the cis and trans conformations because a segment in a cis conformation is likely to pack less efficiently and to occupy a larger volume. By making adjustments to all parameters in the modified theory they are able to obtain an excellent fit to yield stress data on PMMA and PET, while keeping the magnitudes of all parameters reasonable. However, in the Robertson theory only intramolecular forces are taken into account; as, in the glassy state, the cohesion of the matter is due to intermolecular forces, it seems necessary to call for models attributing the plastic resistance to intermolecular force.

Argon (1973) has used Li and Gilman's (1970) results to calculate the height of the energy barrier that opposes the flipping-over of a segment of a molecular chain from one position to the next. The two kinks in the chain which form to permit this motion are treated as a pair of disclinations and the energy necessary to form them is calculated (see Fig. 1.6). The resistance to such a double kink formation in a molecule results from the elastic interaction of the molecule with its neighbours, i.e. from intermolecular forces. Later, Boyce *et al.* (1988) have generalized the idealized intermolecular deformation resistance to account for both pressure sensitivity and the true strain softening associated with localized microscopic shear-banding and transient dilation. It should be noted, nevertheless, that the Argon model essentially regards yielding as a nucleation controlled process, analogous to the stress-activated movement of dislocations in a crystal produced by the applied stress, aided by thermal fluctuations. The application of the Eyring theory on the other hand, implies that yield is not concerned with the initiation of the deformation process, but only that the rate of deformation is changed upon stressing until it equals the imposed rate of change of strain (nonlinear viscoelastic model). However, as discussed in detail by Ward (1983), the two approaches of Argon and Eyring cannot be clearly distinguished at the level of fitting to an experimental curve.

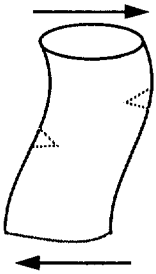

Fig. 1.6. Schematic representation of a pair of disclinations in a molecule.

It could be argued that the Eyring as well as the Robertson model are likely to be appropriate at high temperatures i.e close to T_g, whereas the Argon model is most relevant to the behaviour at low temperatures. Results by Perez (1982) clearly show that a better fit is obtained with the Argon model and the Robertson model at lower and higher temperature, respectively. This corresponds to the evidence that, at low temperature, intermolecular energy barriers, which are at the origin of the cohesion of the glassy solid, are the most important barriers to be overcome; on the other hand, when the temperature approaches T_g, intramolecular forces become more and more dominant.

To sum up, models to describe the yield behaviour of polymers are not yet as firmly based as are, say, models describing the yield strength of metals where the mechanism (dislocation motion) by which changes in the local atomic conformation occur on deformation is well established and in many cases can be observed directly. Models have been proposed that are capable of describing different aspects of the yield behaviour, but so far no accepted unified quantitative treatment exists that can explain all aspects. A more detailed discussion on the above-mentioned models has been given by Wu and Van der Giessen (1991b).

1.2.2. Modelling of orientation hardening

Once the material is stressed to the point of overcoming intermolecular barriers to chain motion, the molecular chains will tend to align along the direction of principal plastic stretch [see e.g. Haward and Thackray (1968) and Argon (1973)]. This action decreases the configurational entropy of the system which, in turn, creates an internal network stress. This process of network distortion is very similar to that of rubber network, and Haward and Thackray (1968) suggested to describe this for uniaxial extension by means of a back stress determined through a Langevin spring (see Fig. 1.4), as suggested by non-Gaussian network theory. Boyce *et al.* (1988) extended this approach to general three-dimensional plastic deformations by introducing a back stress tensor **B** which is taken to be coaxial with the plastic left stretch tensor. Originally, Boyce *et al.* (1988) adopted the classical so-called three-chain model. However, very recently Arruda and Boyce (1991, 1993b) found that the three-chain non-Gaussian network model was not capable of picking up the strain hardening observed experimentally in polycarbonate (PC) and polymethylmetacrylate (PMMA). At the same time, they suggested to model the network by eight equivalent chains instead of three, and obtained more close agreement with their experimental results for PC and PMMA.

In Chapter 2, the full network model for rubber elasticity is used to model the orientation hardening behaviour in large strain deformations of amorphous glassy polymers.

Alternatively, Vest *et al.* (1987) used the phenomenological Mooney-Rivlin rubber elasticity formulation to model the strain orientation hardening. However, the Mooney-Rivlin model is not able to capture the three dimensionality of the strain hardening response of rubber materials at large strains (Arruda and Boyce, 1993a).

1.3. LARGE-STRAIN BEHAVIOUR OF AMORPHOUS GLASSY POLYMERS

To assess the accuracy of the constitutive models, a number of deformation processes in the large strain region are studied numerically and compared with experimental data in Chapters 4-6. Besides the homogeneous uniaxial compression and plane strain compression studied, particular attention is paid to large-strain torsion and localization phenomena such as shear band propagation and neck propagation.

1.3.1. Large-strain torsion

Torsion of cylindrical solid bars in the region of large plastic deformations is of considerable practical interest. In particular, a torsion test seems to be ideally suited for the experimental determination of material parameters in the range of large strains. The major advantage for this purpose over tensile tests is that deformations during torsion remain homogeneous in axial direction until fracture, without showing strain localization in necks etc. A second, slightly more academic interest in large strain torsion relates to recent attempts to incorporate deformation-induced anisotropy into large strain plasticity models. Experiments on polycrystalline metals have shown that texture development, which is the prime source of anisotropy in most materials, leads to elongation of the specimen in the case of free ends or leads to compressive axial stresses in specimens with fixed ends. The prediction of these axial second-order phenomena depend strongly on the constitutive model—in particular the description of anisotropic hardening [see e.g. Neale and Shrivastava, 1990; Van der Giessen *et al.*, 1992a; Harren *et al.* 1989; Wu and Van der Giessen, 1993b]. Thus, the torsion test seems to provide a simple yet effective means for assessing the adequacy of such constitutive models.

Large strain elastic-viscoplastic torsion of circular cylindrical tubes and solid bars under fixed-end as well as free-end conditions is analyzed in Chapter 4, using a numerical method based on a simple, special purpose finite elements. The predicted response of a tube under fixed-end torsion is compared with available experimental data for polycarbonate. The numerical method developed in Chapter 4 is capable of simulating large strain torsion of tubes with any ratio of inner radius to outer radius. Furthermore, it is fairly easy to incorporate other viscoplastic constitutive models into this special finite element program. Therefore, it provides a useful tool to interpret experimental torsion results on thick-walled tubes or solid specimens, and thus to determine the material parameters appearing in the constitutive models.

1.3.2. Plastic instabilities

Localization instabilities in the form of shear bands appear to be almost inevitable when a ductile solid undergoes large plastic flow. Such plastic instabilities have a dual significance; as a precursor to fracture and as a mechanism for further deformation. Developing the ability to predict their onset, evolution and subsequent failure is essential for the control of a variety of manufacturing processes and for the design of material microstructures.

It is now widely acknowledged that glassy polymers exhibit plastic deformation below the glass transition temperature mainly through the activation of microscopic shear bands (see Sec. 1.2). Macroscopic strain localization in polymers can be very different from that in metals due to the dramatic stiffening of polymers at large strains, which is associated with molecular chains orienting and stretching during the deformation process. While plastic instabilities like necks or shear bands in metals almost invariably tend to localize progressively until failure intervenes, necks and macroscopic shear bands in polymers typically do not continue to localize but tend to propagate along the specimen [see e.g. G'Sell *et al.* (1983), Neale and Tugcu (1985), and Buisson and Ravi-Chandar (1990)]. The propagation of localized deformation is fundamental to the processing of polymers since the permanently oriented state generally has enhanced properties, but can also affect subsequent failure. However, the quantitative understanding of thermal-viscoplastic localizations in polymers is still in its infancy.

In Chapter 5, a 2-D finite element analysis has been used to simulate large simple shear tests of amorphous glassy polymers carried out by Gopez and G'Sell (1985), focusing attention on the initiation and propagation of the shear band. The mesh sensitivity and the effects of initial imperfection, strain softening, orientation hardening, strain-rate as well as the edge effects have been discussed in detail. The mechanism of initiation and propagation of the shear bands are discussed in some detail.

Neck propagation, or commonly termed *cold drawing*, is a standard technique used to orient the molecular chains of the polymers and thereby harden the polymer of products such as fibres (axisymmetric deformation) and magnetic tape and sheet materials (plane strain deformations). The phenomenon of neck propagation is in essence a mechanical one, and therefore the problem is usually considered as a quasi-static deformation problem under isothermal conditions.

In Chapter 6, the modified 3-D constitutive model for large strain inelastic deformation of amorphous glassy polymers is incorporated in finite element simulations of the plane strain tension, focusing attention on the initiation of necking and neck propagation along the specimen. The mechanism of necking and neck propagation is discussed based on the detailed analysis of the numerical results.

1.4. THERMODYNAMIC CONSIDERATIONS

Since the deformation mechanisms of rubbers and amorphous polymers are quite different from those of polycrystalline metals and others, the thermodynamic analysis of these materials provides some special features which need to be emphasized here. For the general thermodynamic analysis of deformed solids we refer for instance to Ziegler (1977) and Besseling and Van der Giessen (1993).

1.4.1. Thermodynamics of rubber elasticity

Assume the Helmholtz free energy W per unit mass to be a function of the Lagrangian strain tensor $\mathbf{E}$ and the temperature T, implying that the thermodynamic state of the material can be determined by the current values of a set of state variables $Q = \{\mathbf{E}, T\}$. The entropy χ and the Cauchy stress $\boldsymbol{\sigma}$ are determined through the well-known relations

$$\chi(\mathbf{E}, T) = -\frac{\partial}{\partial T}W(\mathbf{E}, T) , \qquad \boldsymbol{\sigma}(\mathbf{E}, T) = \rho\mathbf{F}\frac{\partial W}{\partial \mathbf{E}}\mathbf{F}^T . \tag{1.1}$$

In above equations ρ is the density of the material after deformation, the superscript T denotes transposition, and $\mathbf{F}$ is the deformation gradient tensor. The internal energy e, again measured per unit mass, is defined as function of $\mathbf{E}$ and T by $e(\mathbf{E}, T) = W + T\chi$. The elimination of W between (1.1) and the definition of e gives

$$\boldsymbol{\sigma} = \rho\mathbf{F}\frac{\partial e}{\partial \mathbf{E}}\mathbf{F}^T - \rho T\mathbf{F}\frac{\partial \chi}{\partial \mathbf{E}}\mathbf{F}^T , \tag{1.2}$$

where it is to be recalled that the partial derivatives with respect to $\mathbf{E}$ are taken at constant temperature. In this form, it is clear that part of the stress in an elastic material arises from changes of internal energy in response to deformation and the remainder from changes of entropy.

In a wide range of solids with ordered microstructure the stress is primarily due to the distortion of the intermolecular potential fields, resulting in a change of internal energy. The right-hand side of equation (1.2) is then dominated by the first term. In contrast, intermolecular forces in high density polymer are substantially unaffected by isochoric deformation and the stress arises mainly from the tendency of the chain molecules to randomize the conformations available to them so as to maximize the entropy (see Sec. 1.1.1). The right-hand side of (1.2) is then governed by the second term. The resulting model of material behaviour is known as the entropic model, a full discussion of which can be found in Chadwick and Creasy (1984). The network models for rubber elasticity discussed in this thesis are of this form. Under the assumption of mechanical incompressibility, the stress tensor in a network model for rubber elasticity is then determined by

$$\boldsymbol{\sigma} = -\rho T \mathbf{F} \frac{\partial \chi}{\partial \mathbf{E}} \mathbf{F}^T - p\mathbf{I}, \tag{1.3}$$

where p must be determined from the boundary conditions.

1.4.2. Thermodynamics of inelastic deformation in glassy polymers

The concept of an intermediate configuration or relaxed configuration is a well-understood tool in finite deformation plasticity theories. Different precise definitions and interpretations aside, the deformation gradient may be multiplicatively decomposed into elastic and plastic parts, $\mathbf{F} = \mathbf{F}^e \mathbf{F}^p$, so that $\mathbf{F}^p$ represents the mapping from the initial to the relaxed configuration. The plastic properties in the relaxed configuration may be subject to change during the deformation process as monitored by a set Q^p of appropriate hidden state variables. The changes with respect to the relaxed configuration being characterized by the set $Q^e = \{\mathbf{E}^e, T\}$, here $\mathbf{E}^e$ is the elastic Lagrangian strain tensor. The actual current thermodynamic state is then defined by the union $Q^e \cup Q^p$. Since thermoelasticity and inelasticity are of a physically totally different nature, we will regard them as uncoupled processes specified by disjunct sets Q^e and Q^p. The free energy in the relaxed configuration is not zero, but has a value that is at any instant determined by the past inelastic deformation history as represented by Q^p. Confining attention to the free energy representation, this value is termed the stored plastic energy, W^p. The free energy in the current state is now given by

$$W = W^e(\mathbf{E}^e, T) + W^p. \tag{1.4}$$

Generally, the stored plastic energy W^p is not a point function of the state variables in Q^p but merely depends on the path history represented by Q^p. Therefore, W^p is usually defined through its evolution during the deformation process (Besseling and Van der Giessen, 1993). However, the plastic properties (such as orientational hardening) of amorphous glassy polymers can be determined from the current plastic stretches through a network model for rubber elasticity [see e.g. Haward and Thackray (1968) and Argon (1973)]. Therefore, we assume the plastic stored energy W^p to be a function of $\mathbf{C}^p$ ($\mathbf{C}^p = \mathbf{F}^{pT}\mathbf{F}^p$) and temperature T, i.e. $W^p = W^p(\mathbf{C}^p, T)$. Note that $\mathbf{C}^p$ is invariant under rigid-body rotations. We further compose the total entropy into thermal entropy χ^t and configurational entropy χ^p, i.e. $\chi = \chi^t + \chi^p$. The rate of change of W^e and W^p can be written as

$$\dot{W}^{e} = \frac{\partial W^{e}}{\partial \mathbf{E}^{e}} \cdot \dot{\mathbf{E}}^{e} + \frac{\partial W^{e}}{\partial T}\dot{T},$$

$$\dot{W}^{p} = \frac{\partial W^{p}}{\partial \mathbf{C}^{p}} \cdot \dot{\mathbf{C}}^{p} + \frac{\partial W^{p}}{\partial T}\dot{T} \equiv \frac{1}{\rho}\mathbf{B} \cdot \mathbf{D}^{p} + \frac{\partial W^{p}}{\partial T}\dot{T}, \tag{1.5}$$

respectively, where $\mathbf{D}^{p}$ is the plastic strain rate tensor, $\mathbf{B}$ is the so-called back stress tensor acting on the Langevin spring (see Fig. 1.4), and ($\cdot$) denotes the scalar product.

From the first law of thermodynamics (stating the law of conservation of energy), using the second law in the form known as the Clausius-Duhem inequality and taking into account the equilibrium equations, we arrive at the local inequality for the so-called rate of energy dissipation:

$$T\rho\omega = -\operatorname{grad}T \cdot \dot{\mathbf{h}} + \boldsymbol{\sigma} \cdot \mathbf{D} - \rho\,(\dot{W} + \dot{T}\chi) \geq 0, \tag{1.6}$$

where ω is the nonnegative entropy production density, $\mathbf{D}$ is the strain-rate tensor, and $\dot{\mathbf{h}}$ is the entropy velocity field (see e.g. Besseling and Van der Giessen, 1993). Using equations (1.4), (1.5) and the relation $\mathbf{D} = \mathbf{D}^{e} + \mathbf{D}^{p}$, the local inequality (1.6) can be further arranged as

$$\begin{aligned} T\rho\omega = {} & -\operatorname{grad}T \cdot \dot{\mathbf{h}} + \boldsymbol{\sigma} \cdot \mathbf{D}^{e} - \rho\frac{\partial W^{e}}{\partial \mathbf{E}^{e}} \cdot \dot{\mathbf{E}}^{e} + \boldsymbol{\sigma} \cdot \mathbf{D}^{p} \\ & - \mathbf{B} \cdot \mathbf{D}^{p} - \rho\dot{T}\left(\chi + \frac{\partial W}{\partial T}\right) \geq 0\,. \end{aligned} \tag{1.7}$$

The inequality in (1.7) has to hold at any instant for any velocity field and so for any local continuum strain-rate $\mathbf{D}$, for any entropy velocity field $\dot{\mathbf{h}}$ and for any thermodynamic state. Noting the relation $\dot{\mathbf{E}}^{e} = \mathbf{F}^{eT}\mathbf{D}^{e}\mathbf{F}^{e}$, we obtain

$$\begin{aligned} \boldsymbol{\sigma} = \rho\mathbf{F}^{e}\frac{\partial W^{e}}{\partial \mathbf{E}^{e}}\mathbf{F}^{eT}, \qquad \chi = -\frac{\partial W}{\partial T}; \\ T\rho\omega = -\operatorname{grad}T \cdot \dot{\mathbf{h}} + (\boldsymbol{\sigma} - \mathbf{B}) \cdot \mathbf{D}^{p} \geq 0. \end{aligned} \tag{1.8}$$

It is clear that the total rate of local energy dissipation $T\rho\omega$ is composed of two independent contributions. Firstly, $-\operatorname{grad}T \cdot \dot{\mathbf{h}}$ is the rate of energy dissipation accompanying the entropy flux $\dot{\mathbf{h}}$ at a temperature gradient $\operatorname{grad}T$. Secondly, $(\boldsymbol{\sigma} - \mathbf{B}) \cdot \mathbf{D}^{p}$ is the dissipation rate resulting from the plastic strain-rate $\mathbf{D}^{p}$ in the 'dashpot' at a driving force $\boldsymbol{\sigma} - \mathbf{B}$ and $(\boldsymbol{\sigma} - \mathbf{B}) \cdot \mathbf{D}^{p}$ may be termed the dissipation rate due to irreversible deformation process.

As we mentioned before, intermolecular forces in high density polymer are substantially unaffected by isochoric deformation and the back stress $\mathbf{B}$ arises mainly from the tendency of the chain molecules to randomize the conformations available to them so as to maximize the configurational entropy χ^{p}. Therefore, we have

$$W^{p} = W^{p}(\mathbf{C}^{p}, T) \approx -T\chi^{p}. \tag{1.9}$$

Chapter 2

On Improved Network Models for Rubber Elasticity and their Applications to Orientation Hardening in Glassy Polymers

Abstract—Three-dimensional molecular network theories are studied which use a non-Gaussian statistical mechanics model for the large strain extension of molecules. Invoking an affine deformation assumption, the evolution of the network—consisting of a large number of molecular chains per unit volume, which are initially randomly oriented in space—is shown to be governed by a balance equation in orientation space. Eulerian and Lagrangian type formulations of these balance equations are given, and the closed-form analytical solution for the so-called Chain Orientation Distribution Function is derived. This full network model is then used to describe the large strain elastic hehaviour of rubbers. Detailed comparisons with experimental results and with two approximate models, namely the classical three-chain model and a very recently proposed eight-chain model, are provided for different types of deformation and rubber. Finally, the network model is applied to describe the orientational hardening in amorphous glassy polymers, and confronted with experimental data for polycarbonate. The inherent physical limitations of the network theory for both applications are discussed.

2.1. INTRODUCTION

The constitutive description of rubber elasticity by application of macromolecular network models dates back to as early as the 1940's. Treloar (1975) gives an excellent comprehensive treatment of the subject. These theories are based on the concept of a network of chains of randomly oriented rigid links that are connected at junction points which in rubberlike materials are provided by the chemical cross-links between macromolecules. The stiffness of such a network is associated with the changing configurational entropy of the network chains. The first statistical mechanics considerations of long chains assumed Gaussian statistics for the possible chain configurations, and it was found that the response of the entire network consisting of n randomly oriented chains per unit volume is identical to that of three independent sets of $n/3$ single chains in three orthogonal directions (see e.g. James and Guth, 1943). Non-Gaussian statistics were employed subsequently to single chain configurations (Kuhn and Grun, 1942) which takes into account the finite extensibility of molecular chains. However, the implementation of such a more accurate statistical theory for a single chain into a theory for the entire network of chains is far more complex than in the Gaussian theory. For uniaxial extension, James and Guth (1943) suggested to develop an approximate network model based on the simplifying assumption that the property of the Gaussian network of being equivalent to three independent sets of chains may be taken over in the non-Gaussian theory (see also Wang and Guth, 1952). Thus, the actual spatial distribution of chains is sampled in three orthogonal orientations. Similarly, Treloar (1946) proposed to use the idea of a four-chain Gaussian network representation (Flory and Rehner, 1943) to sample four spatial chain orientations. Somewhat later, Treloar (1954) formulated a full network theory for simple uniaxial extension which accounts for the actual spatial distribution of chain orientations, but this remained virtually dormant for about 25 years until Treloar and Riding (1979a) extended the theory to biaxial tensile deformations along fixed axes and actually carried out the averaging procedure. Such a full network theory can only be handled numerically, however, and therefore the simplest three-chain model has become the most widespread and almost standard non-Gaussian network model.

Network theories have also found application in the constitutive description of non-rubberlike materials, such as amorphous polymers below their glass transition temperature. When subjected to large strains, and after plastic flow has been initiated, such materials exhibit very strong strain hardening, which is primarily the result of straightening out of polymer chains between physical entanglements and the associated orientation of molecular chains. Haward and Thackray (1968) suggested for a one-dimensional model that this orientation hardening could be modelled by application of a non-Gaussian chain theory. Recently, Boyce *et al.* (1988) extended this to a general three-dimensional model (which we shall term the BPA model) by adopting the three-chain network model. This model turned out to be able to predict some of the well-known phenomena during large strains of polymers rather well, but it was found very recently by Arruda and Boyce (1991) to be unable of capturing the dependence of strain hardening on the state of deformation found experimentally in their large strain experiments on polycarbonate (PC). At the same time, they proposed to model the network by eight equivalent chains instead of three.

A detailed study of that eight-chain model for rubber elasticity in comparison with experiments on various kinds of rubber has appeared very recently (Aruda and Boyce, 1993a), and much better agreement with experiments was obtained than with the traditional three-chain model. A study of the orientation hardening in glassy polymers by the same authors has revealed similar trends (Arruda and Boyce, 1993b). Obviously, the three-chain as well as the eight-chain model are but approximate representations of the actual spatial distribution of molecular chains. Among all possible orientations these models can be regarded to sample a set of particular directions. However the accuracy of these approximations has not been established.

The purpose of this chapter is to assess the accuracy of the three- and eight-chain model by comparison with a model which accounts accurately for the actual spatial orientation distribution of molecular chains. Treloar and Riding (1979a) have already developed a rubber elasticity theory based on such a full network description; but, their considerations were limited to deformations with biaxial extension along fixed axes under plane stress conditions. In the present chapter we extend their work to a general formulation valid for 3-D deformation processes. In the first part, we focus attention to rubber networks deforming affinely with the continuum deformation [a few preliminary results have been reported by Wu and Van der Giessen

(1992a)], and in the second part we discuss the application of the network theory to describe the anisotropic strain hardening in amorphous polymers. The modelling centers around a general treatment of the orientation distribution of molecular chains and their evolution as deformation progresses. This description utilizes the idea of Chain Orientation Distribution Function (CODF), which is governed by balance equations that express physically well-understood conservation features. The authors are not aware of any comparable such treatment for networks. Assuming the network to deform affinely with the deformation of the continuum it is embedded in, closed-form solutions are derived for this CODF, which thus contain the complete information of the orientation distribution of molecular chains at any stage of the deformation. This solution is then used to develop the rubber elasticity model by averaging out the contribution to the free energy of individual chains over all chain orientations. In a modified form, similar to the work of Boyce *et al.* (1988), this full network model is used to model orientation hardening in glassy polymers. The full network model requires numerical integration; an approximation based on the three- and eight-chain representations turns out to be very accurate over the entire range of strains. Verification with some experimental results from the literature is provided both for the elastic behaviour of a few rubber materials and for the plastic response of a typical glassy polymer like polycarbonate.

2.2. IMPROVED NETWORK MODELS FOR RUBBER ELASTICITY

The development of molecular orientation in rubber-like materials under deformation, has been extensively studied, often by measuring the optic anisotropy or birefringence. Various deformation schemes have been proposed, based on the standard conception of a vulcanized rubber as an assembly of molecules linked together at well-defined junction points (points of vulcanization or cross-linking). One of the simple schemes is the so-called affine model, which is based on two key assumptions: *i*) statistical fluctuations of the position of the junction points about their mean position can be neglected, *ii*) the end-to-end vector of a chain (between junction points) co-deforms with the local deformation of the continuum it is embedded in. According to this scheme, as deformation progresses each chain stretches while rotating towards a preferred direction. At all stages each chain attempts to maximize its entropy by disorienting the elements or random links, subject only to the constraints imposed by the end-to-end vectors.

It is to be noted here that in the traditional application to purely elastic rubber-like materials, the affine deformation assumption literally implies that the end-to-end vectors deform as material lines on the continuum. In this paper we shall also be concerned with the application to molecular networks in glassy polymers in which case the network distortion will not follow the continuum deformation exactly. Nevertheless, there will be a connection between the two, but in order to keep the discussion concise, we may, for the time being, distinguish between the deformations of the network and the continuum, respectively, thus allowing for these deformations to be instantaneously different. The precise link between the two depends on the application of the network model; this will be further discussed for rubbers in Sec. 2.2.3 and for glassy polymers in Sec. 2.3.2.

2.2.1. Single Chain Behaviour

We start out by briefly recapitulating the well-known non-Gaussian considerations for a single molecular chain (see, e.g., Treloar, 1975). Consider a single chain between two junction points, with its end-to-end vector $\mathbf{r}_0$ in the initial state being specified by angular coordinates θ_0 and φ_0, $0 \le \theta_0 \le \pi$, $0 \le \varphi_0 \le 2\pi$, with respect to some initial frame of reference defined by the set of orthonormal base vector $\mathbf{e}_i^0$ (see Fig. 2.1). If the chain contains N links of length l, the length r_0 of the unstrained free chain is given by the root-mean-square value $\sqrt{N}l$. Furthermore, consider some strained state of the chain in which the end-to-end vector $\mathbf{r}$ has length r and is oriented at angles θ and φ with respect to some current orthonormal set $\{\mathbf{e}_i\}$. In our considerations in the present and the next subsection, the two frames of references can be chosen arbitrarily; in Sec. 2.2.3 and subsequent discussions, we shall deal with the kinetics of the deformation of chains and we shall make specific identifications for $\mathbf{e}_i^0$ and $\mathbf{e}_i$, respectively. For now, it suffices to note that the stretch of the end-to-end vector in the strained state is $\lambda = r/r_0$.

By considering the statistical distribution of possible link angles at a given vector length r, Kuhn and Grun (1942) were the first to derive the configurational entropy χ of the stretched chain. Their non-Gaussian chain statistics approach accounts for the finite extensibility of the chain and hence is valid for large stretches up to the limiting stretch $\lambda_L = \sqrt{N}$, even for short chains with a small value of N. Furthermore, they showed that the Helmholtz free energy w for a single chain at stretch λ (at constant absolute temperature T) is determined by the configurational entropy χ through $w = -T\chi$, and hence is given by

$$w = kNT\left(\frac{\lambda}{\sqrt{N}}\beta + \ln\frac{\beta}{\sinh\beta}\right) - w_0\,, \qquad \beta = \mathcal{L}^{-1}\left(\frac{\lambda}{\sqrt{N}}\right), \tag{2.1}$$

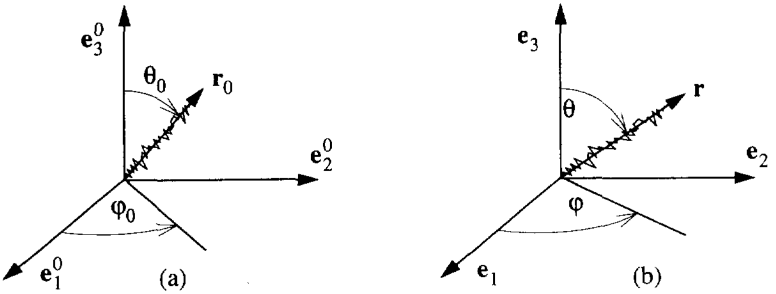

Fig. 2.1. A single chain in unstrained (a) and strained (b) state; definition of geometric quantities.

where w_0 is an arbitrary constant, k is Boltzmann's constant and $\mathcal{L}$ is the Langevin function defined by

$$\mathcal{L}(\beta) = \coth\beta - 1/\beta.$$

The work-rate of stress per unit volume is $\sigma\dot{\varepsilon}$ with $\dot{\varepsilon} = \dot{\lambda}/\lambda$, so that for purely elastic, isothermal deformation processes we find $\sigma\dot{\varepsilon} = \dot{w} = (\partial w/\partial\lambda)\,\dot{\lambda}$. Hence

$$\sigma = \lambda\frac{\partial w}{\partial\lambda}$$

with

$$\frac{\partial w}{\partial \lambda} = kT\sqrt{N}\mathcal{L}^{-1}\left(\frac{\lambda}{\sqrt{N}}\right). \tag{2.2}$$

2.2.2. *The Chain Orientation Distribution Function*

Now consider a network of molecular chains with a random distribution of the orientation of their end-to-end vector $\mathbf{r}_0$ in the unstrained state. Each individual chain is described as discussed above. The deformation of the network is assumed to be homogeneous in the sense that all chains are assumed to be subjected to the same network deformation tensor. The adjective "network" is used here, as mentioned before, to emphasize that in this subsection we shall be concerned only with the network and not with the continuum it is embedded in.

We will assume that the number of the chains per unit volume, n, is large. In effect, for characterizing the distribution of the chain orientations and stretches, we will make the transition to a continuum-like network model by considering the limiting case of an infinite number of chains. Hence, we can identify a continuous distribution of chain orientations. A so-called molecular Chain Orientation Distribution Function (CODF), denoted by $C(\theta, \varphi; t)$, is now introduced such that the relative density of molecular chains whose **r**-vector orientation at some instant t, falls in the range between (θ, φ) and $(\theta + \mathrm{d}\theta, \varphi + \mathrm{d}\varphi)$ is given by $C(\theta, \varphi; t)\sin\theta\mathrm{d}\theta\mathrm{d}\varphi$. Note that $\sin\theta\mathrm{d}\theta\mathrm{d}\varphi$ is the area on a unit sphere spanned by the interval $(\mathrm{d}\theta, \mathrm{d}\varphi)$ and that t is a time-like parameter. The actual number of chains between (θ, φ) and $(\theta + \mathrm{d}\theta, \varphi + \mathrm{d}\varphi)$ then is

$$\mathrm{d}n = C(\theta, \varphi; t)\sin\theta\mathrm{d}\theta\mathrm{d}\varphi. \tag{2.3}$$

For a virgin, unstrained material the orientation of network chains can usually be considered to be distributed in a random fashion initially; then C will be independent of θ and φ, and the material's response is instantaneously isotropic. When the material is deformed all chains are stretched and, at the same time, rotated as will be shown in detail later. Hence, the CODF will develop into a nonuniform distribution, which may be quite severe, as will also be demonstrated later. Thus, texture development in the sense of molecular chain distributions is described in this model in terms of this CODF.

By definition,

$$\int_0^{\pi}\int_0^{2\pi} C(\theta, \varphi; t)\sin\theta\mathrm{d}\theta\mathrm{d}\varphi = 1, \tag{2.4}$$

so that a uniform distribution, corresponding to isotropic properties, is characterized by $C(\theta, \varphi; t) = C_0 = 1/4\pi$. During the deformation process of the network, the CODF is subject to continuous change and this evolution is governed by a continuity equation in orientation space which we will now derive.

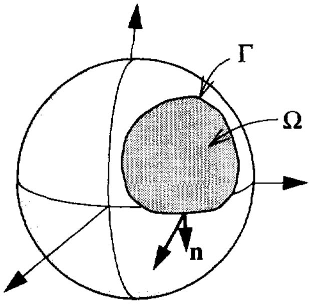

Fig. 2.2. A surface region Ω with boundary Γ on a unit sphere in orientation space. The increase of the volume fraction of chains per unit time within Ω must be balanced with the outflow over the boundary Γ [see (2.5)].

Consider an arbitrary surface region Ω of a unit sphere bounded by the curve Γ, fixed in space (see Fig. 2.2.). The conservation law is expressed in the form that the rate at which the chains contained in Ω increases is equal to the rate at which chains enter into Ω over its boundary Γ:

$$\iint_{\Omega} \frac{\partial (C\sin\theta)}{\partial t}\,\mathrm{d}\theta\,\mathrm{d}\varphi + \oint_{\Gamma} (C\sin\theta)\,\mathbf{v}\cdot\mathbf{n}\,\mathrm{d}\Gamma = 0, \tag{2.5}$$

where $\partial\,(C\sin\theta)\,/\partial t$ is the rate of increase of $C\sin\theta$ at a fixed point in Ω, $\mathbf{v}$ denotes the vector $(\dot{\theta}, \dot{\varphi})$ in (θ, φ) -space, $\mathbf{n}$ denotes the outward unit normal to Γ and a $\cdot$ denotes the inner product of vectors. Rewriting the contour integral and applying Green's theorem gives

$$\oint_{\Gamma} (C\sin\theta)\,\mathbf{v}\cdot\mathbf{n}\,\mathrm{d}\Gamma = \iint_{\Omega} \left(\frac{\partial (C\sin\theta\dot{\theta})}{\partial\theta} + \frac{\partial (C\sin\theta\dot{\varphi})}{\partial\varphi} \right) \mathrm{d}\theta\,\mathrm{d}\varphi. \tag{2.6}$$

Combining (2.5) and (2.6), we obtain the continuity equation for the CODF by a standard argument:

$$\frac{\partial (C\sin\theta)}{\partial t} + \frac{\partial (C\sin\theta\dot{\theta})}{\partial\theta} + \frac{\partial (C\sin\theta\dot{\varphi})}{\partial\varphi} = 0. \tag{2.7}$$

Equation (2.7) describes the change in the CODF at a given point in orientation space at which a number of chains is moving in orientation space. Using standard terminology of continuum mechanics, the derivation above can be referred to as an Eulerian formulation. Alternatively, we can give a Lagrangian treatment in which we follow the motion of one and the same set of chains through orientation space.

By applying the standard transformation procedure in multidimensional integration, the left-hand side of (2.4) can be written in terms of the initial orientation (θ_0, φ_0) as

$$\int_0^{\pi}\int_0^{2\pi} C\sin\theta\,\mathrm{d}\theta\,\mathrm{d}\varphi = \int_0^{\pi}\int_0^{2\pi} C(\theta, \varphi; t)\sin\theta J\,\mathrm{d}\theta_0\,\mathrm{d}\varphi_0,$$

where in the right-hand side,

$$\theta = \theta(\theta_0,\varphi_0;t), \qquad \varphi = \varphi(\theta_0,\varphi_0;t),$$

$$J = \left|\frac{\partial(\theta,\varphi)}{\partial(\theta_0,\varphi_0)}\right| = \frac{\partial\theta}{\partial\theta_0}\frac{\partial\varphi}{\partial\varphi_0} - \frac{\partial\theta}{\partial\varphi_0}\frac{\partial\varphi}{\partial\theta_0} \tag{2.8}$$

On the other hand, we may also assume a given initial orientation distribution C_0, so that from the balance law (2.4) we have,

$$\int_0^{\pi}\int_0^{2\pi} C\sin\theta\,d\theta\,d\varphi = \int_0^{\pi}\int_0^{2\pi} C_0\sin\theta_0\,d\theta_0\,d\varphi_0.$$

Therefore, we obtain the relationship

$$C(\theta,\varphi;t) = C_0\frac{\sin\theta_0}{\sin\theta}J^{-1}. \tag{2.9}$$

The Eulerian and Lagrangian interpretations of the motion of chains in orientation space can be made more explicit by defining a convective time derivative D/Dt in addition to the local derivative $\partial/\partial t$ appearing in (2.5) and (2.7). By analogy to the convective or material time derivative in continuum mechanics, we define

$$\frac{D}{Dt} = \frac{\partial}{\partial t} + \dot{\theta}\frac{\partial}{\partial\theta} + \dot{\varphi}\frac{\partial}{\partial\varphi}, \tag{2.10}$$

so that for any arbitrary quantity f,

$$\frac{Df}{Dt}(\theta,\varphi;t) = \frac{\partial}{\partial t}f(\theta(\theta_0,\varphi_0;t),\varphi(\theta_0,\varphi_0;t);t) \tag{2.11}$$

The convective derivative Df/Dt can be interpreted simply as the rate of change of the quantity f as measured by an observer travelling with the chains in orientation space. With this definition, the local continuity condition (2.7) for the CODF can be rewritten as

$$\frac{D(C\sin\theta)}{Dt} + C\sin\theta\left(\frac{\partial\dot{\theta}}{\partial\theta} + \frac{\partial\dot{\varphi}}{\partial\varphi}\right) = 0, \tag{2.12}$$

while the integral condition (2.5) becomes

$$\frac{D}{Dt}\iint_{\Omega} C\sin\theta\,d\theta\,d\varphi = 0.$$

Recalling the definition of C, the total value F of some quantity f associated with individual chains in some orientation is given by

$$F = \iint_{\Omega} fC\sin\theta\,d\theta\,d\varphi.$$

For future reference, we note that the rate of change of F can be conveniently expressed as

$$\frac{DF}{Dt} = \iint_{\Omega}\frac{Df}{Dt}C\sin\theta\,d\theta\,d\varphi \tag{2.13}$$

in terms of the convective derivative. The proof is fully similar to that of Reynolds' transport theorem in continuum mechanics and will not be elaborated on further.

2.2.3. Full Network Model—Eulerian Form

In this section, we shall further elaborate on the network in rubber-like materials, where the network deformation can be regarded to coincide at each moment with the continuum deformation in which it is embedded. Thus, when the material is subject to some three-dimensional deformation process represented by the deformation gradient tensor **F**, each chain's end-to-end vector $\mathbf{r}_0$ is taken to be distorted (i.e. strained) and rotated to the vector **r** in an affine manner, i.e. $\mathbf{r} = \mathbf{F}\mathbf{r}_0$. The associated principal stretches λ_i $(i = 1, ..., 3)$ as well as the corresponding Lagrangian principal directions $\mathbf{e}_i^0$ in the undeformed configuration and the Eulerian principal directions $\mathbf{e}_i$ in the current deformed configuration are defined through

$$\mathbf{C}\mathbf{e}_i^0 = \lambda_i^2\mathbf{e}_i^0 \qquad (\text{no sum}), \qquad \mathbf{C} = \mathbf{F}^{\mathrm{T}}\mathbf{F} \tag{2.14}$$

and

$$\mathbf{B}\mathbf{e}_i = \lambda_i^2\mathbf{e}_i \qquad (\text{no sum}), \qquad \mathbf{B} = \mathbf{F}\mathbf{F}^{\mathrm{T}}, \tag{2.15}$$

respectively. Here, **C** and **B** are the usual right and left Cauchy-Green tensors, respectively. In the sequel it will be extremely convenient to identify the frames of reference for the chain orientations (θ_0,φ_0) and (θ,φ) in the initial and strained state, by these Langrangian and Eulerian triads $\mathbf{e}_i^0$ and $\mathbf{e}_i$, respectively.

It is assumed that no volume change takes place during deformation of the network and hence of the continuum. Furthermore, intermolecular interactions and changes in internal energy are neglected during the deformation. Accordingly, the total free energy *W* for the network is given simply by the sum of the free energies *w* of the individual chains, i.e.

$$W = \int w \mathrm{d}n,$$

with *w* according to (2.2) and d*n* being the actual number of chains whose r-vector orientation falls in the range of (θ,φ) and $(\theta + \mathrm{d}\theta, \varphi + \mathrm{d}\varphi)$. According to (2.3), *W* can be expressed in the terms of the CODF as given by

$$W = n\int_0^{\pi}\int_0^{2\pi} wC(\theta,\varphi;t)\sin\theta\,\mathrm{d}\theta\,\mathrm{d}\varphi. \tag{2.16}$$

Here, we have substituted the principal stretches as the time-like parameter *t* in the previous expressions for the CODF. This is possible since, as a consequence of the affine deformation assumption, the distortion of the network is independent of the rate of deformation, so that *t* only needs to be some monotonic parameter. Identifying *t* with λ_i will turn out to be convenient for further development.

Expression (2.16) shows that due to the affine deformation assumption and the isotropy of the initial orientation distribution of the chain vectors $\mathbf{r}_0$, the total free energy *W* for the network can be expressed solely as a function of the principal stretches λ_i. By a standard argument (see, e.g. Ogden, 1984), it then follows that the principal axes of the Cauchy stress tensor $\boldsymbol{\sigma}$, coincide with the Eulerian triad $\{\mathbf{e}_i\}$, so that

$$\boldsymbol{\sigma} = \sum_i \sigma_i (\mathbf{e}_i \otimes \mathbf{e}_i) \qquad (2.17)$$

with the principal stresses σ_i required to sustain the imposed deformation being determined by the gradient of W in λ_i-space. Recalling the exposition in the previous subsection, the convective derivative $\mathrm{D}/\mathrm{D}t$ is the appropriate rate of change of any chain-associated quantity. After identifying t with λ_i again, the appropriate gradient in this paper is $\mathrm{D}/\mathrm{D}\lambda_i$ so that we obtain

$$\sigma_i = \lambda_i \frac{\mathrm{D}W}{\mathrm{D}\lambda_i} - p \qquad (\text{no sum}). \qquad (2.18)$$

Here, p is an additional hydrostatic pressure which is left indeterminate by the free energy function because of incompressibility, $\lambda_1\lambda_2\lambda_3 = 1$, but which is determined from the boundary conditions. With the total free energy W being given by (2.16), we obtain according to (2.13)

$$\frac{\mathrm{D}W}{\mathrm{D}\lambda_i} = n\iint_{\Omega} \frac{\mathrm{D}w}{\mathrm{D}\lambda_i} C \sin\theta \,\mathrm{d}\theta \,\mathrm{d}\varphi. \qquad (2.19)$$

We now proceed by deriving the expressions for w and the CODF C as a function of the principal stretches that need to be substituted into (2.19). To that end, we consider the distortion of an initial chain end-to-end vector $\mathbf{r}_0$ into the end-to-end vector $\mathbf{r}$ in the current state. The components of the associated unit direction vectors $\mathbf{m} = \mathbf{r}/r = m_i\mathbf{e}_i$ in current state, and $\mathbf{m}_0 = \mathbf{r}_0/r_0 = m_i^0\mathbf{e}_i^0$ in the initial state are (see Fig. 2.1)

$$m_1 = \sin\theta\cos\varphi, \qquad m_2 = \sin\theta\sin\varphi, \qquad m_3 = \cos\theta, \qquad (2.20)$$

and

$$m_1^0 = \sin\theta_0\cos\varphi_0, \qquad m_2^0 = \sin\theta_0\sin\varphi_0, \qquad m_3^0 = \cos\theta_0, \qquad (2.21)$$

respectively. Invoking the affine deformation assumption, $\mathbf{r} = \mathbf{F}\mathbf{r}_0$, and the well-known continuum mechanics relationship $\mathbf{F}\mathbf{e}_i^0 = \lambda_i\mathbf{e}_i$ (no sum), the components of the unit direction vectors $\mathbf{m}$ and $\mathbf{m}_0$ on the Langrangian and Eurlerian bases respectively, are interrelated by

$$m_i = \frac{\lambda_i}{\lambda} m_i^0 \qquad (2.22)$$

or

$$\sin\theta\cos\varphi = \frac{\lambda_i}{\lambda}\sin\theta_0\cos\varphi_0, \quad \sin\theta\sin\varphi = \frac{\lambda_i}{\lambda}\sin\theta_0\sin\varphi_0, \quad \cos\theta = \frac{\lambda_i}{\lambda}\cos\theta_0. \qquad (2.23)$$

Furthermore, one may invoke $\mathbf{r} = \mathbf{F}\mathbf{r}_0$ so as to eliminate $\mathbf{r}$ from the expression $\lambda^2 = r^2/r_0^2 = (\mathbf{r}\cdot\mathbf{r})/(\mathbf{r}_0\cdot\mathbf{r}_0)$, such that the stretch λ can be written as $\lambda^2 = \mathbf{m}_0\cdot\mathbf{C}\cdot\mathbf{m}_0$. Introducing then the components of $\mathbf{m}_0$ on the Langrangian triad $\mathbf{e}_i^0$ gives, with the aid of (2.14),

$$\lambda^2 = \sum_i (m_i^0)^2 \lambda_i^2. \tag{2.24}$$

This expression determines the stretch λ of a single chain as a function of its initial orientation, i.e. λ is found as a function $\lambda(\theta_0, \varphi_0; \lambda_i)$. Similarly, by starting out from $\lambda^{-2} = r_0^2/r^2 = (\mathbf{r}_0 \cdot \mathbf{r}_0)/(\mathbf{r} \cdot \mathbf{r})$, one finds

$$\lambda^{-2} = \sum_i m_i^2/\lambda_i^2, \tag{2.25}$$

which governs the stretch as a function of the current chain orientation, i.e. $\lambda(\theta, \varphi; \lambda_i)$.

With either one of these relations for λ as a function of λ_i, the free energy function w to be substituted into (2.19) can be formally constructed. However, one may note that

$$\frac{\mathrm{D}w}{\mathrm{D}\lambda_i} = \frac{\partial w}{\partial \lambda}\frac{\mathrm{D}\lambda}{\mathrm{D}\lambda_i},$$

where $\partial w/\partial\lambda$ is immediately given by (2.2) and where, according to the definition of the derivative $\mathrm{D}/\mathrm{D}\lambda_i$, the term $\mathrm{D}\lambda/\mathrm{D}\lambda_i$ is the partial derivative of λ as a function $\lambda(\theta_0, \varphi_0; \lambda_i)$. This function is determined by (2.25), and after differentiation and elimination of m_i^0 by means of (2.22), one finds $\mathrm{D}\lambda/\mathrm{D}\lambda_i = (\lambda/\lambda_i)\, m_i^2$. Hence,

$$\frac{\mathrm{D}W}{\mathrm{D}\lambda_i} = nkT\sqrt{N}\int_0^{\pi}\int_0^{2\pi} C\mathcal{L}^{-1}\left(\frac{\lambda}{\sqrt{N}}\right)\lambda\frac{m_i^2}{\lambda_i}\sin\theta\,\mathrm{d}\theta\,\mathrm{d}\varphi,$$

and the principal stresses, according to (2.18), can be written as

$$\sigma_i = C^{\mathrm{R}}\sqrt{N}\int_0^{\pi}\int_0^{2\pi} C\mathcal{L}^{-1}\left(\frac{\lambda}{\sqrt{N}}\right)\lambda m_i^2 \sin\theta\,\mathrm{d}\theta\,\mathrm{d}\varphi - p, \tag{2.26}$$

where $C^{\mathrm{R}} = nkT$ is known as the rubber modulus.

The final step now is the derivation of the solution for the CODF $C = C(\theta, \varphi; \lambda_i)$. With the help of (2.20), (2.23), (2.25) and (2.8), the CODF can now be explicitly determined from (2.9) by a very long but straightforward calculation, which results in the following general expression:

$$C(\theta, \varphi; \lambda_i) = C_0 \lambda^3(\theta, \varphi; \lambda_i), \tag{2.27}$$

where $C_0 = 1/4\pi$ is the initial uniform distribution and where $\lambda(\theta, \varphi; \lambda_i)$ is to be solved from (2.25). Substituting (2.27) into (2.26), we finally obtain the principal stresses as

$$\sigma_i = \frac{1}{4\pi}C^{\mathrm{R}}\sqrt{N}\int_0^{\pi}\int_0^{2\pi} C\mathcal{L}^{-1}\left(\frac{\lambda}{\sqrt{N}}\right)\lambda^4 m_i^2 \sin\theta\,\mathrm{d}\theta\,\mathrm{d}\varphi - p \tag{2.28}$$

Once these principal stresses are evaluated, the stress tensor $\boldsymbol{\sigma}$ itself is constructed by application of (2.17).

2.2.4. Full Network Model—Lagrangian Form

The full network model we derived in the above can also be developed in the initial configuration, i.e. in a Lagrangian form. There are two different ways to arrive at this. One is an approach based on the initial, uniform chain orientation distribution as demonstrated by Wu and Van der Giessen (1992a). The other, which we will now derive, employs a transformation of (2.28).

The principal stresses in the form (2.26) can be directly transformed to the initial configuration:

$$\sigma_i = C^{\mathrm{R}} \sqrt{N} \int_0^{\pi} \int_0^{2\pi} C \mathcal{L}^{-1} \left(\frac{\lambda}{\sqrt{N}}\right) \lambda \frac{\lambda_i^2 \left(m_i^0\right)^2}{\lambda^2} \sin\theta J \, d\theta_0 \, d\varphi_0 - p$$

with J according to (2.8). By noting (2.9) or $C \sin\theta J = C_0 \sin\theta_0 = (1/4\pi) \sin\theta_0$, we finally obtain

$$\sigma_i = \frac{1}{4\pi} C^{\mathrm{R}} \sqrt{N} \int_0^{\pi} \int_0^{2\pi} \mathcal{L}^{-1} \left(\frac{\lambda}{\sqrt{N}}\right) \frac{\lambda_i^2 \left(m_i^0\right)^2}{\lambda} \sin\theta \, d\theta_0 \, d\varphi_0 - p \qquad (2.29)$$

with $\lambda = \lambda(\theta_0, \varphi_0; \lambda_i)$ calculated from (2.24).

Equations (2.29) are exactly as derived previously by the authors (Wu and Van der Giessen, 1992a). As pointed out in that paper, the equations (2.29) are similar to that given by Treloar and Riding (1979a). However, Treloar and Riding limited their attention to *i*) biaxial deformation, and *ii*) to deformations with fixed principal axes of stretching so that the Eulerian and Lagrangian triads retained fixed orientations in space. The present formulation is valid for arbitrary three-dimensional deformations; for the biaxial deformations mentioned, the model reduces to that in Treloar and Riding (1979a).

It will be noted that in this Lagrangian approach, the CODF is not needed at all for the computation of the network stresses. This is an obvious advantage when one is only interested in the stress-strain response. But, the CODF in itself is an essential source of information about the actual orientation distribution of molecular chains at any stage of a general three-dimensional state of deformation, which the authors have not found before in the literature.

2.2.5. Simplified models

In the present paper, we shall consider two simplified network models that have been proposed in the literature, namely the three-chain model and eight-chain model. The three-chain model was originally suggested by James and Guth (1943) and assumes that a network containing n chains per unit volume is equivalent to three independent (non-interacting) sets of $n/3$ chains per unit volume parallel to the Eulerian principal axes as shown in Fig. 2.3a. The principal values of the stress tensor according to this model are

$$\sigma_i^{3\text{-ch}} = \frac{1}{3} C^{\mathrm{R}} \sqrt{N} \lambda_i \mathcal{L}^{-1}\left(\frac{\lambda_i}{\sqrt{N}}\right) - p \tag{2.30}$$

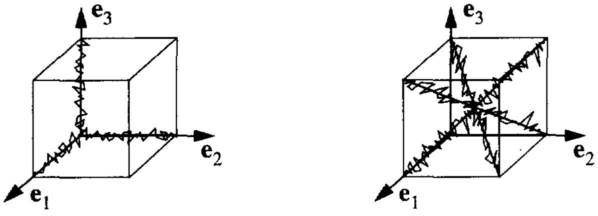

(a) (b)

Fig. 2.3. Schematic representation of the three-chain model (a) and the eight-chain model (b).

The eight-chain model was proposed by Arruda and Boyce (1991, 1993a) and considers a set of eight chains connecting the central junction point and each of eight corners of the unit cube as shown in Fig. 2.3b. The principal values of the stress tensor according to this model are given by

$$\sigma_i^{8\text{-ch}} = \frac{1}{3} C^{\mathrm{R}} \sqrt{N} \frac{\lambda_i^2}{\lambda} \mathcal{L}^{-1} \left(\frac{\lambda}{\sqrt{N}}\right) - p \tag{2.31}$$

with

$$\lambda^2 = \frac{1}{3} \sum_i \lambda_i^2 .$$

Comparing these three- and eight-chain samplings with the actual 3-D initial random distribution of molecular chains, we expected that the three-chain model would be likely to overestimate the actual stiffness of the network, while the eight-chain representation would probably give a lower bound (Wu and Van der Giessen, 1992a). Indeed, as will be demonstrated in the next section, the stress response predicted by our full network model (2.28) or (2.29) is for the same value of N and C^{R} always in between that predicted by the three-chain model and eight-chain model, respectively. However, the integrations involved in (2.28) and (2.29) require a rather time-consuming numerical procedure (see Sec. 2.2.6), which is certainly not appealing when one wishes to incorporate the model in for instance finite element computations. All these observations motivated us to search for an approximation of the full integration by combining the three-chain and eight-chain models. One possibility is a simple linear combination,

$$\sigma_i = (1 - \rho)\, \sigma_i^{3\text{-ch}} + \rho \sigma_i^{8\text{-ch}} , \tag{2.32}$$

where the parameter ρ may be a constant or related to some other physical quantity which is for instance related to the deformation process. In our previous paper (Wu and Van der Giessen, 1992a), ρ was proposed to be related to the maximal principal stretch $\lambda_{\max} = \max(\lambda_1, \lambda_2, \lambda_3)$ by

$$\rho = 0.85 \lambda_{\max} / \sqrt{N} \tag{2.33}$$

where the factor 0.85 was chosen to give the best correlation with full integration of (2.28) or (2.29). In this way, the eight-chain contribution in (2.32) becomes increasingly important when $\lambda_{\max}$ approaches the limit stretch $\lambda_L = \sqrt{N}$ of a single chain.

2.2.6. *Results*

Before considering the stress responses according to the network models described in the above, we shall first study the distortion of the network during a few deformation processes in terms of the CODF. As mentioned before, the CODF gives the precise spatial distribution of the chain orientations for an arbitrary three-dimensional deformation, and thus provides key information about the anisotropy of chain associated quantities. Also, this will provide important hindsight to appreciate the simplified network models later on.

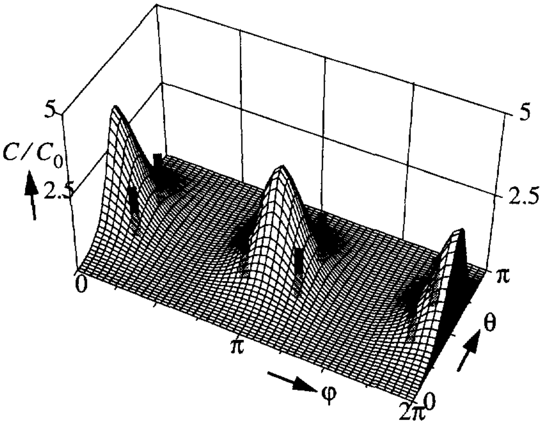

Fig. 2.4. Three-dimensional plot of the CODF during uniaxial tension along the $\mathbf{e}_1$ direction for a stretch of $\lambda = 1.5$. The vertical bars indicate the orientation of the chain in the eight chain model.

Equation (2.27) is the general expression for the CODF in the current orientation space (θ, φ) relative to the Eulerian triad at given values of the principal stretches λ_i, with the function $\lambda(\theta, \varphi; \lambda_i)$ to be solved from (2.25). Figures 2.4 and 2.5 show the CODF during uniaxial extension at various stages of the applied stretch λ. In that case, the Eulerian triad retains fixed directions in space and the principal stretches are $\lambda_1 = \lambda$, $\lambda_2 = \lambda_3 = \lambda^{-1/2}$. The three-dimensional plot in Fig. 2.4 gives a complete picture of the spatial chain orientation at a stretch of $\lambda = 1.5$. The molecular texture created during this deformation due to the stretching out and simultaneous rotation of the chains is clearly seen as two distinct peaks in the CODF in the stretching direction $\mathbf{e}_1$, i.e. $\varphi = 0$, $\theta = 0$ or $\theta = \pi$. As stretching continues, these peaks become increasingly intense, as shown in Fig. 2.5 in a two-dimensional section of the CODF in the $\mathbf{e}_1$-$\mathbf{e}_2$ plane $(\theta = \pi/2)$ for various stretches. It will appear to be instructive to compare the actual spatial chain distribution with the three- chain and eight-chain approximations. In the three-chain model of Fig. 2.3a, the network is represented by three effective chains along the three principal directions, where the one along the tensile stretch direction $\mathbf{e}_1$ will have to carry the tensile stress. Thus, this single chain should represent the actual cloud of chains around this preferred direction as shown in Figs. 2.4 and 2.5, a large fraction of which do not quite have that preferred direction and will contribute less to the axial stiffness. Shown explicitly in Fig. 2.4 is the orientation of the eight chains in the eight-chain model of Fig. 2.3b at the current stretch level, which is readily obtained from the expressions (2.23), (2.24). It is seen that these orientations have rotated towards the actual CODF peaks with ongoing deformation, but are considerably off the ideal orientation. This implies that any chains that are oriented close to the ideal orientation, and which therefore will carry most of the load, are not taken into account in the eight-chain model.

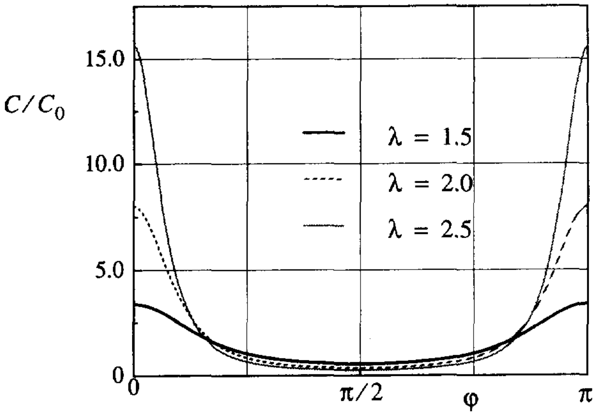

Fig. 2.5. Plane section of the CODF at $\theta = \pi/2$ during uniaxial tension (cf. Fig. 2.4) at various levels of the stretch λ.

Next, we consider the case of simple (and not *pure*) shear, where the deformation gradient is given by the components

$$[F_{ij}] = \begin{bmatrix} 1 & \gamma & 0 \\ 0 & 1 & 0 \\ 0 & 0 & 1 \end{bmatrix}$$

with respect to some global Cartesian basis $\{\mathbf{g}_i\}$. In this case, the Eulerian strain triad $\{\mathbf{e}_i\}$ does not retain a fixed orientation in space, but the $\mathbf{e}_1$-$\mathbf{e}_2$ axes are inclined with respect to the $\mathbf{g}_1$-$\mathbf{g}_2$ axes at an angle $\alpha = (\pi/4) + (1/2)\arctan(\gamma/2)$. The actual spatial orientation in the $\mathbf{g}_1$-$\mathbf{g}_2$ plane is therefore given by the angle $\Phi = \alpha + \varphi$, and this angle is used to plot the section of the CODF in that plane $(\theta = \pi/2)$ as shown in Fig. 2.6. It is observed that molecular orientation effects now lead to the development of strong CODF peaks at the principal stretch orientations (i.e. for $\varphi = 0$) which, in addition, rotate towards the final orientation $\Phi = \alpha = 0$ for the shear $\gamma \to \infty$.

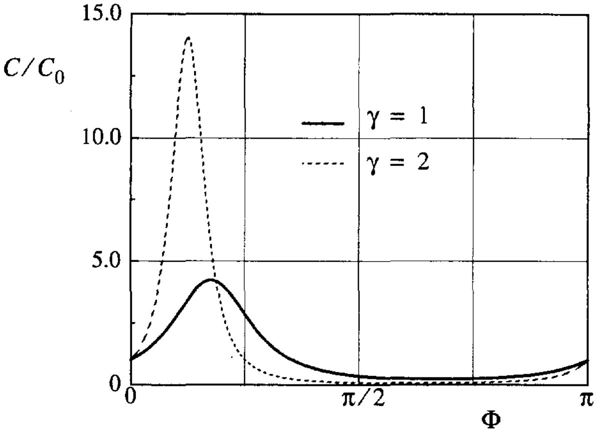

Fig. 2.6. Plane section of the CODF at $\theta = \pi/2$ during plane simple shear at two stages of the deformation.

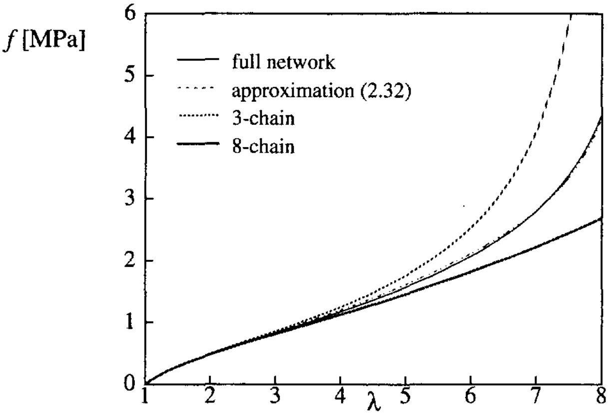

Fig. 2.7. Predicted load vs. stretch diagram for uniaxial tension according to different network models with $N = 75$ and $C^R = 0.273$ MPa.

We shall now proceed by considering the stress-strain response according to the models discussed above. The principal stresses according to the full network model are given by either the Eulerian expression (2.28) or the Lagrangian form (2.29). At each stage of the deformation, the double integrals in these expressions are evaluated by first noting that due to symmetry only the intervals $\theta \in [0, \pi/2]$, $\varphi \in [0, \pi/2]$ need to be considered, then subdividing that area into a number of cells and integrating within each cell using Gaussian quadrature. This procedure is basically equivalent to that described by Treloar and Riding (1979a). Recursive refinement is applied for each cell until the integral is obtained within a relative error of 10^{-5}. The Eulerian and Lagrangian expressions (2.28) and (2.29), respectively, are mathematically equivalent, but it turns out that the evaluation of the integrals in the Eulerian expression is much more time-consuming than the Lagrangian one because the integrand is a significantly more nonlinear function of θ and φ.

Figure 2.7 shows the predicted response to uniaxial extension in the $\mathbf{e}_1$ direction with principal stretches $\lambda_1 = \lambda$, $\lambda_2 = \lambda_3 = \lambda^{-1/2}$, as discussed above. The principal tensile stress is $\sigma_1 = \sigma$, while the conditions $\sigma_2 = \sigma_3 = 0$ are used to determine the unknown pressure p in the constitutive relations (2.28)-(2.31). Contrary to Wu and Van der Giessen (1992a) who presented the results in terms of the true stress σ, we here show the nominal stress f or load per unit undeformed area, which is in this case simply given by $f = \sigma\lambda_2\lambda_3 = \sigma/\lambda$. Figure 2.7 shows the results according to the full network model as well as the simplified three-chain and eight-chain models. The values $N = 75$ and $C^R = 0.273$ MPa were used for all three models; they were simply used as representative values of N and C^R, and were given by Treloar (1975) for uniaxial tension of a vulcanized rubber. All models considered correctly predict a typical S-shaped load vs stretch curve exhibited by rubber materials. What this result clearly shows is that relative to the full network model, the three-chain approximation tends to overestimate the stiffness at large stretches, while the eight-chain model tends to underestimate. There is no significant difference up to stretches of $\lambda \approx 3$ (or roughly 30% of the limit stretch). The difference at larger stretches seems to be associated with the different limit stretches of the complete network. The stretching according to the three-chain model is limited directly by the limit tensile stretch $\lambda_L = \sqrt{N}$ of the chains parallel to the tensile direction, while the overall network limiting stretches for the eight-chain model exceeds λ_L. It is seen that the approximate expression (2.32) for the full network response is indeed very accurate up to very large stretches.

A more important aspect appears to be the description of the network response under different states of deformation. Indeed, the primary motivation for the introduction of the eight-chain model by Arruda and Boyce (1991) was the observation that the standard three-chain model could not pick up the dependence of the state of deformation observed experimentally in rubber materials. In order to assess the accuracy with which the three- and eight-chain models can account for the state of deformation dependence, Arruda and Boyce (1993a) took the following procedure. For a given model, the network parameters N and C^R for a certain material are fitted from uniaxial tension or compression data, and are then used to predict other deformation processes like equi-biaxial tension or plane strain compression. Here, we shall follow a similar procedure but now for the simplified models in comparison with the full network model. Our procedure will be slightly different in the sense that we shall not fit C^R and N independently, but we shall use one value of C^R for all three models. The motivation for this is that the small strain behaviour is governed primarily by C^R, while the network models virtually coincide at these strains (and in fact approach the Gaussian network model). The various network predictions differ essentially only at relatively large strains, and the values of N will be fitted in that range. We shall apply this for two materials and two classes of deformations, as shown in Figs. 2.8 and 2.9, respectively.

Figure 2.8 shows results for uniaxial and biaxial tension of a natural-rubber gum as reported by James *et al.* (1975). The (equi-) biaxial stretching is characterized by the principal stretches $\lambda_1 = \lambda_2 = \lambda$, $\lambda_3 = \lambda^{-2}$ along fixed directions, while the material is in a state of plane stress, i.e. $\sigma_3 = 0$. The figures show the loads in the stretching directions, i.e. $f = \sigma_1/\lambda$ for uniaxial tension and $f = \sigma_1/\lambda = \sigma_2/\lambda$ for biaxial tension. The Figs. 2.8a to c show results for the three-chain, eight-chain and full network models, respectively, where in each case the value $C^R = 0.4$ was used while the value of N was fitted for each model to the uniaxial data. It is observed that the three-chain model (see Fig. 2.8a) cannot predict the significantly different behaviour in biaxial tension, especially at larger stretches. The eight-chain model does predict a stiffer response in biaxial tension at larger stretches, but still underestimates the experimental data (see Fig. 2.8b). Notice that the value of N for the eight-chain model is about three times smaller than that for the three-chain model. These conclusions are similar to those found by Arruda and Boyce (1993a) using similar data from Treloar (1944) for another material. Figure 2.8c shows the results for the full network model, and it is seen that the predicted response for biaxial tension is significantly lower than the experimental data and in fact is slightly lower than that according to the eight-chain model.

The second set of cases, shown in Fig. 2.9, is concerned with uniaxial and plane strain compression of a silicone rubber as investigated also by Arruda and Boyce (1993a). Uniaxial compression in the $\mathbf{e}_1$ direction is characterized by principal stretches $\lambda_1 = \lambda < 1$, $\lambda_2 = \lambda_3 = \lambda^{-1/2}$, while plane strain compression is determined by $\lambda_1 = \lambda < 1$, $\lambda_2 = 1$, $\lambda_3 = \lambda^{-1}$. For all three models the value $C^R = 0.435$ is used, and the value of N is for each model fitted to the uniaxial data. It is seen in Fig. 2.9a that the three-chain model overestimates the stiffness during plane strain compression for compressions $1/\lambda$ larger than about 2, while the eight-chain model is found to slightly underestimate the stress response in that regime (see Fig. 2.9b). The plane strain compression prediction for the full network shown in Fig. 2.9c agrees well with the experimental results up to $1/\lambda \approx 2.5$ but for continued compression a softer response was found experimentally.

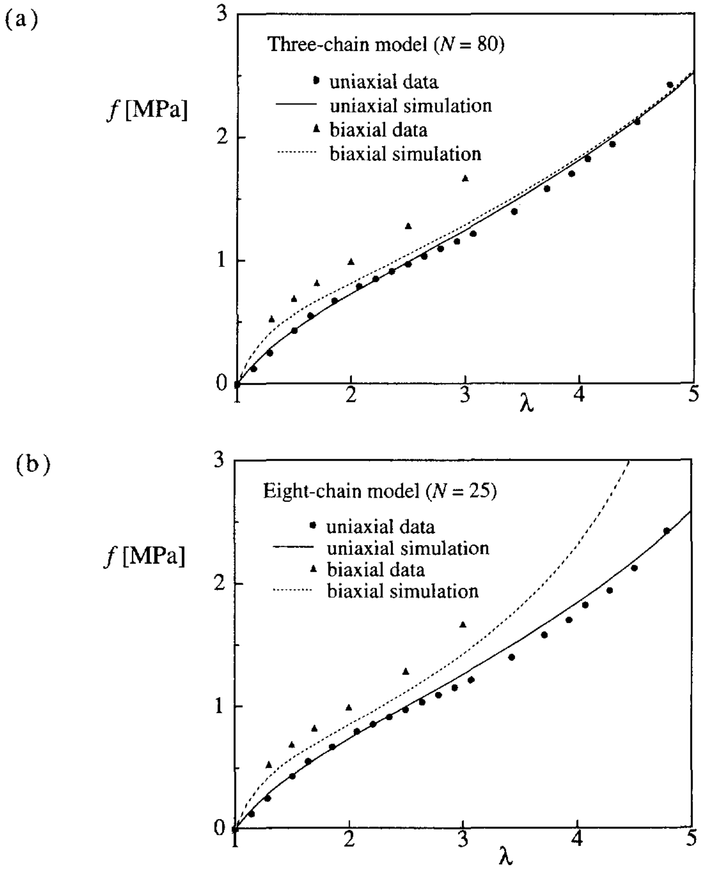

(c)

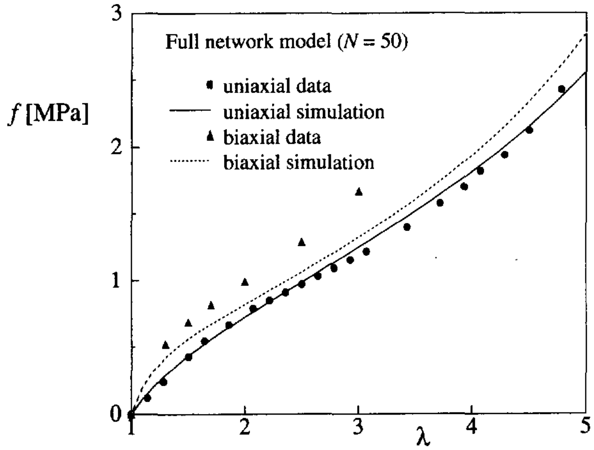

Fig. 2.8. Load vs. stretch diagram for uniaxial and equi-biaxial tension of a natural-rubber gum for the three-chain (a), the eight-chain (b) and the full network model (c). The experimental data is taken from James *et al.* (1975) and $C^R = 0.4$ MPa.

At this point, it should be recalled that the three- and eight-chain models are both based on approximate descriptions of an affine network model, and that our full network theory is based on the exact treatment of that concept. As suggested also by Arruda and Boyce (1993a) one would expect that the full network model provides a better description of real rubber behaviour. However, we do not find that the full network model's predictions are necessarily in better agreement with experimental results than the predictions of the eight-chain model. Especially the biaxial tension results of Fig. 2.8 are captured best by the eight-chain model. This does not imply however that the eight-chain model is a better model *per se*. There are several assumptions that underly the present network concept, and which can act as potential sources of discrepancy with experiments. First of all, there are several so-called network defects, such as unstable crosslinks and interlooping of chains or entanglements, as suggested already by Flory (1944), which may have a very significant effect. One of the key assumptions is that the junction points in the network provide permanent nodes in the network; however, molecular chains may also slide relative to each other at so-called sliplinks (see, e.g., Ball *et al.*, 1981). All these network defects will tend to lower that the actual stiffness of the network. Furthermore, the affine assumption is known to hold with high accuracy at low deformations, but it has been suggested that as the deformation increases, the behaviour of a real network approaches the so-called phantom network in which the junction points move independent of the continuum (see e.g. Mark and Erman, 1988). Also it cannot be ruled out that at large deformations, when chains are rotated towards a common axis to such an extent that they become ligned up, intermolecular interactions are no longer negligible. Molecular dynamics simulations (Gao and Weiner, 1991) seem to indicate that this may be a significant effect already at relatively small deformations in the Gaussian regime, and it may be expected to be even more important at the large strain levels considered here, leading to a more diffuse CODF than predicted here. In conclusion, if the eight chain model seems to effectively pick up all these effects in an average sense, this is more due to sheer coincidence than to more accurate modelling.

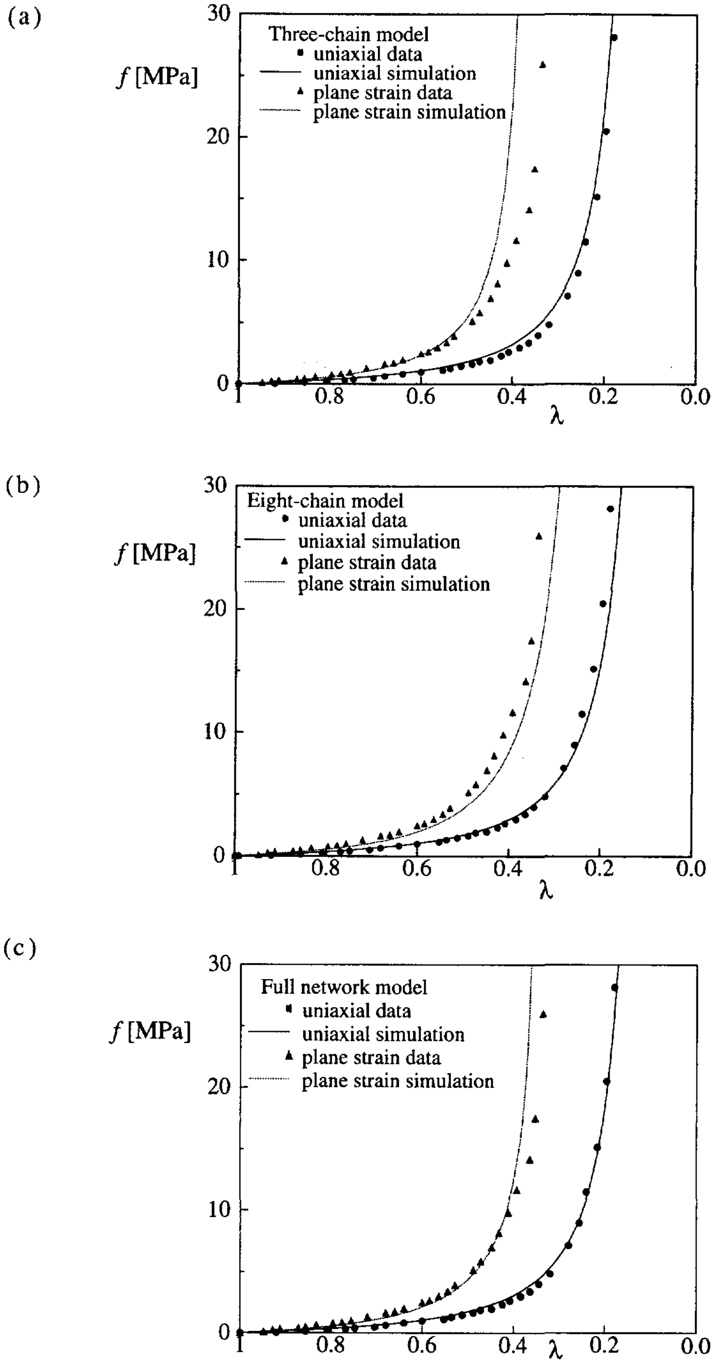

Fig. 2.9. Load vs. stretch diagram for uniaxial and plane strain compression of a silicone rubber gum for the three-chain (a), the eight-chain (b) and the full network model (c). The experimental data is taken from Arruda and Boyce (1993a) and $C^R = 0.435$ MPa.

2.3. A LARGE INELASTIC DEFORMATION MODEL FOR GLASSY POLYMERS

We start by briefly recapitulating the so-called BPA model developed by Boyce, Parks and Argon (1988). In the BPA model, the microstructure of an isotropic amorphous polymer is assumed to consist primarily of long molecular chains, which are randomly coiled in space. Side groups protrude from the backbone chains at various locations and, in conjunction with overall chain trajectory, can act as nodes, or points of physical entanglement. This results in a network-like structure much like that of rubber as discussed in Sec. 2.2, but with the chemical cross-links replaced by physical entanglements.

Following the work of Haward and Thackray (1968), it is further assumed that a glassy polymer must overcome two physically distinct sources of resistance before large strain inelastic flow may occur. Below the glass transition temperature, prior to initial yield, the material must be stressed to exceed its intermolecular resistance to segment rotation; this will be discussed first. Once the material is free to flow, molecular alignment occurs, resulting in an anisotropic internal resistance to further inelastic deformation, which is called orientational hardening; this shall be discussed in Sec. 2.3.2.

The intermolecular resistance to plastic flow is due to the impedance imposed by neighbouring chains on the ability of a chain segment to rotate either individually or in a cluster. Argon (1973) developed an expression for the plastic shear strain rate, $\dot{\gamma}^{\mathrm{p}}$, which ensues once the isotropic barrier to chain segment rotation has been overcome:

$$\dot{\gamma}^{\mathrm{p}} = \dot{\gamma}_0 \exp\left[-\frac{As_0}{T}\left(1-\left(\frac{\tau}{s_0}\right)^{5/6}\right)\right] \tag{2.34}$$

where $\dot{\gamma}_0$ is a pre-exponential factor, A is proportional to the activation volume/Boltzmann's constant, T is the absolute temperature and τ is the applied shear stress. Furthermore, $s_0 = 0.077\mu/(1-\nu)$ is the athermal shear strength, μ is the elastic shear modulus, υ is Poisson's ratio. Boyce *et al.* (1988) extended this expression to include the effects of pressure and strain softening. They used $s+\alpha p$ instead of s_0, where p is the pressure and α is a pressure dependence coefficient. Furthermore, s is assumed to evolve with plastic straining via $\dot{s} = h(1-s/s_{\mathrm{ss}})\,\dot{\gamma}^{\mathrm{p}}$, where h is the rate of resistance drop with respect to the plastic strain and s_{ss} is the assumed saturation value of s.

2.3.1. Three-dimensional representation

Consider the homogeneous deformation of an initially isotropic body loaded so that its deformation gradient at a subsequent time is $\mathbf{F}$. The deformation gradient may be multiplicatively decomposed into elastic and plastic parts, $\mathbf{F} = \mathbf{F}^{\mathrm{e}}\mathbf{F}^{\mathrm{p}}$. Following Lee (1969) and others, Boyce *et al.* (1988) take $\mathbf{F}^{\mathrm{e}}$ to be symmetric, so that $\mathbf{F}^{\mathrm{p}}$ represents the relaxed configuration obtained by unloading without rotation (in the polar decomposition sense). Hence, $\mathbf{F}^{\mathrm{p}}$ can be decomposed as $\mathbf{F}^{\mathrm{p}} = \mathbf{V}^{\mathrm{p}}\mathbf{R}$ with the plastic stretch $\mathbf{V}^{\mathrm{p}}$ and the total stretch $\mathbf{V}$ in polar decomposition $\mathbf{F} = \mathbf{V}\mathbf{R}$ being related by $\mathbf{V} = \mathbf{F}^{\mathrm{e}}\mathbf{V}^{\mathrm{p}}$. The rate quantities corresponding to this decomposition consist of the velocity gradient $\mathbf{L}$,

$$\mathbf{L} = \dot{\mathbf{F}}\mathbf{F}^{-1} = \mathbf{D} + \mathbf{W} = \dot{\mathbf{F}}^{e}\mathbf{F}^{e-1} + \mathbf{F}^{e}\mathbf{L}^{p}\mathbf{F}^{e-1}$$

where $\mathbf{D}$ is the rate of deformation, $\mathbf{W}$ is the spin, and $\mathbf{L}^{p} = \mathbf{D}^{p} + \mathbf{W}^{p} = \dot{\mathbf{F}}^{p}\mathbf{F}^{p-1}$ is the velocity gradient in the relaxed configuration. With the adopted symmetry of $\mathbf{F}^{e}$, the skewsymmetric part $\mathbf{W}^{p}$ is algebraically given as $\mathbf{W}$ plus a term dependent on $\mathbf{F}^{e}$ and $\mathbf{D} + \mathbf{D}^{p}$ (see Boyce *et al.*, 1988). The rate of change of shape of the relaxed configuration, $\mathbf{D}^{p}$, must be constitutively prescribed. In the BPA model, the magnitude of $\mathbf{D}^{p}$ is taken to be given by the plastic shear strain rate, $\dot{\gamma}^{p}$, according to (2.34) while the tensor direction of $\mathbf{D}^{p}$ is specified by $\mathbf{N}$, so that

$$\mathbf{D}^{p} = \dot{\gamma}^{p}\mathbf{N}, \tag{2.35}$$

where the direction $\mathbf{N}$ is the deviatoric part of the driving stress, normalized by the effective equivalent shear stress τ:

$$\mathbf{N} = \frac{1}{\sqrt{2}\tau}\tilde{\boldsymbol{\sigma}}', \qquad \tau = \sqrt{\frac{1}{2}\tilde{\boldsymbol{\sigma}}' \cdot \tilde{\boldsymbol{\sigma}}'} \tag{2.36}$$

The driving stress $\tilde{\boldsymbol{\sigma}}$ itself is defined by

$$\tilde{\boldsymbol{\sigma}} = \boldsymbol{\sigma} - \frac{1}{J}\mathbf{F}^{e}\mathbf{B}\mathbf{F}^{e} \tag{2.37}$$

where $\boldsymbol{\sigma}$ is the Cauchy stress tensor and $\mathbf{B}$ is the back stress tensor due to the strain hardening resulting from molecular alignment. The corresponding effective stress τ is taken to be the driving force in the plastic flow equation (2.34). The Cauchy stress is taken to be given by the elastic constitutive law (Anand, 1979)

$$\boldsymbol{\sigma} = \frac{1}{J}(\underset{\sim}{\mathcal{L}}_{e}\ln\mathbf{F}^{e}) \tag{2.38}$$

where $\underset{\sim}{\mathcal{L}}_{e}$ is the fourth-order isotropic elastic modulus tensor. The theory needs to be complemented with constitutive equations for the back stress $\mathbf{B}$. In all computations to be presented later, the elastic strains remain small and all geometric nonlinearities associated with elastic deformations such as in (2.37) are neglected (see also Boyce *et al.*, 1988).

2.3.2. Orientation hardening

Once the material is stressed to the point of overcoming intermolecular barriers to chain motion, the molecular chains will be stretched and will tend to align along the direction of principal plastic stretch. This action decreases the configurational entropy of the system which, in turn, is responsible for the internal resistance to continued flow. This process of network distortion is very similar to that of rubber network, and Haward and Thackray (1968) suggested to describe this for uniaxial extension by means of a back stress determined through the Langevin expression (2.2). Boyce *et al.* (1988) extended this approach to general three dimensional plastic deformations by introducing a back stress tensor $\mathbf{B}$ which is taken to be coaxial with the plastic stretch tensor $\mathbf{V}^{p}$. Thus, if $\mathbf{e}_{i}^{p}$ are the unit eigen vectors of $\mathbf{V}^{p}$, corresponding to a plastic stretch λ_i^{p}, the back stress $\mathbf{B}$ is constructed as

$$\mathbf{B} = \sum_i B_i (\mathbf{e}_i^{\mathrm{p}} \otimes \mathbf{e}_i^{\mathrm{p}})$$

from the principal components B_i. Boyce *et al.* (1989) presented an extended version of their model to accounted for initial anisotropy; but, here we will assume that the initial network structure of the polymer is isotropic.

According to the three-chain implementation of Boyce *et al.* (1988), the principal components of $\mathbf{B}$ can be determined from equations (2.30), where the λ_i are now replaced by λ_i^{p}, the principal values of the left plastic stretch tensor $\mathbf{V}^{\mathrm{p}}$. Since plastic flow according to (2.35), (2.36) is affected only by the deviatoric part of $\tilde{\boldsymbol{\sigma}}$, we stipulate $\mathbf{B}$ to be deviatoric, so that the principal components of the back stress tensor according to this three-chain non-Gaussian network model are

$$B_i^{3\text{-ch}} = \frac{1}{3} C^{\mathrm{R}} \sqrt{N} \left[\lambda_i^{\mathrm{p}} \mathcal{L}^{-1}\left(\frac{\lambda_i^{\mathrm{p}}}{\sqrt{N}} \right) - \frac{1}{3} \sum_{j=1}^{3} \lambda_j^{\mathrm{p}} \mathcal{L}^{-1}\left(\frac{\lambda_j^{\mathrm{p}}}{\sqrt{N}} \right) \right] \tag{2.39}$$

However, very recently, Arruda and Boyce (1991) found that the three-chain non-Gaussian network model was not capable of picking up the strain hardening observed experimentally in polycarbonate (PC). These findings seem to have triggered their suggestion to model the network by eight equivalent chains instead of three, and very recently presented a detailed discussion and comparison with experimental results for PC and polymethylmethacrylate (PMMA) (Arruda and Boyce, 1993b). The principal, deviatoric components of the back stress tensor according to this eight-chain non-Gaussian network model are (cf. eq. (2.31))

$$B_i^{8\text{-ch}} = \frac{1}{3} C^{\mathrm{R}} \sqrt{N} \mathcal{L}^{-1}\left(\frac{\lambda^{\mathrm{p}}}{\sqrt{N}} \right) \frac{\lambda_i^{\mathrm{p}^2} - \lambda^{\mathrm{p}^2}}{\lambda^{\mathrm{p}}}, \qquad \lambda^{\mathrm{p}^2} = \frac{1}{3} \sum_{j=1}^{3} \lambda_j^{\mathrm{p}^2}. \tag{2.40}$$

On the basis of our considerations in the previous section for rubber-like materials, we can now also consider the full network model, in which full account is given of the orientation distribution of the individual chains in the network. According to this model, the principal back stresses are given by (cf. eq. (2.29))

$$B_i = \frac{1}{4\pi} C^{\mathrm{R}} \sqrt{N} \int_0^{\pi} \int_0^{2\pi} \mathcal{L}^{-1}\left(\frac{\lambda^{\mathrm{p}}}{\sqrt{N}} \right) \frac{\lambda_i^{\mathrm{p}^2} m_i^{0^2} - \lambda^{\mathrm{p}^2}/3}{\lambda^{\mathrm{p}}} \sin\theta_0 d\theta_0 d\varphi_0,$$

$$\lambda^{\mathrm{p}^2} = \sum_j (m_j^0)^2 \lambda_j^{\mathrm{p}2}, \tag{2.41}$$

with m_i^0 defined by (2.21) and with λ^{p} being defined similar to (2.24). Here, the averaging is carried out in the initial configuration. Alternatively, B_i can be identified in the Eulerian form (cf. eq. (2.28))

$$B_i = \frac{1}{4\pi} C^{\mathrm{R}} \sqrt{N} \int_0^{\pi} \int_0^{2\pi} \mathcal{L}^{-1}\left(\frac{\lambda^{\mathrm{p}}}{\sqrt{N}}\right) (\lambda^{\mathrm{p}})^4 \; (m_i^2 - \tfrac{1}{3}) \sin\theta d\theta d\varphi , \qquad \lambda^{\mathrm{p}^{-2}} = \sum_j m_j^2 / \lambda_j^{\mathrm{p}^2} , \quad (2.42)$$

with m_i defined by (2.20) and with λ^{p} according to a similar expression as (2.25). Similar to (2.32) for rubber-like materials, an approximation of the full network predictions can be sought in the form of a combination of the three-chain and eight-chain models through

$$B_i = (1 - \rho_{\mathrm{p}}) B_i^{\text{3-ch}} + \rho_{\mathrm{p}} B_i^{\text{8-ch}} , \qquad (2.43)$$

thus avoiding the time-consuming integration involved in (2.41) and (2.42). Here, ρ_{p} is considered to be related to the maximal principal plastic stretch $\lambda^{\mathrm{p}}_{\max} = \max(\lambda^{\mathrm{p}}_1, \lambda^{\mathrm{p}}_2, \lambda^{\mathrm{p}}_3)$ via $\rho_{\mathrm{p}} = 0.85\lambda^{\mathrm{p}}_{\max}/\sqrt{N}$. Assuming that the actual physically entangled molecular chains behave sufficiently close to a perfect non-Gaussian network, this full network model should give a more accurate description than the approximate three- and eight-chain models. In this spirit, the full network model will now be used to assess the adequacy of the simplified hardening expressions (2.39), (2.40).

(a)

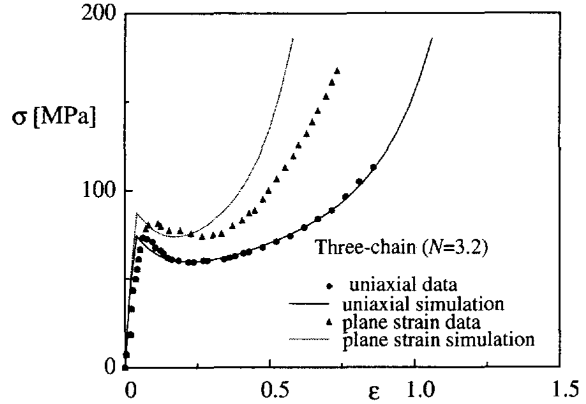

(b)

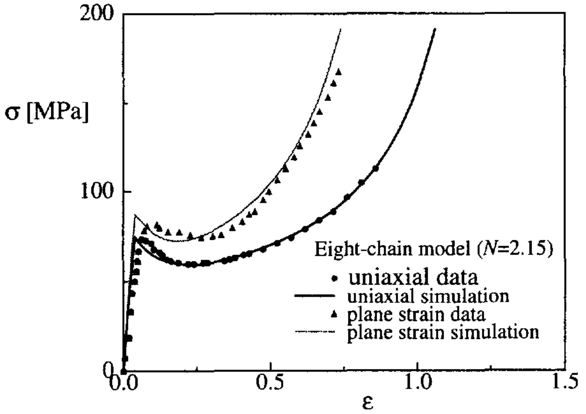

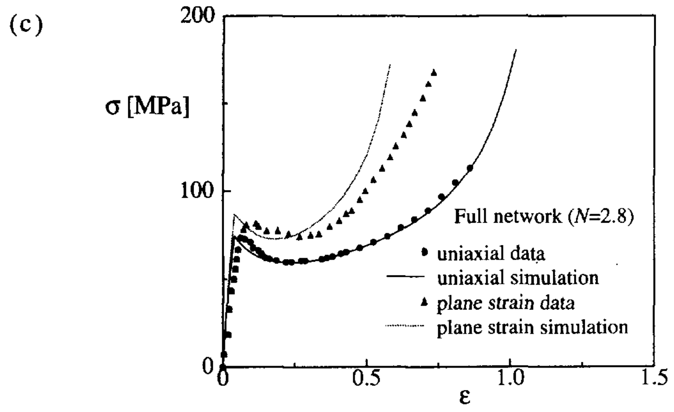

Fig. 2.10. Simulated true stress vs. true strain curve for compression of PC at room temperature according to the three-chain (a), the eight-chain (b) and the full network model (c) for the orientation hardening. The experimental results are from Arruda and Boyce (1993b) and the material parameters used in the numerical simulation are $E = 2300$ MPa, $\nu = 0.3$, $\dot{\gamma}_0 = 2\times 10^{-15}\ \mathrm{s}^{-1}$, $A = 240$ K/MPa, $s_0 = 97$ MPa, $s_{ss}/s_0 = 0.79$, $h = 500$ MPa, $\alpha = 0.08$ and $C^R = 12.8$ MPa.

2.3.3. Results

Arruda and Boyce (1993b) give a detailed discussion of the predictions of the above mentioned constitutive models using either the three-chain or the eight-chain network model in comparison with experimental results on PC and PMMA. In particular, they study the accuracy with which the orientational hardening in these materials can be predicted with these simplified models under different states of deformation, viz. uniaxial compression and plane strain compression. Here we wish to reconsider one of their series of tests in order to assess the deviation of these approximate network models based on expressions (2.39), (2.40) from the more exact full network description contained in (2.41),. These tests relate to uniaxial or plane strain compression of PC at room temperature $(T = 23^{\circ}\mathrm{C})$, which are specified by the following velocity gradient components with respect to a global Cartesian basis:

$$\text{uniaxial compression } [L_{ij}] = \begin{bmatrix} -\dot{\varepsilon} & 0 & 0 \\ 0 & \underset{\sim}{\dot{\varepsilon}} & 0 \\ 0 & 0 & \underset{\sim}{\dot{\varepsilon}} \end{bmatrix}, \text{plane strain compression } [L_{ij}] = \begin{bmatrix} -\dot{\varepsilon} & 0 & 0 \\ 0 & \underset{\sim}{\dot{\varepsilon}} & 0 \\ 0 & 0 & 0 \end{bmatrix}.$$

The applied strain-rate was taken as $\dot{\varepsilon} = 0.01/\mathrm{s}$, and the transverse strain-rate $\underset{\sim}{\dot{\varepsilon}}$ is determined from the boundary conditions $\sigma_{22} = \sigma_{33} = 0$ and $\sigma_{22} = 0$ for uniaxial and plane strain compression, respectively. The stress response in terms of the compressive stress $\sigma = -\sigma_{11}$ versus the logarithmic strain ε is obtained by numerically integrating the BPA constitutive equations (2.34)-(2.38) in an incremental manner. The back stresses are at each increment computed from the current plastic stretch; in the case of the full network model, we used the expressions (2.41) and applied the same numerical integration scheme as in Sec. 2.2.6.

The values of the elastic and viscoplastic material parameters to be used in the simulation are based on tensile experiments on PC (Boyce and Arruda, 1990). Following Arruda and Boyce (1993b), the parameters C and N that deter- mine the orientational hardening are fitted for all three network models to the uniaxial compression data. However, as opposed to Arruda and Boyce (1993b), we have chosen to use the same value of C^R for all three models, for the reason that C^R governs the network hardening at small plastic strains, while at that stage there is no conceivable difference yet between the various network models (see also Sec. 2.2.6). With the parameters thus obtained, the plane strain compression response is simulated and compared with the experimental results shown in Fig. 2.10. It is seen that the uniaxial responses is picked up very accurately with each of the models with the chosen value of N; but these values cannot be determined very accurately because the maximum plastic stretches attained before failure are still far off the limit stretch. The various predicted plane strain responses exhibit the same tendency as found in the foregoing for rubber elasticity in Fig. 2.9: the plane strain responses according to the three- and eight-chain models provide upper bound and lower bounds, respectively, to the full network predictions. The best agreement with experiments is obviously obtained in this case with the eight-chain model.

As a further assessment of the adequacy of these network models, we will now consider the deformation of PC (at room temperature) by simple shear. This is a significantly different deformation process than the tension or compression tests, and has not been studied in this context before. The problem analyzed is that of homogeneous simple shear in the x_1-x_2 plane, as determined by the velocity gradient components $L_{12} = \dot{\gamma}$, $L_{ij} = 0$ otherwise, implying a plane strain condition in the x_3-direction. Using a special test setup, G'Sell and Gopez (1985) were able to produce this state of deformation in a relatively large part of their specimen with good accuracy. In accordance with their room temperature experiments on PC, we consider a shear rate $\dot{\gamma} = 3 \times 10^{-3} s^{-1}$. The material constants are taken to be the same as in the above compression cases.

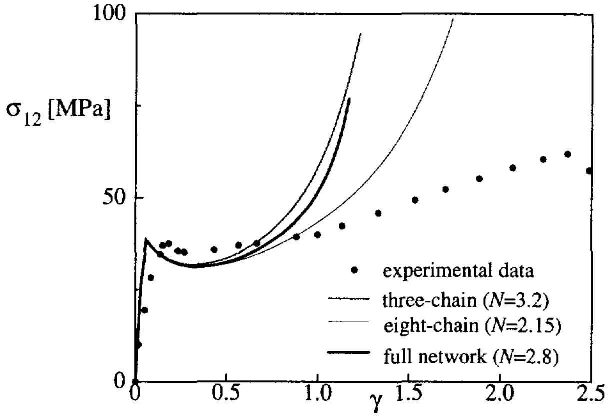

Fig. 2.11. Shear stress response to large simple shear of PC at room temperature at a shear strain-rate of $\dot{\gamma} = 3 \times 10^{-3}$ s^{-1}. The experimental data is estimated from the macroscopic load and shear strain data from G'Sell and Gopez (1985), and the material parameters used for the simulation are identical to those listed in Fig. 2.10.

Figure 2.11 shows the shear stress σ_{12} as a function of the shear strain γ. Also shown are a number of experimental points taken from G'Sell and Gopez (1985). This data is obtained from the measured overall shear force on the specimen and the macroscopic shear strain, and is expected not to give a very accurate estimate of the actual stress state associated with pure simple shear because of the observed shear band propagation and end effects (work that considers these effects in detail is currently in progress). Focusing attention here to the post-yield behaviour, it is seen that the actual orientational hardening remains much less than that predicted by the BPA model for any of the network models. In agreement with the above findings, the eight- chain model predicts the lowest hardening, but beyond a shear strain of $\gamma \approx 1$ the limit stretching feature of the network theory becomes noticeable, while the actual response shows rather little hardening anyway.

The secondary normal stresses σ_{11} and σ_{22} during simple shear are mainly due to the development and the subsequent rotation of the induced anisotropy. It is well-known that the prediction of these phenomena generally shows a rather strong dependence on the constitutive models—in particular the description of anisotropic hardening; for large strain metal plasticity, this has been studied in detail by e.g. Van der Giessen *et al.* (1992a). Figure 2.12 now shows the predicted normal stress σ_{22} as a function of the shear strain γ according to the present constitutive model. In all cases, the normal stress is rather small up to $\gamma \approx 1$. For larger shears, the 3-chain model predicts very large compressive stresses that are associated with the stretching of the net- work affinely with the plastic deformation. Initially, the principal directions of the plastic stretch are oriented at roughly 45° relative to the x_1-x_2 axes, and this orientation slowly rotates towards the final "ideal" x_1-x_2 directions with ongoing shearing. But the limit stretching of the network is attained long before such final orientations are reached, thus explaining the very substantial normal stress. The full network model predicts roughly the same normal stress development, but when using the 8-chain model, we see that the magnitude of the normal stress reduces drastically. Unfortunately, we have not been able to find any experimental data on normal stress development during simple shear of PC in order to compare these predicted results with experiments. Nevertheless, it seems unlikely that the very large values for $\gamma > 1$ are realistic.

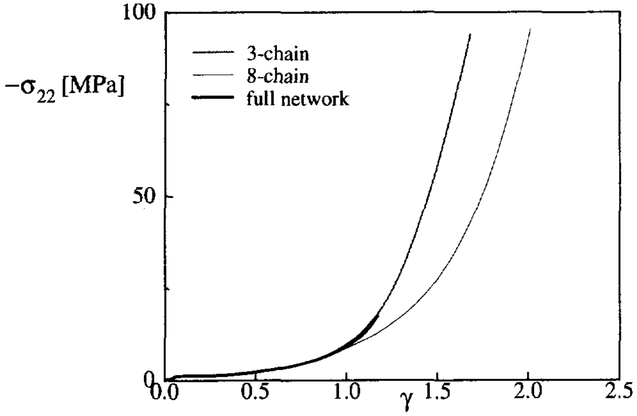

Fig. 2.12. Development of compressive stress during large simple shear of PC at room temperature. Strain-rate and material parameters are as in Fig. 2.11.

We have repeated the above mentioned analyses for PMMA using the material constants given by Boyce *et al.* (1988). The trends in shear stress and normal stress development were found to be qualitatively completely similar to the above results, and we shall therefore not discuss this further.

After this discussion of the accuracy of the various network representations, it is very pertinent to briefly point out that our predictions may be strongly dependent on a number of assumptions in the constitutive model. In particular one needs to realize that the idea of using an affine network theory to model the stretching of the molecular network assumes that the junction points in the network remain in tact. However, it has been suggested in the literature (see, e.g., Raha and Bowden, 1972; Botto *et al.*, 1987) that physical entanglements in amorphous polymers are being pulled out during deformation. In terms of our network model this would mean that the number of chains n reduces in the course of the deformation process, while the number of links N per chain increase, thus reducing the stiffness of the network. This aspect absolutely requires further study. Furthermore, there is the particular way of incorporating deformation-induced anisotropy by means of the effective stress concept in (2.36). This is probably rather important in the above simple shear considerations, where the stress history is nonproportional and significant rotations of the principal axes occur. A different approach may be found in e.g. Batterman and Bassani (1990).

2.4. CONCLUSION

We have carefully considered the so-called non-Gaussian affine network models for molecular networks, and their application to modelling rubber elasticity and the orientation hardening in glassy amorphous polymers. Our considerations have extended Treloar and Riding's (1979a) analysis for uniaxial and biaxial extension of rubber networks to general three-dimensional deformation processes. Our full network model fully accounts for the spatial distribution of the orientation of the chain end-to-end vectors. The purpose of studying this model here in some detail is to assess the accuracy of two approximate models in which the network response is modelled by sampling a few particular chain orientations, namely the classical three-chain model first suggested by James and Guth (1943), and the eight-chain model proposed very recently by Arruda and Boyce (1991, 1993a).

The general tendency of the predictions of these simplified models compared with the more exact full network theory is that with the same network parameters, the three-chain model overestimates the stiffness of the network at large strains, while the eight-chain model underestimates the stiffness. At small strains the models are indistinguishable. Another important aspect is the capability of the different models to capture the dependence of the network response to the state of deformation. It turns out that the three-chain model is not capable of picking-up this dependence, whereas the eight-chain tends to overestimate the dependence of the state of deformation as compared with the full network model.

The predictions of the network models both for rubber elasticity and for orientation hardening in glassy polymers are compared with available experimental results. In studying the dependence of the state of deformation in rubber-like materials it was found that the full network gave a much better quantitative agreement with experiments than the classical three-chain model. On the other hand, the eight-chain model performed even better sometimes, although this is an approximation of the full network model. It thus seems that this performance is not an inherent feature of the eight-chain model; rather, this reminded us of the constitutive assumptions involved in the affine network theory. It has been noted that further improvement of this physically based model for rubber elasticity requires a better understanding of the role of various kinds of network defects in rubber-like materials that are not taken into account at present. The application to glassy polymers is based upon even stronger assumptions. We have also discussed that one of the most important phenomena that has been neglected in the present modelling is the pulling out of entanglements in such polymers. The present results employing the full network model indicate that this may give rise to a significantly softer response than expected on the basis of the perfect network model. However, most of these matters are not well understood yet, and are among the outstanding problems in polymer physics.

In addition to a complete description of the stress-strain response during network deformation, the present study has contributed in a more general sense to the understanding of the evolution of molecular orientation in 3D during large deformations. General balance equations have been derived in both Eulerian and Lagrangian formulations, and together with the affine deformation assumption this has led to a description of molecular re-orientation in a continuous sense in terms of what we called the CODF. This CODF gives the volume fraction of the molecular chains in a certain orientation in space. The general solution has been derived in closed form for 3D network distortions that are affine with the continuum stretch. Apart from its key role in the development of the stress-strain relations, this solution may turn out to be useful for constitutive formulation of anisotropic behaviour connected with the orientation distribution of molecular chains.

Chapter 3

On Network Descriptions of Mechanical and Optical Properties of Rubbers

Abstract—The non-Gaussian full network model for rubber elasticity is re-formulated in a more efficient and more micromechanics motivated manner. Based on such a full network description, a so-called full network model for rubber photoelasticity is proposed, by introducing directional polarizabilities into the individual links of the idealized randomly-jointed chain. This optical theory can be used to study the optical properties or birefringence-strain behaviour of rubbers in arbitrary 3-D deformation states. Detailed comparisons with two approximate models, namely the classical three-chain model and a so-called eight-chain model for rubber photoelasticity, which is also developed in this paper, are provided for different types of deformation. The predicted numerical results are compared with experimental data found in the literature.

3.1. INTRODUCTION

The present understanding of mechanical behaviour of amorphous polymers owes much to early advances in the network theory of rubber elasticity [see e.g. Kuhn and Grun (1942) and Treloar (1975)]. These theories are based upon the concept of a network of chains of randomly oriented rigid links that are connected at junction points which in rubber-like materials are provided by the chemical cross-links between macromolecules. Furthermore, these network theories use a so-called affine deformation scheme, which is based on two key assumptions: (*i*) Statistical fluctuations of the position of the junction points about their mean position can be neglected, (*ii*) the end-to-end vector of a chain between junction points co-deforms with the local deformation of the continuum it is embedded in. According to this scheme, as deformation progresses each chain stretches while rotating towards a preferred direction. At all stages each chain attempts to maximize its entropy by disorienting the elements or random links, subject only to the constraints imposed by the end-to-end vectors. Another important assumption involved in these network models is that intermolecular interactions are negligible in comparison to intramolecular effects. The overall properties of the network are then obtainable by simply summing the contributions of the individual chains. Furthermore, the exact non-Gaussian treatments of a single chain, both for mechanical and optical behaviour, are available (developed originally by Kuhn and Grun, 1942; and James and Guth, 1943). However, exact treatment of the transition from an individual chain to network behaviour is very difficult owing to its mathematical complexity. In principle, this transition (through an averaging process) needs the orientations of the individual chains of the network, which was not available for arbitrary 3-D deformations until very recent (Wu and Van der Giessen, 1993a).

Various simplified averaging procedures to obtain the network response have been proposed (see Wu and Van der Giessen, 1993a). Among these simplified models, the so-called three-chain model, originally suggested by James and Guth (1943), has become the most widespread and almost standard non-Gaussian network model for rubber elasticity. This model assumes that a network containing n chains per unit volume is equivalent to three independent sets of $n/3$ single chains in three orthogonal directions. Thus, the actual spatial distribution of chains is sampled in three orthogonal orientations. Similarly, Treloar (1946) proposed the idea of a four-chain Gaussian network representation (Flory and Rehner, 1943) to sample four spatial chain orientations. Very recently, Arruda and Boyce (1991, 1993a) proposed a so-called eight-chain model, which considers a set of eight chains connecting the central junction point and each of the eight corners of the unit cube. Obviously, these models are but approximate representations of the actual spatial distribution of molecular chains. All these models can be regarded to sample a set of particular directions among all possible orientations. More precisely, the three-chain model would overestimate the contribution of the chain collection oriented along the direction of major principal extension, while the eight-chain model would underestimate the stiffness of the network (Dahoun *et al.*, 1993). The four-chain model has the major draw-back that it does not exhibit the symmetry required of the principal strain space (Arruda and Boyce, 1991).

The full network formulation by Wu and Van der Giessen (1992a, 1993a) accounts accurately for the actual spatial orientation distribution of molecular chains. Treloar and Riding (1979a) had already developed a rubber elasticity theory based on such a full network description, but their considerations were limited to deformations with biaxial extension along fixed axes under plane stress conditions. Our model extend their theory to a general formulation valid for 3-D deformation processes.The modelling centres around a general treatment of the orientation distribution of molecular chains and their evolution as deformation progresses. This description utilizes the idea of Chain Orientation Distribution Function (CODF), which is governed by balance equations that express physically well-understood conservation principles. Assuming the network to deform affinely with the deformation of the continuum it is embedded in, closed-form solutions has been derived for this CODF, which thus contain the complete information of the orientation distribution of molecular chains at any stage of the deformation. This solution is then used to develop the rubber elasticity model by averaging out the contribution to the free energy of individual chains over all chain orientations. The model has been found to be able to pick up the mechanical behaviour of rubbers at various different large deformations (Dahoun, 1992; Wu and Van der Giessen, 1993a); and has been successfully used to model the orientation hardening behaviour of large inelastic deformations of amorphous glassy polymers (see e.g. Wu and Van der Giessen, 1993a, b, c). G'Sell and Dahoun (1993) and Dahoun *et al.* (1993) used the full network model to describe the amorphous phase responses in their composite model for large plastic deformation of semi-crystalline polymers.

In Section 3.2, we re-formulate the full network model for rubber elasticity in a more efficient and more micromechanics motivated manner. The so-derived equations are mathematically equivalent to those given in Wu and Van der Giessen (1993a). But, the new representation of the model allows us to avoid calculating principal stretches and principal directions of deformations.

The development of molecular chain segment orientation in rubber-like materials under deformation has been extensively studied experimentally, often by the optical anisotropy or birefringence [see e.g. Treloar, 1975; Brown and Windle, 1984; Mitchell *et al.*, 1985]. In Section 3.3, a so-called non-Gaussian full network model for rubber photoelasticity is proposed. The derivation of this optical theory proceeds along lines parallel to the treatment of the full network model for rubber elasticity. The essential modification is the introduction of directional polarizabilities into the individual links of the idealized randomly-jointed chain. Again, Treloar and Riding (1979b) had already developed a non-Gaussian optical theory based on such a full network description; but, just as for the mechanical properties, their considerations were limited to deformations with biaxial extension along fixed axes under plane stress conditions. Our model extend their theory to a general formulation valid for 3-D deformation processes. For the purpose of comparison, we will also give two simplified optical theories corresponding to the so-called three-chain model [see e.g. Wang and Guth, 1952] and eight-chain model (Arruda and Boyce, 1993a) originally for rubber elasticity. The full network model for rubber photoelasticity requires numerical integration; an approximation to the numerical results will be given, which is based on the three-chain and eight-chain representations. Verification with some experimental results from literature is provided both for the mechanical and for optical behaviour of a few rubber materials.

Tensors will be denoted by bold-face letters. The tensor product is denoted by $\otimes$ and the following operation for second-order tensors applies ($\mathbf{a} = a_{ij}\mathbf{e}_i \otimes \mathbf{e}_j$, $\mathbf{b} = b_{ij}\mathbf{e}_i \otimes \mathbf{e}_j$, $\mathbf{e}_i$ being a Cartesian basis): $\mathbf{ab} = a_{ik}b_{kj}\mathbf{e}_i \otimes \mathbf{e}_j$. Superscripts T and -1 denote the transverse and inverse of a second-order tensor, respectively. The trace is denoted by tr. The three principal values of $\mathbf{a}$ are denoted by $\tilde{a}_i$ where the superposed ~ reminds one of the principal value of the quantity.

3.2. THE FULL NETWORK MODEL FOR RUBBER ELASTICITY

In (Wu and Van der Giessen, 1993a) we introduced a so-called molecular Chain Orientation Distribution Function (CODF), denoted by $C(\theta, \varphi; t)$, such that the relative density of molecular chains, at some instant t, whose $\mathbf{r}$-vector orientation falls in the range between (θ, φ) and $(\theta + \mathrm{d}\theta, \varphi + \mathrm{d}\varphi)$ is given by $C(\theta, \varphi; t)\sin\theta\,\mathrm{d}\theta\,\mathrm{d}\varphi$. Note that $\sin\theta\,\mathrm{d}\theta\,\mathrm{d}\varphi$ is the area on a unit sphere spanned by the interval $(\mathrm{d}\theta, \mathrm{d}\varphi)$ and that t is just a time-like parameter. With n denoting the number of chains per unit volume, the actual number of chains between (θ, φ) and $(\theta + \mathrm{d}\theta, \varphi + \mathrm{d}\varphi)$ then is

$$\mathrm{d}n = nC(\theta, \varphi; t)\sin\theta\,\mathrm{d}\theta\,\mathrm{d}\varphi. \tag{3.1}$$

For a virgin, unstrained material the orientation of network chains can usually be considered to be distributed in a random fashion; then C will be independent of θ and φ, and the material's response is instantaneously isotropic. When the material is deformed, all chains are stretched and, at the same time, rotated. Hence, the CODF will develop into a nonuniform distribution, which can be quite severe as has been demonstrated in Wu and Van der Giessen (1993a). Thus, texture development in the sense of molecular chain distributions is described in this model in terms of this CODF.

Assuming the network to deform affinely with some three dimensional deformation process represented by the deformation gradient tensor $\mathbf{F}$ of the continuum it is embedded in, each chain's end-to-end vector $\mathbf{r}_0$ in the initial state is taken to be strained and rotated to the vector $\mathbf{r}$ in the current state in an affine manner, i.e. $\mathbf{r} = \mathbf{F}\mathbf{r}_0$. It can be shown (Wu and Van der Giessen, 1993a) that in an arbitrary state of deformation, the CODF for an initially random network can be expressed as follows:

$$C = C_0 \lambda_c^3(\theta, \varphi; \lambda_i), \tag{3.2}$$

where $C_0 = 1/4\pi$ is the initial uniform distribution, and where $\lambda_c^3(\theta, \varphi; \lambda_i)$ is the stretch of an individual chain whose $\mathbf{r}$-vector has an orientation (θ, φ) with respect to the Eulerian triads $\mathbf{e}_i^E$ (i.e. the principal stretch directions in the current configuration), and λ_i are the principal stretches. Here, we have substituted the principal stretches as the time-like parameter t in the previous expressions for the CODF. This is possible since, as a consequence of the affine deformation assumption, the distortion of the network is independent of the rate of deformation, so that t only needs to be some monotonic parameter. Identifying t with λ_i will turn out to be convenient for further development (Wu and Van der Giessen, 1993a). For a detailed derivation of (3.2) we refer to Wu and Van der Giessen (1993a). It is clear that the Eulerian triads themselves rotate during the deformation process. Therefore, we have to re-calculate the principal stretches λ_i and the corresponding principal directions $\mathbf{e}_i^E$ at each stage of the deformation process. Before proceeding it is noted that since we assume the network to be incompressible, the deformation gradient tensor satisfies $\det \mathbf{F} = 1$.

It is noted that the CODF in (3.2) is directly related to the stretch of an individual chain and is determined completely through the deformation ellipsoid, which is independent of the coordinate system used. Therefore, we can rewrite (3.2) in the form

$$C = C_0 \lambda_c^3(\Theta, \Phi; \mathbf{F}), \tag{3.3}$$

where (Θ, Φ) is the orientation of the $\mathbf{r}$-vector of an individual chain in the current state with respect to a fixed triad $\mathbf{e}_i$ (see Fig. 3.1.), and where $\mathbf{F}$ is the deformation gradient tensor. The chain stretch λ_c can be obtained from $\mathbf{F}$ by

$$\lambda_c^{-2} = \mathbf{m} \, (\mathbf{F}\,\mathbf{F}^T)^{-1} \mathbf{m}. \tag{3.4}$$

Here, $\mathbf{m}$ is the unit vector $\mathbf{m} = \mathbf{r}/r = m_i \mathbf{e}_i$ $(r = \|\mathbf{r}\|)$ along the end-to-end vector $\mathbf{r}$, in the current deformed state with components

$$m_1 = \sin\Theta\cos\Phi, \quad m_2 = \sin\Theta\sin\Phi, \quad m_3 = \cos\Theta. \tag{3.5}$$

The actual number of chains between (Θ, Φ) and $(\Theta + d\Theta, \Phi + d\Phi)$ then is

$$dn = n C_0 \lambda_c^3(\Theta, \Phi; \mathbf{F}) \sin\Theta \, d\Theta \, d\Phi. \tag{3.6}$$

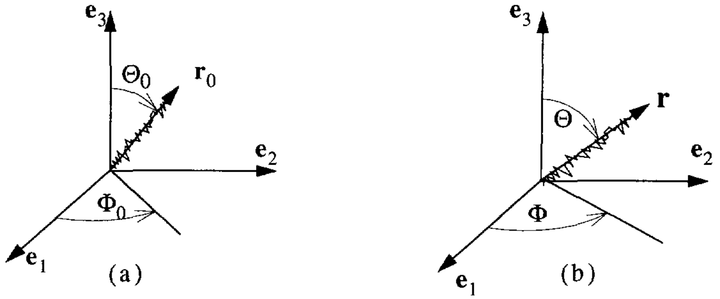

Fig. 3.1. A single chain in unstrained (a) and strained (b) state; definition of geometric quantities.

In order to represent the mechanical properties, let us consider a single chain between two junction points, with its end-to-end vector **r** in the current state being specified by angular coordinates Θ and Φ with respect to some fixed frame of reference defined by the set of orthonormal base vectors $\mathbf{e}_i$ (see Fig. 3.1.). We further assume that this single chain has a given stretch λ_c in current state. If the chain contains N links of length l, the length of the unstrained free chain r_0 is given by the root-mean-square value $\sqrt{N}\,l$. By considering the statistical distribution of possible link angles at a given stretch λ_c, Kuhn and Grun (1942) were the first to derive the well-known non-Gaussian relationship between force f_c and stretch λ_c for the stretched chain in the form

$$f_c = \frac{kT}{l}\mathcal{L}^{-1}\left(\frac{\lambda_c}{\sqrt{N}}\right), \tag{3.7}$$

where k is Boltzmann's constant, T is absolute temperature and $\mathcal{L}$ is the Langevin function defined by $\mathcal{L}(\beta) = \coth\beta - 1/\beta$. By noting that $r = \lambda_c r_0 = \lambda_c\sqrt{N}l$, while $1/n$ is the volume per chain and $1/(nr)$ is the cross section area of the chain in the current state, the equation (3.7) can be transformed into a relationship between the Cauchy stress σ_c, defined by $\sigma_c = f_c rn$, acted on the continuum in which the chain is embedded and the stretch in the form

$$\sigma_c = C^R\sqrt{N}\lambda_c\mathcal{L}^{-1}\left(\frac{\lambda_c}{\sqrt{N}}\right), \tag{3.8}$$

where $C^R = nkT$ is known as the rubbery modulus. Now, introduce a so-called micro-stress tensor $\boldsymbol{\sigma}_c$ by

$$\boldsymbol{\sigma}_c = \sigma_c(\mathbf{m}\otimes\mathbf{m}) - p\mathbf{I}, \tag{3.9}$$

which can be interpreted as the contribution of the single chain to the stress of the network. The hydrostatic pressure p is included because of incompressibility. The overall or macro-stress tensor $\boldsymbol{\sigma}$ of the network is then obtained by simply averaging the micro-stress tensor $\boldsymbol{\sigma}_c$ of the individual chains, i.e.

$$\boldsymbol{\sigma} = \frac{1}{n}\int\boldsymbol{\sigma}_c\,\mathrm{d}n. \tag{3.10}$$

With dn being given by (3.6) and the CODF by (3.3), we find

$$\boldsymbol{\sigma} = \frac{1}{4\pi}\int_0^{\pi}\int_0^{2\pi} \boldsymbol{\sigma}_c \lambda_c^3 \sin\Theta \, d\Theta \, d\Phi - p\mathbf{I}\,; \tag{3.11}$$

and with (3.8) and (3.9), we finally obtain for the Cartesian stress components, $\boldsymbol{\sigma} = \sigma_{ij}\mathbf{e}_i \otimes \mathbf{e}_j$,

$$\sigma_{ij} = \frac{1}{4\pi} C^R \sqrt{N} \int_0^{\pi}\int_0^{2\pi} \lambda_c^4 \mathcal{L}^{-1}\left(\frac{\lambda_c}{\sqrt{N}}\right) m_i m_j \sin\Theta \, d\Theta \, d\Phi - p\delta_{ij} \tag{3.12}$$

with λ_c determined from (3.4) as a function of the deformation gradient tensor $\mathbf{F}$ and the orientation (Θ, Φ). The hydrostatic pressure p is left unspecified by the constitutive equations and is to be determined from the boundary conditions.

The equations (3.12) are mathematically equivalent to those given in Wu and Van der Giessen (1993a). But, the new representation of the model allows us to avoid calculating principal stretches and principal stretch directions for arbitrary 3-D deformation. Furthermore, this micromechanics motivated new derivation will turn out to be convenient for further development of the so-called full network model for rubber photoelasticity in the next section.

3.3. IMPROVED NEWORK MODELS FOR RUBBER PHOTOELASTICITY

It is well-known that many materials show the phenomenon of double refraction, which arises from the fact that they are optically anisotropic. In other words, they have different refractive indices, or polarizabilities in different directions. The refractive index of a material is a function of its response to the electric field in the light wave, or, more specifically, of its polarizability, which is defined as the induced dipole moment per unit field strength. Rubber-like materials are usually assumed to be random in their structure and isotropic in their physical properties; such materials do not show double refraction in the initial undeformed state. But in the deformed state, their structures are no longer random; they cease to be isotropic and begin to show double refraction or birefringence.

Usually, developing a network model for rubber photoelasticity follows closely the lines taken in the treatment of the corresponding network model for rubber elasticity. The essential modification is the introduction of directional polarizabilities into the individual links of the idealized randomly-jointed chain. First, the optical properties of the single chain are determined as a function of its length or stretch. Next, the contribution of an individual chain to the polarizability of the network is determined. Finally, the total polarizability of the network is obtained by integration over all the chains.

3.3.1. Full network model—Eulerian form

Consider a single chain at a given stretch λ_c in the current deformed state, with its unit vector $\mathbf{m}$ being specified by angular coordinates Θ and Φ with respect to the base vectors $\mathbf{e}_i$ (see Fig. 3.1.). Kuhn and Grun (1942) had shown that a stretched chain can be characterized by polarizabilities γ_1 in the direction of $\mathbf{m}$ and γ_2 in directions $\mathbf{l}$ and $\mathbf{n}$ perpendicular to $\mathbf{m}$. These are given by

$$\gamma_1 = N\left(\alpha_1 - (\alpha_1 - \alpha_2)\frac{2\lambda_c/\sqrt{N}}{\mathcal{L}^{-1}(\lambda_c/\sqrt{N})}\right),$$

$$\gamma_2 = N\left(\alpha_2 + (\alpha_1 - \alpha_2)\frac{\lambda_c/\sqrt{N}}{\mathcal{L}^{-1}(\lambda_c/\sqrt{N})}\right), \tag{3.13}$$

in terms of the polarizabilities α_1 and α_2 parallel and perpendicular to the link direction respectively. The optical anisotropy or difference of principal polarizabilities may be written as

$$\gamma_1 - \gamma_2 = N(\alpha_1 - \alpha_2)P(\lambda_c), \quad P(\lambda_c) = 1 - \frac{3\lambda_c/\sqrt{N}}{\mathcal{L}^{-1}(\lambda_c/\sqrt{N})} \quad . \tag{3.14}$$

The contribution of an individual chain to the polarizability of the network can be determined by introducing a so-called chain polarizability tensor $\mathbf{B}_c$ in the form

$$\begin{aligned}\mathbf{B}_c &= \gamma_1 \mathbf{m} \otimes \mathbf{m} + \gamma_2 \mathbf{n} \otimes \mathbf{n} + \gamma_2 \mathbf{l} \otimes \mathbf{l} \\ &= (\gamma_1 - \gamma_2)\,\mathbf{m} \otimes \mathbf{m} + \gamma_2 \mathbf{I}\end{aligned} \tag{3.15}$$

The overall polarizability tensor $\mathbf{B}$ of the network is then readily obtained by simple summing the chain polarizability tensor $\mathbf{B}_c$ of the individual chains, i.e.

$$\mathbf{B} = \int \mathbf{B}_c \,\mathrm{d}n. \tag{3.16}$$

With $\mathrm{d}n$ by (3.6) and the CODF according to (3.3), we obtain

$$\mathbf{B} = \frac{n}{4\pi}\int_0^{\pi}\int_0^{2\pi} \mathbf{B}_c \lambda_c^3 \sin\Theta \,\mathrm{d}\Theta \,\mathrm{d}\Phi. \tag{3.17}$$

Using (3.13) and (3.15), we find for the Cartesian polarizability tensor components, $\mathbf{B} = B_{ij}\mathbf{e}_i \otimes \mathbf{e}_j$,

$$B_{ij} = \frac{n}{4\pi}\int_0^{\pi}\int_0^{2\pi} \lambda_c^3 (\gamma_1 - \gamma_2)\, m_i m_j \sin\Theta \,\mathrm{d}\Theta \,\mathrm{d}\Phi + n\gamma_2 \delta_{ij} \tag{3.18}$$

with λ_c being given by (3.4) and m_i by (3.5). The normalized differences of polarizabilities in two orthogonal directions i and j are then given by

$$\begin{aligned}\beta_{ii} - \beta_{jj} &= \frac{B_{ii} - B_{jj}}{n(\alpha_1 - \alpha_2)} \\ &= \frac{N}{4\pi}\int_0^{\pi}\int_0^{2\pi} \lambda_c^3 P(\lambda_c)\,(m_i m_i - m_j m_j)\sin\Theta \,\mathrm{d}\Theta \,\mathrm{d}\Phi, \quad (\text{no sum})\end{aligned} \tag{3.19}$$

with $P(\lambda_c)$ being given in (3.14b).

3.3.2. *Full network model—Lagrangian form*

The full network model for rubber photoelasticity derived above, can also be developed in the initial state, i.e. in a Lagrangian form instead of in the foregoing Eulerian form. The Lagrangian form can be obtained in a rather straightforward matter by employing a direct transformation of (3.17). Without going into the details, we give only the result in the form

$$B_{ij} = \frac{n}{4\pi}\int_0^{\pi}\int_0^{2\pi} (\gamma_1 - \gamma_2) F_{ik}F_{jl}m_{0k}m_{0l}\sin\Theta_0 \mathrm{d}\Theta_0 \mathrm{d}\Phi_0 + n\gamma_2\delta_{ij} \tag{3.20}$$

with F_{ij} being the Cartesian components of the deformation gradient tensor $\mathbf{F}$. Here, the integrations are performed in the initial orientation space (Θ_0, Φ_0); and $m_{01} = \sin\Theta_0\cos\Phi_0$, $m_{02} = \sin\Theta_0\sin\Phi_0$ and $m_{03} = \cos\Theta_0$ are the components of the unit vector $\mathbf{m}_0 = \mathbf{r}_0/r_0 = m_{0k}\mathbf{e}_k$ along the end-to-end vector $\mathbf{r}_0$ in the initial state (see Fig. 3.1). It is noted that the chain stretch λ_c in (14) should in this case be determined in the initial state according to $\lambda_c^2 = \mathbf{m}_0(\mathbf{F}^T\mathbf{F})\mathbf{m}_0$.

It is noted that from (3.20) we can easily obtain the normalized differences of polarizabilities $\beta_{ii} - \beta_{jj}$ (no sum), which are similar to those given by Treloar and Riding (1979b). However, Treloar and Riding (1979b) limited their attention to 2-D deformations with fixed principal axes of stretching. Our formulation is valid for arbitrary 3-D deformations; for the 2-D deformations mentioned, the Lagrangian form of our full network model reduces to that in Treloar and Riding (1979b). It is also noted that in the Lagrangian approach, the CODF is not needed at all for the computation of the polarizability tensor of the network. However, the CODF in itself is an essential source of information about the actual orientation distribution of molecular chains at any stage of a general 3-D state of deformation (Wu and Van der Giessen, 1993a).

3.3.3. *Simplified models*

In this paper, we shall consider two simplified network models for rubber photoelasticity, namely the three-chain model and eight-chain model. The three-chain model was originally suggested by James and Guth (1943) for rubber elasticity and assumes that a network containing n chains per unit volume is equivalent to three independent sets of $n/3$ chains per unit volume parallel to the Eulerian principal axes $\mathbf{e}_i^E$. Using the notation $\tilde{B}_i^{\text{3-ch}}$ for the principal network polarizabilities, we thus have

$$\mathbf{B}^{\text{3-ch}} = \sum_{i=1}^{3} \tilde{B}_i^{\text{3-ch}} (\mathbf{e}_i^E \otimes \mathbf{e}_i^E) \tag{3.21}$$

The normalized differences of the principal network polarizabilities had been given in the form (see e.g. Treloar and Riding, 1979b)

$$\frac{\tilde{B}_i^{3\text{-ch}} - \tilde{B}_j^{3\text{-ch}}}{n(\alpha_1 - \alpha_2)} = \frac{1}{3} N [P(\lambda_i) - P(\lambda_j)] , \tag{3.22}$$

where λ_i are the principal stretches. The Cartesian components, $\mathbf{B}^{3\text{-ch}} = B_{ij}^{3\text{-ch}} \mathbf{e}_i \otimes \mathbf{e}_j$, can be determined from the principal values $\tilde{B}_i^{3\text{-ch}}$ and principal directions $\mathbf{e}_i^{\mathrm{E}}$ by a standard tensor transformation argument. However, the results cannot be represented by general mathematical formulae for arbitrary 3-D deformations.

The eight-chain model for rubber elasticity was proposed by Arruda and Boyce (1991, 1993a) and considers a set of eight chains connecting the central junction point and each of eight corners of the unit cube. The polarizability tensor according to the eight-chain model, $\mathbf{B}^{8\text{-ch}}$, is found as

$$\mathbf{B}^{8\text{-ch}} = n \frac{(\gamma_1 - \gamma_2)}{3\lambda_{\mathrm{c}}^2} \mathbf{F}\mathbf{F}^{\mathrm{T}} + n\gamma_2 \mathbf{I} \tag{3.23}$$

with

$$\lambda_{\mathrm{c}} = \sqrt{\frac{1}{3} \operatorname{tr} (\mathbf{F}\,\mathbf{F}^T)} \,. \tag{3.24}$$

The tensor $\mathbf{B}^{8\text{-ch}}$ can be represented as $\mathbf{B}^{8\text{-ch}} = B_{ij}^{8\text{-ch}} \mathbf{e}_i \otimes \mathbf{e}_j$. It may be shown that

$$\begin{aligned} \beta_{ii}^{8\text{-ch}} - \beta_{jj}^{8\text{-ch}} &= \frac{B_{ii}^{8\text{-ch}} - B_{jj}^{8\text{-ch}}}{n(\alpha_1 - \alpha_2)} \\ &= \frac{N}{3\lambda_{\mathrm{c}}^2} P(\lambda_c) \, (F_{ik} F_{ik} - F_{jk} F_{jk}) \,, (\text{no sum for } i \text{ and } j) \,. \end{aligned} \tag{3.25}$$

3.3.4. Approximation of the full network model

Comparing the three- and eight-chain samplings with the actual three-dimensional initial random distribution of molecular chains, we expected that, as in the network models for rubber elasticity (Wu and Van der Giessen, 1993a), the three-chain model would overestimate the actual optical anisotropy of the network, while the eight-chain model would probably give a lower bound. Indeed, as will be demonstrated in the next section, the optical response predicted by our full network model (3.18) or (3.20) is, for the same values of N and n, always in-between that predicted by the three-chain model and eight-chain model, respectively. However, the integrations involved in (3.18) and (3.20) require a rather time-consuming numerical procedure. All these observations motivated us to search for an approximation of the full integration by combining the three-chain and eight-chain models. One possibility is a simple linear combination,

$$\mathbf{B} = (1 - \rho) \mathbf{B}^{3\text{-ch}} + \rho \mathbf{B}^{8\text{-ch}} , \tag{3.26}$$

where the parameter ρ may be a constant or related to some other physical quantity which is, for instance, related to deformation process. In this paper, we consider ρ to be related to the maximal principal stretch $\lambda_{\max} = \max(\lambda_1, \lambda_2, \lambda_3)$ by

$$\rho = 0.62 \frac{\lambda_{\max}}{\sqrt{N}}, \tag{3.27}$$

where the factor 0.62 was chosen to give the best correlation with full integrations of (3.18) and (3.20). In this way, the eight-chain contribution in (3.23) becomes increasingly important when $\lambda_{\max}$ approaches the limit stretch $\sqrt{N}$. The form (3.26) is similar to our previous proposition for the full network stress in rubber elasticity in relation to that according to three- and eight-chain models (Wu and Van der Giessen, 1993a).

3.3.5. *Calculation of birefringences*

In an optical anisotropic medium the properties are represented by the refractive index ellipsoid, the principal axes of which represent the three principal indices $\tilde{\mu}_i$ in three mutually perpendicular directions. This in turn is related to the polarizability ellipsoid, whose axes correspond to the principal polarizabilities $\tilde{B}_i$, and coincide in direction with the axes of the refractive index ellipsoid. The conversion of polarizabilities $\tilde{B}_i$ (per unit volume) to refractive indices $\tilde{\mu}_i$ makes use of the Lorentz-Lorenz relation

$$\frac{\tilde{\mu}_i^2 - 1}{\tilde{\mu}_i^2 + 2} = \frac{4\pi}{3} \tilde{B}_i. \tag{3.28}$$

Since the differences of refractive index relative to the mean value μ_0 are generally small, it may be shown that,

$$\frac{\tilde{\mu}_i^2 - 1}{\tilde{\mu}_i^2 + 2} \approx \left[\frac{\tilde{\mu}_0^2 - 1}{\tilde{\mu}_0^2 + 2} - 6 \frac{\mu_0^2}{(\mu_0^2 + 2)^2} \right] + 6 \frac{\mu_0}{(\mu_0^2 + 2)^2} \tilde{\mu}_i,$$

so that

$$\tilde{\mu}_i = \Delta\mu_0 \tilde{B}_i - M_0 \tag{3.29}$$

with

$$\Delta\mu_0 = \frac{4\pi}{3} \frac{(\mu_0^2 + 2)^2}{6\mu_0}, \qquad M_0 = \frac{(\mu_0^2 - 1)(\mu_0^2 + 2) - 6\mu_0^2}{(\mu_0^2 + 2)^2}.$$

Applying the relationship (3.29) for all three principal directions, we find that the polarizability tensor B and the refractive index tensor μ, formed from the principal values $\tilde{\mu}_i$, are related through

$$\boldsymbol{\mu} = \Delta\mu_0 \mathbf{B} - M_0 \mathbf{I}. \tag{3.30}$$

Since the polarizability ellipsoid is coaxial with the refractive index ellipsoid, the birefringence for propagation of light along any direction is determined by the polarizabilities in the two transverse directions (directions of electric vector). Therefore, for instance, propagation along $\mathbf{e}_3$ involves the difference of polarizabilities $B_{11} - B_{22}$. Using (3.30), we obtain equations in the form

$$\mu_{ii} - \mu_{jj} = \frac{4\pi}{3}\frac{(\mu_0^2+2)^2}{6\mu_0}(B_{ii} - B_{jj}), \qquad \text{(no sum)}, \tag{3.31}$$

or

$$\mu_{ii} - \mu_{jj} = \Delta\mu_N(\beta_{ii} - \beta_{jj}), \qquad \text{(no sum)} \tag{3.32}$$

with

$$\Delta\mu_N = \frac{4\pi}{3}\frac{(\mu_0^2+2)^2}{6\mu_0} n(\alpha_1 - \alpha_2).$$

Here, μ_{ij} are the components of the refractive index tensor $\boldsymbol{\mu}$ defined by $\boldsymbol{\mu} = \mu_{ij}\mathbf{e}_i \otimes \mathbf{e}_j$.

3.4. RESULTS

The full network model for rubber elasticity has been used to describe the large strain elastic behaviour of rubber-like materials (Wu and Van der Giessen, 1993a). Detailed comparisons with experimental results and with two approximate models have been provided for different types of deformation and rubbers (Wu and Van der Giessen, 1993a). As an additional example of the application of the model, we study the mechanical responses to uniaxial tension and pure shear of a vulcanized rubber reported by Treloar (1944), but, according to the new derivation of the full network model given in section 3.2. This also serves a numerical check on the present network formulation compared to the previous one (Wu and Van der Giessen, 1993a). At each stage of the deformation, the double integral in the full network relation (3.12) is evaluated by first noting that due to symmetry only the intervals $\Theta \in [0, \pi/2]$, $\Phi \in [0, \pi]$ need to be considered, then subdividing that area into a number of cells and integrating within each cell using Gaussian quadrature. Recursive refinement is applied for each cell until the integral is obtained with a relative error of 10^{-5}.

As pointed out by Wu and Van der Giessen (1993a), the full network model as well as the simplified three-chain model and eight-chain model are able to reproduce experimental rubber stress-strain data for a certain deformation and material by selecting the material parameters N and C^R for the given model. However, a more important aspect appears to be the description of the network response under different states of deformation. In order to assess the deformation dependence, we take the following procedure [see also Arruda and Boyce (1993a), Wu and Van der Giessen (1993a)]. The network parameters N and C^R are fitted from uniaxial tension data, and are then used to predict pure shear. Figure 3.2 shows results for uniaxial tension in terms of the nominal stress f or load per unit undeformed area as a function of the uniaxial stretch λ. The values of $N = 62$ and $C^R = 0.3\text{MPa}$ were found to give the best correlation with the uniaxial tension data (Treloar, 1944). The predicted results of pure shear using these values of the parameters are given in Fig. 3.3. The pure shear is characterized by the principal stretches $\lambda_1 = \lambda, \lambda_2 = 1, \lambda_3 = 1/\lambda$ along fixed directions, while the material is in a state of plane stress, i.e. $\sigma_{33} = 0$. The figure shows the load in the stretching direction, i.e. $f = \sigma_{11}/\lambda$. It is observed that the full network model predicts the different behaviour in pure shear well over the entire experimental range.

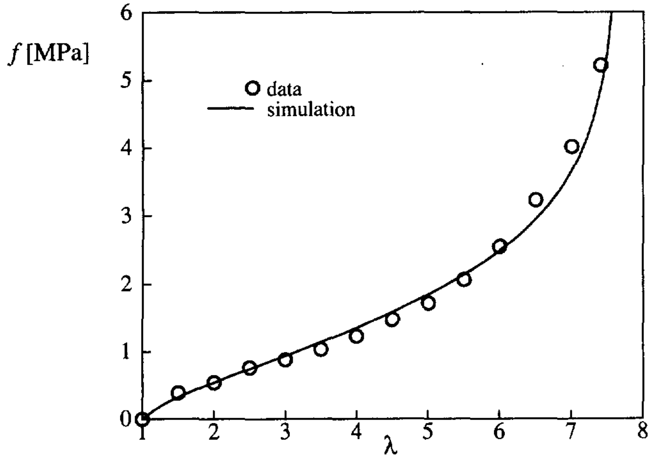

Fig. 3.2. Load vs. stretch diagram for uniaxial tension of a vulcanized rubber according to the full network model for rubber elasticity with $N = 62$ and $C^R = 0.3$ MPa. The experimental data is taken from Treloar (1944).

We proceed by studying the optical properties of rubbers in terms of the full network model as well as the simplified three-chain and eight-chain models for rubber photoelasticity. The numerical procedure of the integrations (3.18) and (3.20) involved in the full network model is similar to that in the mechanical description Appendix (3.12) of the full network given above. However, the integrals in equations (3.18) and (3.20) are 'well-behaved' over the whole of the specified ranges (Treloar and Rinding, 1979b). This is due to the fact that whereas the tensile stress σ_c on the single chain tends to infinity as its stretch λ_c approaches the limit stretch N [see Eq. (3.8)], the optical anisotropy of the chain remains finite and reaches the value $n(\alpha_1 - \alpha_2)$ [see Eqs. (3.14)]. As a result, the amount of computation required to achieve any degree of accuracy is notably less for the optical than for the mechanical problem.

Figure 3.4 shows the predicted difference in polarizability for uniaxial tension in the $\mathbf{e}_1$ direction with principal stretches $\lambda_1 = \lambda, \lambda_2 = \lambda_3 = \lambda^{-2}$. The value $N = 25$ was used for all three models; it was simply used as a representative value of N. What this result clearly shows is that relative to the full network model for rubber photoelasticity, the simplified three-chain model tends to overestimate the optical anisotropy at large stretches, while the eight-chain approximation tends to underestimate it. It is also observed that all models give virtually identical predictions for small stretches up to $\lambda \approx 2.5$ (or roughly 50% of the limit stretch). The difference at large stretches seems to be associated with the different limit stretches of the complete network. The stretching according to the three-chain model is limited directly by the tensile stretch $\lambda_L = \sqrt{N}$ of the chains parallel to the tensile direction, while the overall network limiting stretch for the eight-chain model exceeds λ_L. It is seen that the approximation (3.26) for the full network optical response is indeed very accurate up to very large stretches.

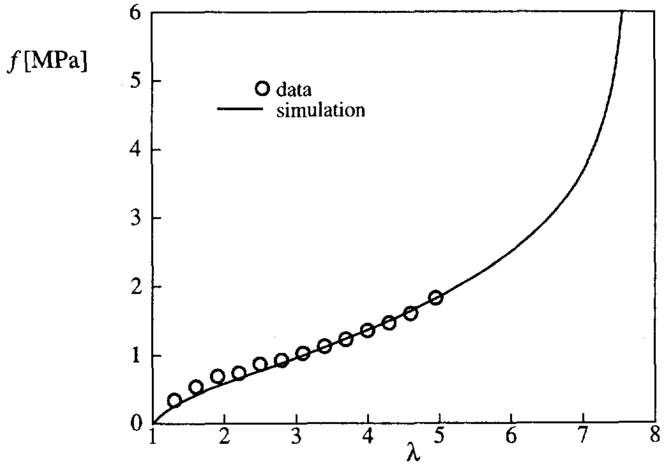

Fig. 3.3. Load vs. stretch diagram for pure shear of a vulcanized rubber according to the full network model for rubber elasticity with $N = 62$ and $C^R = 0.3$ MPa. The experimental data is taken from Treloar (1944).

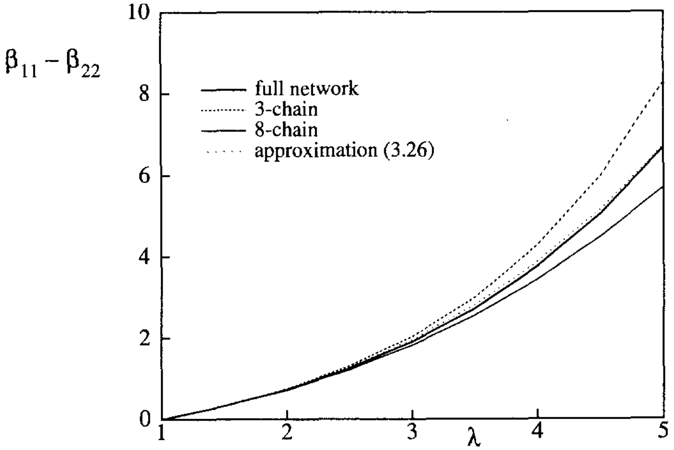

Fig. 3.4. Predicted normalized optical anisotropy vs. stretch diagram for uniaxial tension according to different network models for rubber photoelasticity with $N = 25$.

Next, we consider the case of simple (and *not* pure) shear, where the deformation gradient tensor $\mathbf{F}$ is given by $\mathbf{F} = \mathbf{I} + \Gamma \mathbf{e}_1 \otimes \mathbf{e}_2$. In contrast to uniaxial tension where the principal stretch directions are fixed in space, the principal stretch directions in simple shear rotate constantly during the deformation process. As a result, the prediction of the optical anisotropy in simple shear is much more involved than in the deformations with fixed principal stretch directions. Figure 3.5 shows the predicted optical anisotropy of simple shear according to the full network model, three-chain and eight-chain network models for rubber phtoelasticity. The differences in predicted normalized optical anisotropy $\beta_{11} - \beta_{33}$ between the network models are similar to those presented in Fig. 3.4 for uniaxial tension. Compared with the CODF in simple shear presented in Wu and Van der Giessen (1993a), it is found that all models support the observation that molecular chains rotate towards the shear direction. Again, the approximation (3.26) for the full network optical response in terms of $\beta_{11} - \beta_{33}$ is very accurate up to very large shear strains.

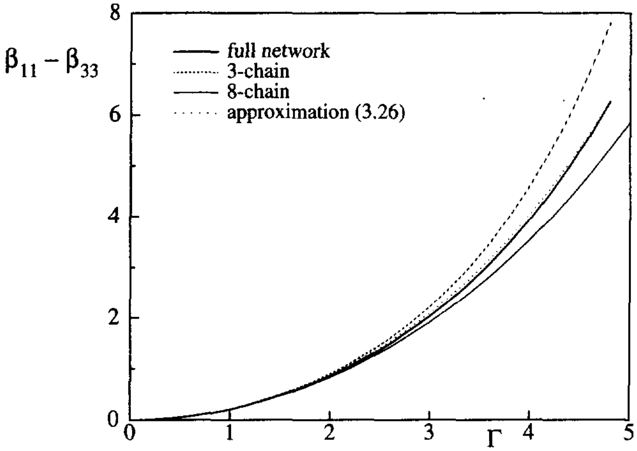

Fig. 3.5. Predicted normalized optical anisotropy $\beta_{11} - \beta_{33}$ vs. shear strain diagram during simple shear according to different network models for rubber photoelasticity with $N = 25$.

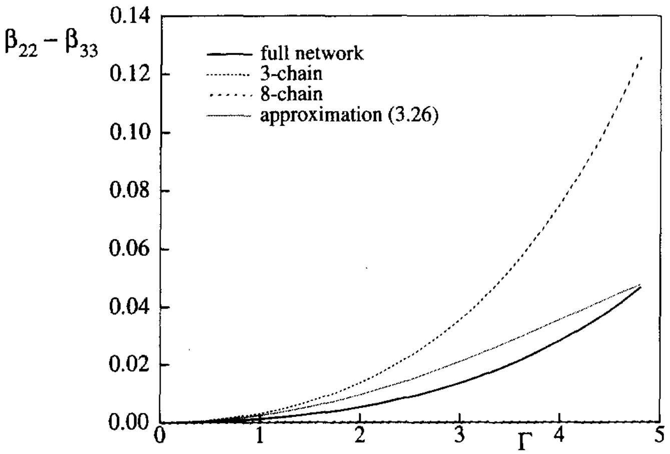

Fig. 3.6. Development of secondary optical anisotropy $\beta_{22} - \beta_{33}$ during simple shear according to different network models for rubber photoelasticity with $N = 25$.

It is well-known that the secondary normal stresses σ_{11} and σ_{22} during simple shear are mainly due to the development and subsequent rotation of the induced anisotropy; and that the prediction of these mechanical phenomena generally shows a rather strong dependence on the constitutive models [see e.g. Wu and Van der Giessen (1993a, c)]. It is expected that the secondary order effects in optical anisotropies such as $\beta_{22} - \beta_{33}$ will also strongly depend on the constitutive models for rubber photoelasticity. Figure 3.6 shows the predicted secondary optical anisotropy $\beta_{22}-\beta_{33}$ during simple shear. Although the predicted absolute values of $\beta_{22}-\beta_{33}$ are much smaller than those of $\beta_{11}-\beta_{33}$, the relative differences in predicted $\beta_{22}-\beta_{33}$ between the network models are much larger than those in predicted $\beta_{11}-\beta_{33}$. In fact, according to the eight-chain model, $\beta_{22}-\beta_{33}\equiv 0$ during simple shear [see Eqs. (3.25)]. This fact is also the reason why the approximation (3.26) for the full network optical response in terms of $\beta_{22}-\beta_{33}$ is not very good in this special case.

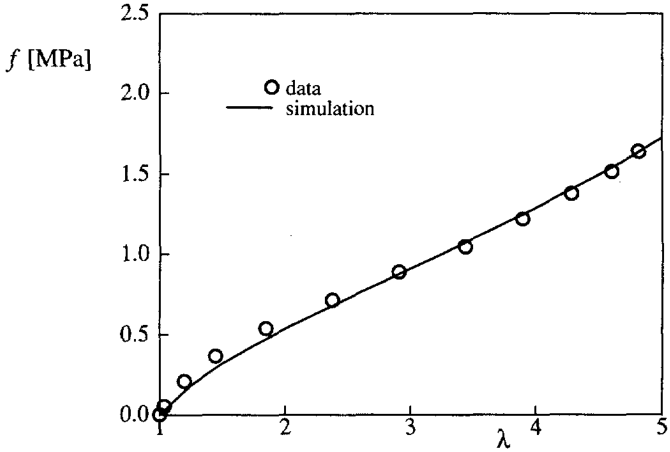

Fig. 3.7. Load response to uniaxial tension of a vulcanized styrene-butadiene rubber (SBR) according to the full network model for rubber elasticity with $N = 75$ and $C^R = 0.3$ MPa. The experimental data is taken from Doherty *et al.* (1980).

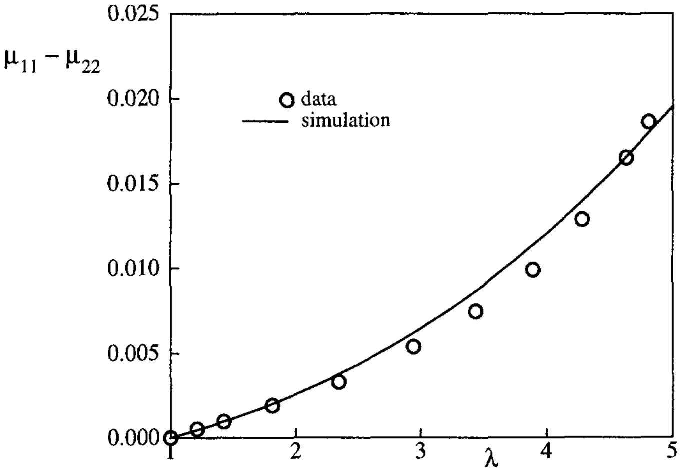

Fig. 3.8. Predicted birefringence in uniaxial tension of a vulcanized styrene-butadiene rubber (SBR) according to the full network for rubber photoelasticity with $N = 75$ and $\Delta\mu_N = 3.6\times10^{-3}$. The experimental data is taken from Doherty *et al.* (1980).

Doherty *et al.* (1980) made simultaneous measurements of stress and birefringence for a vulcanized styrene-butadiene rubber (SBR) under uniaxial tension. The values of $N = 75$ and

$C^R = 0.3\text{MPa}$ according to our full network model for rubber elasticity are determined; the fit is shown in Fig. 3.7. The so-determined value of $N = 75$ is then used to predict birefringence according to our full network model for rubber photoelasticity. For that purpose, a value for the intrinsic birefringence $\Delta\mu_N$ must be estimated for a quantitative prediction. The simulated birefringence-stretch curve is presented in Fig. 3.8, where a value for the intrinsic birefringence $\Delta\mu_N = 3.6 \times 10^{-3}$ was chosen to give the best correlation with the experimental data. The value of $\Delta\mu_N$ seems to be reasonable (see e.g. Treloar, 1975). It is observed that the full network model for rubber photoelasticity is able to capture the optical behaviour, at least qualitatively.

3.5. DISCUSSION AND CONCLUSION

In this chapter, the full network model for rubber elasticity has been re-formulated in a more efficient and more micromechanics motivated manner. The equations are mathematically equivalent to those given in Wu and Van der Giessen (1993a). But, the new representation of the model allows us to avoid calculating principal stretches and principal stretch directions of deformations. The predicted numerical results have been compared with experimental data for a vulcanized rubber under uniaxial tension and pure shear. The comparison further supports our conclusion (Wu and van der Giessen, 1993a): the full network model for rubber elasticity does pick up the dependence of the state of deformation observed experimentally in rubber materials.

We have developed a so-called full network model for rubber photoelasticity. The derivation of this optical theory follows similar lines as the treatment of the full network model for rubber elasticity. The essential modification is the introduction of directional polarizabilities into the individual links of the idealized randomly-jointed chain. Our full network optical theory has extended Treloar and Rinding's (1979b) analysis for biaxial extension with fixed principal stretch directions to general three-dimensional deformation processes. We have also presented a so-called eight-chain network optical theory and have considered the classical three-chain network optical theory. The three-chain model and eight-chain model are both based on approximate descriptions of an affine network model, while our full network theory is based on an exact treatment of that same concept. The purpose of studying the full network model for rubber photoelasticity here in some detail is to assess the accuracy of the three-chain and eight-chain model. The general tendency of the predictions of these simplified models compared with the more exact full network theory is that with the same network parameters, the three-chain model overestimates the optical anisotropy of the network at large strains, while the eight-chain model underestimates the optical anisotropy. At small strains the models are indistinguishable.

In general, the form of the relations between polarizabilities and applied strains is very similar to that for the corresponding stresses. However, the specific non-Gaussian features are quantitatively less pronounced. This is due to the fact that whereas the tensile stress σ_c on a single chain tends to infinity as its stretch λ_c approaches the limit stretch $\sqrt{N}$, the polarizability of the chain remains finite throughout. As a result, the amount of computation required to achieve any degree of accuracy is notably less for the optical than for the mechanical problem. It is noted that the relative differences between various network models in predicted optical properties are smaller than in predicted mechanical properties at large strains, using the same value of N. Furthermore, the factor 0.62 was used in the approximation of the full network model in the description of optical properties [see (3.26) and (3.27)], while the factor 0.85 in the description of mechanical properties gave the best correlation with the full network model (see Wu and Van der Giessen, 1993a). From numerical point of view this also has to be attributed, to some extent, the fact that the specific non-Gaussian features are quantitatively less pronounced in the optical behaviour of rubbers.

The predicted numerical results according to the full network optical theory have been compared with experimental data for a vulcanized styrene-butadiene rubber under uniaxial tension. Although a value for the intrinsic birefringence $\Delta\mu_N$ was estimated, the full network optical theory was found to be able to capture the optical behaviour of rubbers, at least qualitatively. A quantitative comparison needs more experimental data for different types of deformation and materials. However, experiments for optical properties are much less available than for mechanical properties of rubbers. Furthermore, theoretical and experimental studies on optical properties presented in the literature have been limited to 1-D or 2-D deformations with fixed principal stretch directions in space, as far as the authors aware. Analysis of optical anisotropy in deformations including arbitrary rotations of the principal strain axes is of theoretical and practical importance. Obviously, large simple shear is a typical large strain and large rotation problem. The present study of optical anisotropies under simple shear has shown that the full network as well as the three-chain network and eight-chain network optical theories correctly predict that the molecular chains rotate continuously towards the shear direction. A more important aspect seems to be that the prediction of the secondary optical anisotropy, $\beta_{22} - \beta_{33}$, during simple shear is strongly dependent on the constitutive models. Thus, the simple shear test seems to provide a simple yet effective means for assessing the adequacy of non-Gaussian network models for rubber photoelasticity.

Finally, it is well-known that if the number of links N is large, the orientation distributions of the individual links with respect to the end-to-end vector has been given by Kuhn and Grun (1942) analytically. Furthermore, a closed-form solution for molecular chain orientation distribution function (CODF) has also been derived by Wu and Van der Giessen (1993a). Therefore, it is possible to obtain analytically a so-called Link Orientation Distribution Function (LODF), which would be expected to contain the complete information of the orientation distribution of molecular links at any stage of the deformation.

This paper is mainly concerned with the formulation of network optical theories and their constitutive differences. Further refinement of the models and detailed comparisons with experimental data are in progress and will be reported elsewhere.

Chapter 4

On Large-Strain Inelastic Torsion of Glassy Polymers

Abstract—Large-strain elastic-viscoplastic torsion of circular tubes and solid bars of glassy polymers is investigated under fixed-end as well as free-end conditions. The analysis employs a large inelastic deformation model for glassy polymers that incorporates a recently proposed constitutive law for the so-called orientational hardening, which is identified to play a key role in the description of the deformation-induced anisotropy in glassy polymers. The solution of the problem is obtained numerically by means of simple, special purpose finite elements. Results are presented in terms of predicted torque vs twist curves for all cases. Furthermore, we present axial force vs twist curves for fixed-end torsion or elongation vs twist curves for free-end torsion, both phenomena being associated with anisotropic hardening. In some cases, the predicted stress distributions are also given. The differences between free-end and fixed-end torsion are emphasized. Numerical results predicted by the model are compared with experimental results for polycarbonate found in the literature.

4.1. INTRODUCTION

Torsion of a circular bar in the range of large plastic strains has recently been the subject of numerous investigations. One of the main reasons for that is that the torsion test provides an excellent means for obtaining experimental data for the constitutive behaviour of elastic-plastic solids at large to very large deformations. The major advantage over the standard tensile test is that deformations of a solid bar in torsion remain axially homogeneous up to final failure without giving rise to strain localization phenomena such as necking and shear banding. Evidently, torsional deformations are inhomogeneous in the radial direction, but this multiaxiality is lower and better tractable than the three-dimensional state inside necks, etc. This has been shown before for large strain torsion of metals in [see e.g. Neale and Shrivastava, 1985, 1990; Wu and Van der Giessen, 1991a; Van der Giessen *et al.*, 1992a, 1992b] by means of a numerical method, and will be demonstrated here for glassy polymers.

Although torsion of a circular bar may appear to be a simple deformation process, the so-called Swift effect of notable axial extensions during large strain torsion of a metal bar with axially free ends—studied first by Swift (1947) is a fascinating and complex phenomenon. At room temperature, most initially isotropic metals tend to elongate during torsion when the specimen's ends are axially free [see also Bailey *et. al.*, 1972; Billington, 1977]. An analogous effect is the development of an axial force when the ends of the bar are axially fixed. It has been firmly established that these axial effects at large plastic strains in polycrystalline metals are due to the development of texture [e.g. Gil-Sevillano *et al.*, 1975; Harren *et al.* 1989]. Now, the constitutive modelling of the macroscopic behaviour of elastic-plastic solids where proper account is given of the induced anisotropy associated with texture development is currently considered one of the most challenging areas in continuum plasticity theory and has attracted a great deal of interest recently. It has been shown that the predictions of the axial effects show a remarkably strong dependence on the constitutive relations adopted [see e.g. Neale and Shrivastava, 1990; Van der Giessen *et al.*, 1992a; Harren *et al.* 1989]. Thus, the torsion test seems to provide a simple yet effective means for assessing the adequacy of such constitutive models.

It has been found that the axial extension effect is more pronounced in thin-walled tubes than in solid bars (Billington, 1977). In fact, many experimentalists have preferred torsion experiments on tubes over solid bars [see e.g. White *et al.*, 1990]. Reducing the wall thickness of a tube will reduce the nonuniformity of the deformation, and if the tubes are extremely thin then the deformation can be approximated to be homogeneous so that the experimental results can be easily interpreted. In fact, many experimental procedures based on torsion have used thin-walled specimens for which the state of the deformation has been assumed to be completely uniform and, for fixed- end torsion, to be a state of simple shear [see e.g. White *et al.*, 1990]. Unfortunately, in order to avoid buckling in a finite deformation torsion experiment on a hollow tube, it is necessary that the thickness of the tube be at least 10-15% of the mean radius (Khen and Rubin, 1992). Therefore, these hollow tubes cannot really be considered to be thin and the deformation is not really homogeneous. In addition to this, a thin hollow tube is much more difficult to be manufactured and gripped than a solid bar, so that in view of various experimental problems, thin-walled tubes seem to be of less practical importance at large strains. Consequently, the numerical simulation of both solid bars and (thick-walled) tubes under large strain torsion, accounting accurately for nonuniform states of deformation is of considerable practical significance.

It is expected that axial phenomena occur also in large strain torsion of glassy polymers [see e.g. Wu and Turner, 1973]. The first finite element simulation of large strain torsion of glassy polymers was developed very recently by authors (Wu and Van der Giessen, 1993b). In that preliminary study, we have considered the solid bar torsion of polycarbonate (PC) based on a constitutive framework developed by Boyce, Parks and Argon (1988). Their constitutive model incorporates rate and temperature dependent plastic flow, softening and subsequent orientational hardening, which are generally considered as a key phenomena. We have compared the predictions of the axial effects for three different orientation hardening models namely the three-chain model (Wang and Guth, 1952), the eight-chain model (Arruda and Boyce, 1991, 1993) and full network model (Wu and Van der Giessen, 1992a, 1993a). It was found that the predictions of the axial effects are sensitive to the orientation hardening relations adopted (Wu and Van der Giessen, 1993b).

In this chapter, a numerical analysis of combined torsion and tension of circular solid bars as well as tubes is presented, focusing on both fixed-end and free-end torsion as limiting cases. The approach is based on special purpose, ring- shaped finite elements. These elements are effectively one-dimensional and allow for an efficient analysis of such problems. Differences between the behaviour in free-end and in fixed-end torsion are emphasized. Furthermore, the differences in behaviour of solid bars and of tubes are discussed. Numerical results predicted by the model are compared with experimental results for thick-walled polycarbonate tubes found in (Wu and Turner, 1973).

Tensors will be denoted by bold-face letters. The tensor product is denoted by ⊗ and the following operations for second and fourth-order tensors apply ($\mathbf{a} = a_{ij}\mathbf{e}_i \otimes \mathbf{e}_j$, $\mathbf{b} = b_{ij}\mathbf{e}_i \otimes \mathbf{e}_j$, $\underset{\sim}{\mathcal{A}} = \mathcal{A}_{ijkl}\mathbf{e}_i \otimes \mathbf{e}_j \otimes \mathbf{e}_k \otimes \mathbf{e}_l$, $\mathbf{e}_i$ being a Cartesian basis): $\mathbf{ab} = a_{ik}b_{kj}\mathbf{e}_i \otimes \mathbf{e}_j$, $\mathbf{a} \cdot \mathbf{b} = a_{ij}b_{ij}$ and $\underset{\sim}{\mathcal{A}}\mathbf{b} = \mathcal{A}_{ijkl}b_{kl}$. Superscripts T and -1 denote the transverse and inverse of a second-order tensor, respectively. A superposed dot denotes the material time derivative or rate. Matrix or column matrix (vector) will be denoted by a large size letter in the finite element formulation.

4.2. CONSTITUTIVE EQUATIONS

We start by briefly recapitulating the model for large inelastic deformations of glassy polymers developed by Boyce, Parks and Argon (1988), which will be referred to henceforth as the BPA model. The BPA model is developed within an internal variable framework, but at the same time is to a large extent based on the micro- mechanics and orientation behaviour associated with the molecular chain network structure of polymers and its affine deformation characteristics. In the BPA model, the microstructure of an initially isotropic amorphous polymer is assumed to consist primarily of long molecular chains, which are randomly coiled in space. Side groups protrude from the backbone chains at various locations and, in conjunction with overall chain trajectory, can act as nodes, or points of physical entanglement. This results in a network-like structure much like that of rubber, but with the chemical crosslinks replaced by physical entanglements.

Following the pioneering work of Haward and Thackray (1968), it is assumed that a glassy polymer must overcome two physical distinct sources of resistance before large strain inelastic flow may occur. Below the glass transition temperature, prior to initial yield, the material must be stressed to exceed its intermolecular resistance to segment rotation. Once the material is free to flow, molecular alignment occurs, resulting in an anisotropic internal resistance to further inelastic deformation, which is called orientational hardening; this will be discussed in Sec. 4.2.2. The intermolecular resistance to plastic flow is considered to be due to the impedance imposed by neighbouring chains on the ability of a chain segment to rotate either individually or in a cluster. Based upon the assumption that plastic flow occurs by double-kinking of molecular chains, Argon (1973) developed the following expression for the plastic shear strain rate, $\dot{\gamma}^p$:

$$\dot{\gamma}^p = \dot{\gamma}_0 \exp\left[-\frac{As_0}{T}\left(1 - \left(\frac{\tau}{s_0}\right)^{5/6}\right)\right] \tag{4.1}$$

where $\dot{\gamma}_0$ is a pre-exponential factor, A is proportional to the activation volume/Boltzmann's constant, T is the absolute temperature and τ is the applied shear stress. Furthermore, $s_0 = 0.077\mu/(1-\nu)$ is the athermal shear strength, μ is the elastic shear modulus, υ is Poisson's ratio. Boyce *et al.* (1988) extended this expression to include the effects of pressure and strain softening. They used $s + \alpha p$ instead of s_0, where p is the pressure and α is a pressure dependence coefficient. Furthermore, s is assumed to evolve with plastic straining via

$\dot{s} = h(1 - s/s_{ss})\,\dot{\gamma}^p$, where h is the rate of resistance drop with respect to the plastic strain and s_{ss} is the assumed saturation value of s.

4.2.1. Three-dimensional representation

Consider the homogeneous deformation of an initially isotropic body loaded so that its deformation gradient at a subsequent time is **F**. The deformation gradient may be multiplicatively decomposed into elastic and plastic parts, $\mathbf{F} = \mathbf{F}^e\mathbf{F}^p$. Following Lee (1969) and others, Boyce *et al.* (1988) take $\mathbf{F}^e$ to be symmetric, so that $\mathbf{F}^p$ represents the relaxed configuration obtained by unloading without rotation (in the polar decomposition sense). Hence, $\mathbf{F}^p$ can be decomposed as $\mathbf{F}^p = \mathbf{V}^p\mathbf{R}$ with the plastic stretch $\mathbf{V}^p$ and the total stretch $\mathbf{V}$ in polar decomposition $\mathbf{F} = \mathbf{V}\mathbf{R}$ being related by $\mathbf{V} = \mathbf{F}^e\mathbf{V}^p$. According to this decomposition, the velocity gradient is decomposed as:

$$\mathbf{L} = \dot{\mathbf{F}}\mathbf{F}^{-1} = \mathbf{D} + \mathbf{W} = \dot{\mathbf{F}}^e\mathbf{F}^{e^{-1}} + \mathbf{F}^e\mathbf{L}^p\mathbf{F}^{e^{-1}}$$

where **D** is the rate of deformation, **W** is the spin, and $\mathbf{L}^p = \mathbf{D}^p + \mathbf{W}^p = \dot{\mathbf{F}}^p\mathbf{F}^{p^{-1}}$ is the velocity gradient in the relaxed configuration. With the adopted symmetry of $\mathbf{F}^e$, the skewsymmetric part $\mathbf{W}^p$ is algebraically given as **W** plus a term dependent on $\mathbf{F}^e$ and $\mathbf{D} + \mathbf{D}^p$ (see Boyce *et al.*, 1988). Since the elastic strains will remain small, we can neglect geometry differences between current and relaxed configurations, $\mathbf{F}^e \approx \mathbf{I}$. When this approximation is carried through consistently, the constitutive equations can be simplified significantly, as discussed by Boyce *et al.*, (1988). In particular it is noted that $\mathbf{W}^p \approx \mathbf{W}$ and $\mathbf{D} \approx \mathbf{D}^e + \mathbf{D}^p$, with $\mathbf{D}^e$ the symmetric part of $\dot{\mathbf{F}}^e\mathbf{F}^{e^{-1}}$.

The rate of change of shape of the relaxed configuration, $\mathbf{D}^p$, must be constitutively prescribed. In the BPA model, the magnitude of $\mathbf{D}^p$ is taken to be given by the plastic shear strain rate, $\dot{\gamma}^p$, according to (4.1) while the tensor direction of $\mathbf{D}^p$ is specified by **N**, so that

$$\mathbf{D}^p = \dot{\gamma}^p\mathbf{N}, \tag{4.2}$$

where the direction **N** is the deviatoric part of the driving stress, normalized by the effective equivalent shear stress τ:

$$\mathbf{N} = \frac{1}{\sqrt{2}\tau}\tilde{\boldsymbol{\sigma}}', \qquad \tau = \sqrt{\frac{1}{2}\tilde{\boldsymbol{\sigma}}'\cdot\tilde{\boldsymbol{\sigma}}'} \tag{4.3}$$

The driving stress $\tilde{\boldsymbol{\sigma}}$ is itself defined by

$$\tilde{\boldsymbol{\sigma}} = \boldsymbol{\sigma} - \mathbf{B} \tag{4.4}$$

where $\boldsymbol{\sigma}$ is the Cauchy stress tensor and **B** is the back stress tensor due to the strain hardening resulting from molecular alignment as will be further discussed in the next section.

In (Boyce *et al.*, 1988), the Cauchy stress is taken to be given by the elastic constitutive law (Anand, 1979)

$$\boldsymbol{\sigma} = \frac{1}{J}(\underset{\sim}{\mathcal{L}}_\mathrm{e} \ln \mathbf{F}^\mathrm{e}) \tag{4.5}$$

where $\underset{\sim}{\mathcal{L}}_\mathrm{e}$ is the fourth-order isotropic elastic modulus tensor:

$$\underset{\sim}{\mathcal{L}}_\mathrm{e} = \mathcal{L}_\mathrm{e}^{ijkl}\mathbf{e}_i \otimes \mathbf{e}_j \otimes \mathbf{e}_k \otimes \mathbf{e}_l,$$

$$\mathcal{L}_\mathrm{e}^{ijkl} = \frac{E}{2(1+\nu)}\left[(\delta^{ik}\delta^{jl} + \delta^{il}\delta^{jk}) + \frac{2\nu}{1-2\nu}\delta^{ij}\delta^{kl}\right], \tag{4.6}$$

with $E = 2(1+\nu)\mu$ being Young's modulus and $J = \det\mathbf{F}^\mathrm{e}$. Although a *different* implementation is briefly mentioned in (Boyce *et al.*, 1988) to solve boundary value problems, we here wish to adopt a more typical viscoplastic rate formulation as will be discussed in detail in the next section. As a consequence, we need the rate form equivalent of the elasticity equations (4.5)-(4.6). Since the elastic strains are assumed to remain small, we may replace the hyperelastic law (4.5) with the hypoelastic rate form:

$$\overset{\nabla}{\boldsymbol{\sigma}} = \underset{\sim}{\mathcal{L}}_\mathrm{e}\mathbf{D}^\mathrm{e} \tag{4.7}$$

in terms of the same modulus tensor $\underset{\sim}{\mathcal{L}}_\mathrm{e}$ and employing the Jaumann stress rate, $\overset{\nabla}{\boldsymbol{\sigma}} = \dot{\boldsymbol{\sigma}} - \mathbf{W}\boldsymbol{\sigma} + \boldsymbol{\sigma}\mathbf{W}$ to retain objectivity. The constitutive equations (4.7) can be finally arranged in the following form:

$$\overset{\nabla}{\boldsymbol{\sigma}} = \underset{\sim}{\mathcal{L}}_\mathrm{e}\mathbf{D} - \dot{\boldsymbol{\sigma}}_\mathrm{v} \tag{4.8}$$

where $\dot{\boldsymbol{\sigma}}_\mathrm{v} = \underset{\sim}{\mathcal{L}}_\mathrm{e}\mathbf{D}^\mathrm{p}$ acts as an instantaneous stress rate term that represents the viscoplastic contribution.

4.2.2. Orientation hardening

Once the material is stressed to the point of overcoming intermolecular barriers to chain motion, the molecular chains will tend to align along the direction of principal plastic stretch [see e.g. Haward and Thackray (1968) and Argon (1973)]. This action decreases the configurational entropy of the system which, in turn, creates an internal network stress. This process of network distortion is very similar to that of rubber network, and Haward and Thackray (1968) suggested to describe this for uniaxial extension by means of a back stress determined through a Langevin spring, as suggested by non-Gaussian network theory. Boyce *et al.* (1988) extended this approach to general three-dimensional plastic deformations by introducing a back stress tensor **B** which is taken to be coaxial with the plastic left stretch tensor $\mathbf{V}^\mathrm{p}$. Thus, if $\mathbf{e}_i^\mathrm{p}$ are the unit eigen vectors of $\mathbf{V}^\mathrm{p}$, corresponding to a plastic stretch λ_i^p, the back stress **B** is constructed as

$$\mathbf{B} = \sum_i B_i(\mathbf{e}_i^\mathrm{p} \otimes \mathbf{e}_i^\mathrm{p})$$

from the principal components B_i. Originally, Boyce *et al.* (1988) adopted the classical so-called three-chain model for which the principal components $B_i^{3-\mathrm{ch}}$ of the back stress tensor are given in terms of the plastic stretches λ_i^{p} by (Wang and Guth, 1952)

$$B_i^{3\text{-ch}} = \frac{1}{3} C^{\mathrm{R}} \sqrt{N} \left[\lambda_i^{\mathrm{p}} \mathcal{L}^{-1}\left(\frac{\lambda_i^{\mathrm{p}}}{\sqrt{N}}\right) - \frac{1}{3} \sum_{j=1}^{3} \lambda_j^{\mathrm{p}} \mathcal{L}^{-1}\left(\frac{\lambda_j^{\mathrm{p}}}{\sqrt{N}}\right) \right]. \tag{4.9}$$

Here, C^{R} is known as the rubbery modulus, N is a statistical network parameter related to the network locking stretch and $\mathcal{L}$ is the Langevin function defined by $\mathcal{L}(\beta) = \coth\beta - 1/\beta$.

However, very recently Arruda and Boyce (1991, 1993b) found that the three-chain non-Gaussian network model was not capable of picking up the strain hardening observed experimentally in polycarbonate (PC) and polymethylmetacrylate (PMMA). At the same time, they suggested to model the network by eight equivalent chains instead of three, and obtained more close agreement with their experimental results for PC and PMMA. The principal components of the back stress tensor according to this eight-chain non-Gaussian network model are:

$$B_i^{8\text{-ch}} = \frac{1}{3} C^{\mathrm{R}} \sqrt{N} \mathcal{L}^{-1}\left(\frac{\lambda^{\mathrm{p}}}{\sqrt{N}}\right) \frac{{\lambda_i^{\mathrm{p}}}^2 - {\lambda^{\mathrm{p}}}^2}{\lambda^{\mathrm{p}}}, \qquad {\lambda^{\mathrm{p}}}^2 = \frac{1}{3} \sum_{j=1}^{3} {\lambda_j^{\mathrm{p}}}^2. \tag{4.10}$$

Both the three-chain and eight-chain model are based on approximate representations of the actual spatial distributions of molecular chains by “lumping” their orientations in three and eight specific directions, respectively. Very recently, the authors developed the so-called full network model in which full account is taken of the 3-D orientation distribution of the individual chains in the network (Wu and Van der Giessen, 1992a, 1993a). This model is a 3-D generalization for arbitrary deformation paths of the 2-D model for proportional deformations proposed by Treloar and Riding (1979a). The principal back stresses according to this model can be given in two equivalent ways, depending on whether one considers the chain orientation distribution in the undeformed isotropic state or in the current deformed state; here, we only reiterate the expression according to the first point of view because it is more convenient for applications, i.e.

$$B_i = \frac{1}{4\pi} C^{\mathrm{R}} \sqrt{N} \int_0^{\pi} \int_0^{2\pi} \mathcal{L}^{-1}\left(\frac{\lambda^{\mathrm{p}}}{\sqrt{N}}\right) \frac{{\lambda_i^{\mathrm{p}}}^2 {m_i^0}^2 - {\lambda^{\mathrm{p}}}^2/3}{\lambda^{\mathrm{p}}} \sin\theta_0 d\theta_0 d\varphi_0, \quad {\lambda^{\mathrm{p}}}^2 = \sum_{j=1}^{3} {\lambda_j^{\mathrm{p}}}^2 {m_j^0}^2 \tag{4.11}$$

Here, the m_i^0 are the components of the unit vector $\mathbf{m}^0$ in orientation space (θ_0, φ_0) defined by:

$$m_1^0 = \sin\theta_0 \cos\varphi_0, \qquad m_2^0 = \sin\theta_0 \sin\varphi_0, \qquad m_3^0 = \cos\theta_0,$$

where θ_0 and φ_0 measure the orientation of molecular chains relative to the principal stretch directions in the undeformed configuration. Furthermore, an accurate approximation of the full network predictions according to (4.11) has been found (Wu and Van der Giessen, 1992a) in the form of a combination of the three-chain and eight-chain model predictions (4.9), (4.10) through

$$B_i = (1 - \rho^{\mathrm{p}}) B_i^{3\text{-ch}} + \rho^{\mathrm{p}} B_i^{8\text{-ch}}. \tag{4.12}$$

Excellent agreement with full integration is obtained by taking ρ^{p} to be related to the maximum principal plastic stretch $\lambda^{\mathrm{p}}_{\max} = \max(\lambda^{\mathrm{p}}_1, \lambda^{\mathrm{p}}_2, \lambda^{\mathrm{p}}_3)$ via $\rho^{\mathrm{p}} = 0.85\lambda^{\mathrm{p}}_{\max}/\sqrt{N}$. All computations to be reported here have used the expression (4.12).

4.3. PROBLEM FORMULATION AND METHOD OF SOLUTION

We consider a uniform circular cylindrical tube of initial outer radius $R_{\mathrm{o}0}$, initial inner radius $R_{\mathrm{i}0}$, and initial length L_0, which is subjected to a twist φ due to an applied torque M. Also, the bar may be subjected simultaneously to an axial force F associated with an axial displacement U. The end faces of the bar are constrained such that they remain plane and perpendicular to the axial direction, and it is assumed that in fact any cross-section of the bar remains plane. The lateral surfaces of the bar are traction-free and all properties are assumed to be axisymmetric and homogeneous along the axial direction. Although deformation-induced anisotropy may occur, the behaviour remains axisymmetric and is further assumed to remain uniform in the axial direction. Thus, we neglect the formation and propagation of macroscopic circumferential shear bands that may develop [see, e.g. Wu and Turner, 1973; Wang *et al.*, 1982]. Consequently, the bar remains circular cylindrical, and at the current deformed state has an outer radius R_{o}, an inner radius R_{i}, and a length L. This problem and the adopted numerical method are a natural extension of the solid bar problem studied in (Wu and Van der Giessen, 1991a; Van der Giessen *et al.*, 1992a, 1992b) within the context of metal plasticity. In the sequel we give a brief but complete summary of the governing equations.

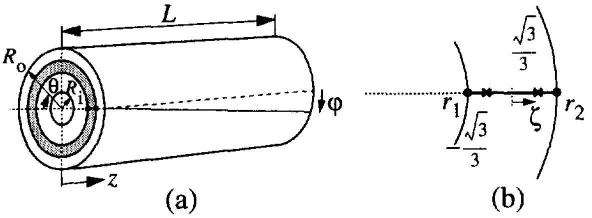

Fig. 4.1. The finite element used here are cylindrical tubes with inner radius r_1 and outer radius r_2; (a) definition of nodal points (●); and (b) material sampling points (X).

All governing equations will be referred to a spatially fixed cylindrical coordinate system $x^i = (r, \theta, z)$ with orthonormal base vectors $\mathbf{e}_i$. These base vectors are associated with the current state, so that the various tensor components to be used in the sequel represent the respective physical components. However, due account must be given of the fact that the base vectors are spatially fixed so that their material time derivative will generally not vanish since the coordinate system is curvilinear (Van der Giessen, 1991a).

The kinematics of the problem is readily established. The deformations are such that if the initial coordinates of a material point are $x^i_0 = (r_0, \theta_0, z_0)$, its current coordinates are $x^i = (r, \theta, z)$, where

$$r = r(r_0;t)\ , \quad \theta = \theta_0 + \omega(t)z_0\ , \quad z = e(t)z_0, \tag{4.13}$$

with t a monotonic time-like parameter. Here, $\omega = \varphi/L_0$ is the twist per unit initial length of the bar and $e = L/L_0 = 1 + U/L_0$ is the extensional stretch in axial direction. The components of the velocity vector $v = v_i e_i$ are then given by

$$(v_i) = (\dot{r}, \frac{z\dot{\omega}}{e}, \frac{z\dot{e}}{e}) ,$$

and the components of $D = D_{ij} e_i \otimes e_j$ and $W = W_{ij} e_i \otimes e_j$ are found to be given by:

$$D_{11} = \frac{\partial \dot{r}}{\partial r}, \quad D_{22} = \frac{\dot{r}}{r}, \quad D_{33} = \frac{\dot{e}}{e}, \quad D_{23} = \frac{1}{2}\frac{r\dot{\omega}}{e}, \quad D_{12} = D_{13} = 0 ;$$

$$W_{12} = -\frac{z\dot{\omega}}{e}, \quad W_{13} = 0, \quad W_{23} = \frac{1}{2}\frac{r\dot{\omega}}{e} . \tag{4.14}$$

Regarding the stress state inside the bar, axisymmetry and axial homogeneity imply that the stress components of Cauchy stress $\sigma = \sigma_{ij} e_i \otimes e_j$ satisfy $\sigma_{12} = \sigma_{13} = 0$ while $\sigma_{ij} = \sigma_{ij}(r;t)$ otherwise. The resultant torque, M, and the axial tensile force, F, are given by

$$M = 2\pi \int_{R_i}^{R_o} r^2 \sigma_{23} dr , \quad F = 2\pi \int_{R_i}^{R_o} r \sigma_{33} dr . \tag{4.15}$$

while the lateral surfaces are traction-free, $\sigma_{11}(R_i) = 0$ and $\sigma_{11}(R_o) = 0$. Free-end torsion is analyzed by specifying the boundary condition $F = 0$, while fixed-end torsion follows from the condition $\dot{e} = 0$.

It is observed that for the present axisymmetric problem, the pertinent quantities depend only on the radial coordinate r. This problem can be dealt with in an efficient way by means of special purpose finite elements in the radial direction as demonstrated in (Wu and Van der Giessen, 1991a). As shown schematically in Fig. 4.1a, the elements used are circular cylindrical tubes, with inner radius r_1 and outer radius r_2 in the current configuration. Such an element is geometrically one-dimensional along the r-axis, with two nodes at $r = r_1$ and $r = r_2$, respectively (see Fig. 4.1b). In addition to the overall axial displacement U and the angle of twist φ, the degrees of freedom of the element are the radial nodal displacments. It is numerically convenient to take the element's vector **V** of degrees of freedom as

$$\mathbf{V} = \begin{bmatrix} \frac{\dot{r}_1}{r_1} & \frac{\dot{r}_2}{r_2} & \frac{\dot{\omega}}{e}L & \frac{\dot{e}}{e} \end{bmatrix}^T \tag{4.16}$$

in terms of the radial nodal velocities $\dot{r}_1$ and $\dot{r}_2$. The radial velocity at any radius within the element is determined by assuming a linear interpolation of $\dot{r}/r$ between the nodal values. The element's force vector **F** dual to **V**, such that $\mathbf{F}^T\mathbf{V}$ is the rate of work of the loads on the element, is then given by

$$\mathbf{F} = \begin{bmatrix} r_1 F_{r1} & r_2 F_{r2} & M^l & LF^l \end{bmatrix}^T \tag{4.17}$$

where F_{r1} and F_{r2} are the radial forces on the inner and outer surfaces of the element, respectively, and where M^l and F^l are the torque and the axial force, respectively, that act on the element. The total torque M and the total axial force F acting on the bar are obtained by summation over all elements:

$$M = \sum M^i, \quad F = \sum F^i.$$

The governing FE equations are formulated within a framework using the concept of material sampling points and this leads to the element equilibrium equations of the form

$$\mathbf{D}^T \mathbf{\Sigma} = \mathbf{F} \tag{4.18}$$

where $\mathbf{\Sigma}$ is a vector containing the sampling point stress components and $\mathbf{D}$ is a matrix depending on the current geometry (see Appendix). Since the lateral surfaces of the bar are traction-free, not only all internal nodal radial forces F_{ri} must vanish, but also the radial force at the outmost node at $r = R_o$ and at the innermost node $r = R_i$. The rate equilibrium conditions at the current instant are obtained by straightforward time differentiation. After elimination of the stress rates by means of the constitutive equations (4.8), the following finite element equations for the unknown $\mathbf{V}$ are obtained:

$$\mathbf{K}\mathbf{V} = \dot{\mathbf{F}} + \dot{\mathbf{F}}_v$$

(see Appendix). Here, $\dot{\mathbf{F}}_v$ acts as an additional force rate that represents the viscous terms and is calculated from $\boldsymbol{\sigma}_v$ appearing in (4.8).

The deformation process is then analysed employing a linear incremental solution procedure, based on a time step Δt, with simultaneous updating of the configuration. At each increment, the twisting increment $\Delta\omega = \dot{\omega}\Delta t$ and the stretching increment $\Delta e = \dot{e}\Delta t$ as well as the nodal radial displacement increments are obtained from the equations

$$\mathbf{K}(\Delta t \mathbf{V}) = \Delta t(\dot{\mathbf{F}} + \dot{\mathbf{F}}_v) - (\mathbf{D}^T \mathbf{\Sigma} - \mathbf{F}), \tag{4.19}$$

assembled for the entire bar. The equilibrium conditions (4.18) are included in the right hand side in order to prevent drifting of the solution away from the true equilibrium path. Finally, the increments of the sampling point stresses are evaluated by $\Delta\boldsymbol{\sigma} = \dot{\boldsymbol{\sigma}}\Delta t$ and similarly for the other pertinent quantities, except for the back stress **B** which can be computed from the current plastic state of deformation instantaneously.

4.4. RESULTS

The torsion problem described in Sec. 4.3 involves a number of nondimensional groups, and therefore we introduce the following quantities:

$$\Gamma = \varphi \frac{R_{o0}}{L_0}, \quad \bar{\tau} = \frac{3M}{2\pi (R_{o0}^3 - R_{i0}^3) s_0}, \quad \bar{\sigma} = \frac{F}{\pi (R_{o0}^2 - R_{i0}^2) s_0}. \tag{4.20}$$

These quantities, along with the overall axial logarithmic strain $\varepsilon = \ln e$ can be used to efficiently present the overall response of the specimen irrespective of its exact geometry. To enable a direct comparison with experimental data for PC (Wu and Turner, 1973) we have taken the actual dimensions to be the same as in (Wu and Turner, 1973), i.e. $R_{o0} = 3.175$ mm and $L_0 = 6.35$, while the initial inner radius is $R_{i0} = 1.5875$ mm for the tube. All numerical calculations were carried out at a constant twist rate $\dot{\omega} = 0.02 \mathrm{rad\,s}^{-1}$ corresponding to a shear rate $\dot{\Gamma} = 0.01 \mathrm{s}^{-1}$.

At room temperature ($T = 294$ K), the following values of the parameters that determine the stress-rate, temperature dependence and softening behaviour for PC are used: $\dot{\gamma}_0 = 2 \times 10^{15} \mathrm{s}^{-1}$, $A = 240 \mathrm{K/MPa}$, $s_0 = 111$ MPa, $s_{ss}/s_0 = 0.92$, $h = 500 \mathrm{MPa}$ and $\alpha = 0.08$, while Young's modulus and Poisson's ratio are taken as $E = 2623$ MPa and $\nu = 0.3$, respectively. Most of this data has been taken from the experiment carried out by Boyce and Arruda (1990); but, the value of the shear strength has been fitted with the yield point observed in the torsion experiments (Wu and Turner, 1973), while the saturation value s_{ss} has been chosen to fit the softening behaviour observed during simple shear of PC by G'Sell (1986). The parameters C^R and N that govern the orientation hardening are taken as $C^R = 3.7 \mathrm{MPa}$ and $N \approx 6$, which are reasonable compared with experimental values [see Reference 27 in (G'Sell, 1986)]. Admittedly, the material parameters have been compiled from different sources involving different experiments on material that is likely to be not exactly the same, but because of lack of sufficient experimental data this was the best we could do. In any case, with the exception of the yield point, the torsion results to be presented here provide an independent comparison with the experiments in (Wu and Turner, 1973).

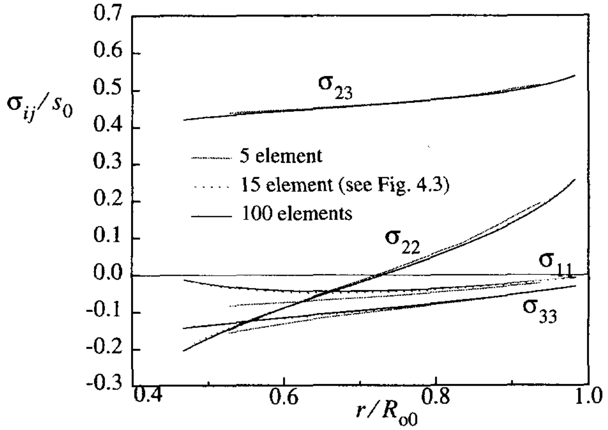

Fig. 4.2. Stress distributions inside the tube in fixed-end torsion for $\Gamma = 2$ using different meshes (note the reduction of the radii of the tube; see also Fig. 4.5).

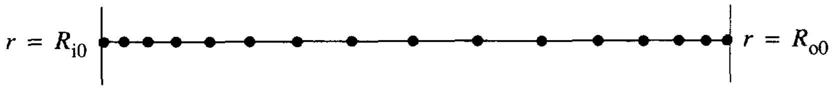

Fig. 4.3. The finite element mesh used for the tube, comprising 15 elements.

In Wu and Van der Giessen (1991a), the predicted stress distributions for an incompressible elastic solid bar in fixed-end torsion were compared with the analytical solution available when the torsion angle is small. Even with only five elements the stress distribution was represented with sufficient accuracy. Further checks were performed for an incompressible elasto-plastic material by comparison with highly accurate results from a semi-analytical method, and again it was found that sufficiently accurate results were obtained by using only five elements (Van der Giessen *et al.*, 1992a). However, for a tube one cannot expect to get highly accurate results using only five elements, because of the intrinsic properties of the special element and the additional lateral inner boundary condition $\sigma_{11}(R_i) = 0$ involved. In order to obtain sufficiently accurate results, we use a somewhat refined mesh near the lateral surfaces (especially near the inner surface) where high strain gradients are expected. Numerical experiments show for a tube that the computed torque and axial force as well as the shear stress distributions are not sensitive to the number of elements; but, the second order effects, such as the radial stress distribution, are indeed rather sensitive to the number of elements used. Figure 4.2 shows a typical stress distribution for a twist corresponding to $\Gamma = 2$, using three different meshes consisting of 5 equally sized elements, 100 elements or 15 elements with a local refinement as shown in Fig. 4.3 (the stress distributions are plotted by linear interpolation between sampling point values). Clearly, the differences in predicted shear stress are very small, but the radial stress distribution near the inner radius with a uniform mesh comprising only 5 elements is very poor. Since this paper primarily focuses on the overall characteristics of torsion (torque, axial force, elongation, etc.) which are not very sensitive to deviations from the actual stress state, it was decided that the mesh shown in Fig. 4.3 for the tube would be sufficiently accurate. A similar mesh is used for the solid bar.

4.4.1. Fixed-end torsion

We first study the fixed-end torsion of PC specimens. This corresponds to invoking the axial boundary conditions $\dot{e} = \dot{U} = 0$ in and will lead to the development of an axial force F.

Figure 4.4 shows the torque responses to fixed-end torsion of the tube and of the solid bar in terms of the torque M and the twist φ. Later on, in Fig. 4.7, the torque responses are plotted in terms of the nondimensional torque $\bar{\tau}$ and the shear strain Γ defined in (4.20). It is found that the overall trends obtained for the torque in fixed-end torsion is similar to the evolution of the shear stress in simple shear as studied e.g. in (Wu and Van der Giessen, 1993a). The response is characterized by *i)* an initially elastic response which ends at the yield point when the torsion angle φ is about 0.3 rad ($\Gamma \approx 0.15$); *ii)* a small but significant torque drop after plastic deformation has been initiated, which at the current levels of strain must be attributed to the material softening; *iii)* a gradual hardening starting around $\varphi \approx 2$ rad ($\Gamma \approx 1$) and which ends when the maximum plastic stretch at the outer radius approaches the locking stretch $\sqrt{N}$ of the macromolecular chain network. Also shown are a number of experimental points taken from Wu and Turner (1973). It is found that the constitutive model, together with the numerical tool used here, is capable of capturing a number of the major characteristics of the plastic torsion behaviour in a qualitatively reasonable way. The small strain viscoelastic effect observed in the experiments, as indicated by the deviation from the linear elastic response prior to yield, is not accounted for in the constitutive model.

Although axial loads were not monitored during their experiments, Wu and Turner (1973) stated that no axial force is expected during twisting of a tube made from an isotropic material if it does not undergo a volume change; if the material tends to change its volume an axial force may develop. Before presenting the axial loads found in our simulations, we first consider the volume changes predicted here. Figure 4.5 presents the evolution of the outer radius R_0 and inner radius R_i during torsion of the tube. It is clear that both R_0 and R_i decrease monotonically while the length of the specimen is kept fixed. It is also found from Fig. 4.5 that the thickness of the tube slowly increases. At the maximum twist, $\Gamma = 2.2$, the wall thickness has changed by about 4%, corresponding to a reduction in volume of the tube of only about 0.2%. It is emphasized that according to the constitutive model of Sec. 4.2, this volume reduction is entirely due to elastic deformations.

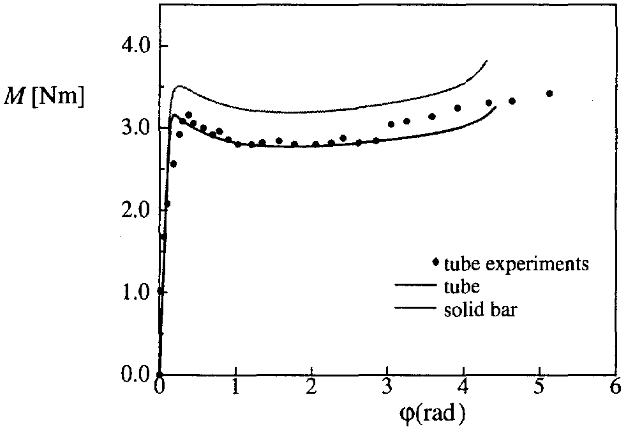

Fig. 4.4. Torque responses in fixed-end torsion for the solid bar ($R_i = 0$) and for the tube ($R_{i0}/R_{o0} = 0.5$). The experimental data for the tube are taken from Wu and Turner (1973).

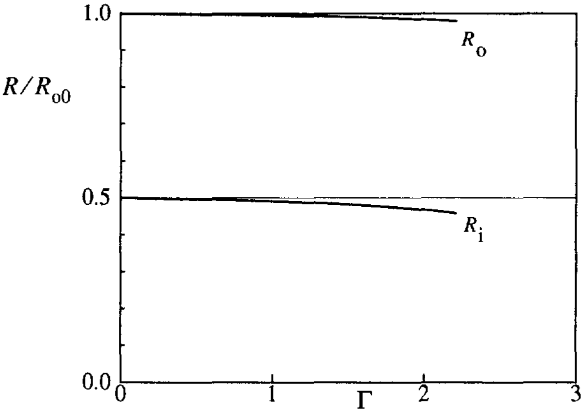

Fig. 4.5. Evolution of the outer radius R_o and the inner radius R_i during fixed-end torsion.

The predicted axial forces for the tube and for the solid bar are presented in Fig. 4.6. It is found that in terms of the dimensionless force $\bar{\sigma}$, the tube and the solid bar exhibit a similar axial response. The prime characteristic of the response is that the axial force developed during twisting is compressive. There appears to be a rapid initiation during the first elastic stage of the deformation, followed by a stage of little change after yielding and softening, while the axial force increases rapidly again during the strain-hardening stage. The value of the axial force attained prior to yielding is consistent with the dilatation of 0.2% mentioned above. In the model used here, volume changes are attributed to elastic deformations only, and with a value of the bulk modulus of $B = E/[3(1-2\nu)] = 2186$ MPa, the compressive axial load agrees with that shown in Fig. 4.6. Obviously, this argument cannot explain the subsequent three-fold increase with ongoing plastic deformation. The latter phenomenon must be attributed to the deformation-induced anisotropy associated with the deformation of the entangled molecular network in glassy polymers.

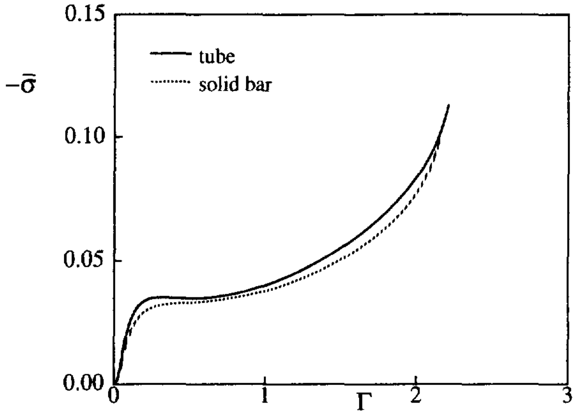

Fig. 4.6. Development of compressive axial forces in fixed-end torsion.

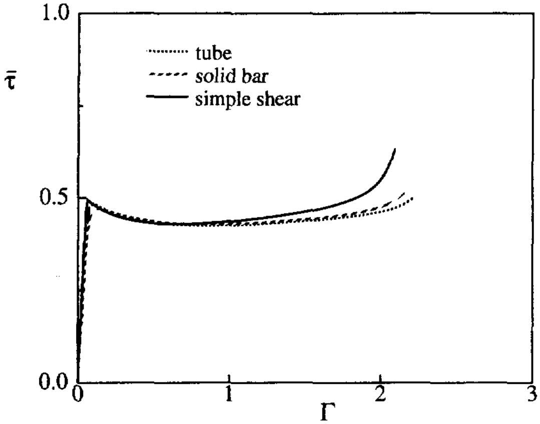

Fig. 4.7. Normalized torque responses to fixed-end torsion in comparison with the shear stress responses to homogeneous simple shear.

As has been demonstrated in Fig. 4.2, the stress distributions in tube or solid bar are quite nonuniform. For practical purposes, it may be of interest however to have an approximate tool to link the twisting of a tube or solid bar to homogeneous simple shear. If the shear stress distribution is approximated to be constant across the entire cross-section, this shear stress is readily found to be related to the applied torque M through the quantity $\bar{\tau}s_0$ defined in (4.20). To assess the accuracy of this approximation, we replot in Fig. 4.7 the torque responses found for tube and solid bar in comparison with the shear stress response to homogeneous simple shear to a shear strain Γ obtained by direct straightforward integration of the constitutive equations [see Wu and Van der Giessen, 1993a]. It is seen that the simple representation in terms of $\bar{\tau}$ gives a reasonable estimate of the simple shear behaviour up to moderately large strains of the order of 1, but that at larger strains the stress inhomogeneity in the actual specimen become too large to give an adequate agreement.

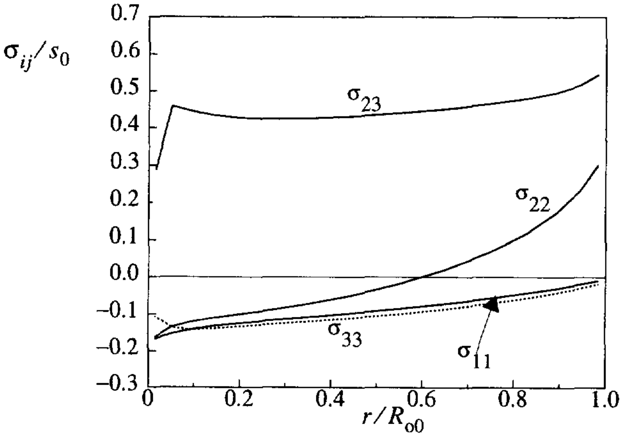

Fig. 4.8. Stress distributions in the solid bar in fixed-end torsion at $\Gamma = 2$.

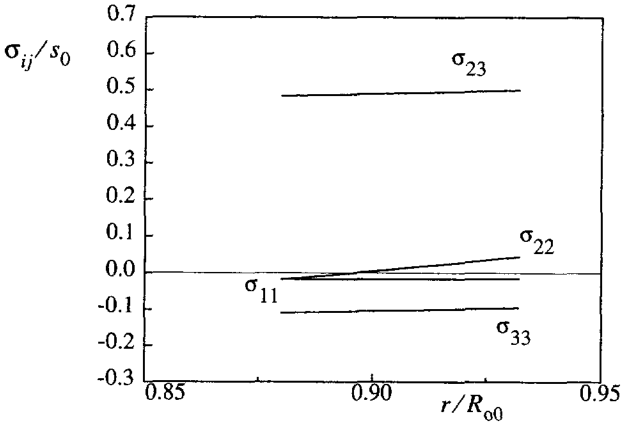

Fig. 4.9. Stress distribution in a thin-walled tube ($R_{i0}/R_{o0} = 19/20$) in fixed-end torsion at $\Gamma = 2$.

To assess the difference between the behaviour of the tube and the solid bar, we present the stress distributions across the solid bar when $\Gamma = 2$ in Fig. 4.8. Comparing with the results for the tube shown in Fig. 4.2, the shear stress in the tube is much more uniform than in the solid bar. The reason is that in the solid bar the material close to the axis of the bar remains in small deformation state up to the moment that the maximum plastic stretch at the outer surface approaches the limit stretch of the network.

Reducing the wall thickness of a tube, will reduce the nonuniformity of the deformation. In fact, many experimental procedures based on torsion have used thin- walled specimens for which the state of deformation has been assumed to be completely uniform and, for fixed-end torsion, to be a state of simple shear [see, e.g., White *et al.*, 1990]. In order to check this hypothesis, we present the stress distributions in such a tube with $R_{i0} = 19/20\,R_{00}$ in fixed-end torsion in Fig. 4.9. It is observed that the shear stress, the axial normal stress and radical normal stress are indeed uniform across the wall thickness with fair accuracy, but the hoop stress still exhibits a significant variation.

4.4.2. Free-end torsion

We proceed by studying the torsion of the same tube and the same solid bar as in the previous subsection, but under conditions of axially free ends. These conditions are obtained by imposing the opposite axial boundary condition as in the previous case of fixed-end torsion, i.e. $F = 0$ in (4.16), thus allowing for an axial elongation e.

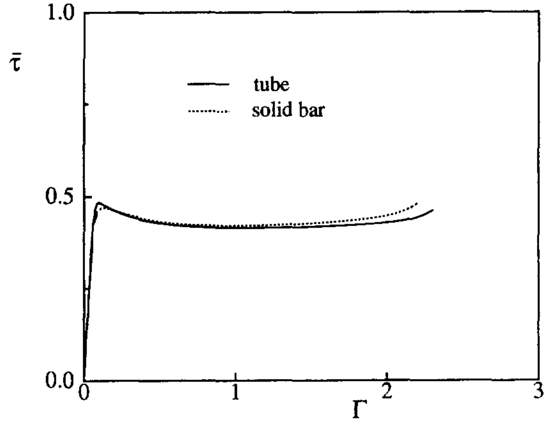

Fig. 4.10. Torque responses in free-end torsion for the solid bar and for the tube $(R_{i0}/R_{00} = 0.5)$.

Figures 4.10 and 11 present the torque responses and the accompanying axial elongation development in the tube and in the solid bar during free-end torsion. The difference between the tube and the solid bar in predicted torque is similar to that in fixed-end torsion. The torque responses found during free-end torsion differ rather little from those found in fixed-end torsion (Fig. 4.4); careful inspection shows that the free-end tests exhibit less strain hardening at the final stages of deformation.

Figure 4.11 shows that the axial strains that develop during free-end twisting may attain quite significant values of up to 6%. The axial strain is found to increase almost linearly up to $\Gamma \approx 1$ while growing increasingly fast for larger twists. Figure 4.11 also shows a significant difference in elongation between the tubular and the solid specimen. Furthermore, it is interesting to note that the axial strain develops in a distinctly different manner than the axial forces during fixed-end torsion (Fig. 4.6), and does not display a long-range plateau of very small apparent slope. Nevertheless, both second-order effects are attributed to the same feature of the material's response, namely deformation-induced anisotropy.

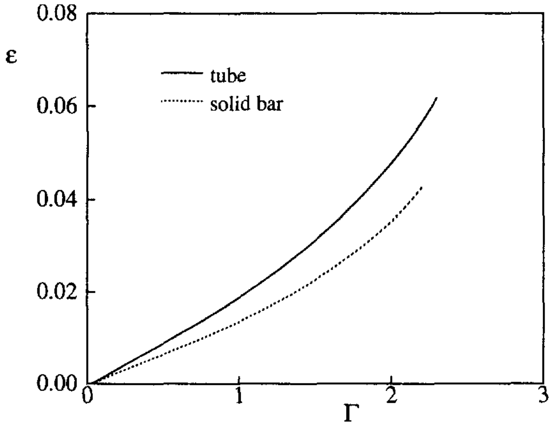

Fig. 4.11. Axial elongations in free-end torsion of tube or solid bar.

Wang *et al.* (1982) give some experimental results for free-end torsion of solid specimens made of various types of polymers, including a PC. Their torque response is qualitatively similar to that shown in Fig. 4.10, be it the maximum shear strain attained in their experiments was only about 0.4, i.e. well in the softening regime. The particular type of PC used in those experiments is rather different from that assumed in the computations: the value of s_0 estimated from the torque at yield is only about 90 MPa. Data for elongation and volume changes are only given in (Wang *et al.*, 1982) up to yield, and thus represent only the elastic behaviour.

The predicted stress distributions across the tube are shown in Fig. 4.12.

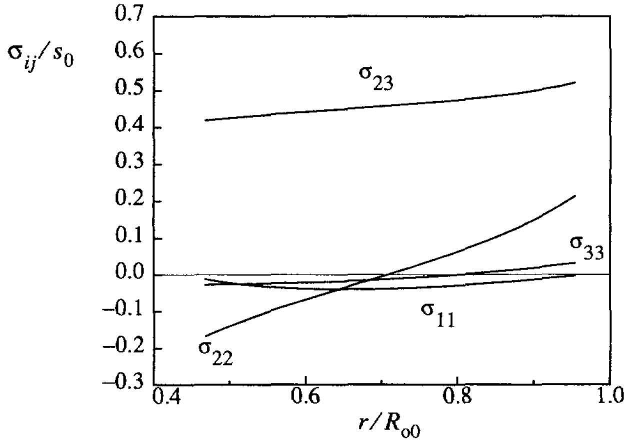

Fig. 4.12. Stress distributions in the tube in free-end torsion at $\Gamma = 2$.

4.5. CONCLUSION

In this chapter, we have analysed the large strain elastic-viscoplastic torsion of circular cylindrical tubes and solid bars under fixed-end as well as free-end conditions using a numerical method based on a simple, special purpose finite elements.

The predicted response of a tube under fixed-end torsion has been compared with available experimental data for polycarbonate, based on material properties taken (with one exception) from independent sources. The calculation stopped at $\Gamma = 2.2$. when the maximum plastic stretch approached the locking stretch of the macromolecular chain network. Generally speaking, the agreement is reasonable, even though our simulations cannot reflect the initiation and propagation of macroscopic shear bands observed experimentally. Preliminary numerical studies of shear band propagation in simple shear with the same constitutive model (Wu and Van der Giessen, 1992b) seem to support the approximation involved: the results suggest that the torque response during propagation is affected only slightly, while the response after propagation has completed is identical to that when the deformation is presumed to remain uniform during the entire process. A number of features in the experimental results are not picked up by the constitutive model. We shall return to this later.

As expected, stress distributions in a tube are more homogeneous than in a solid bar (see Fig. 4.2 and Fig. 4.8). For the tube considered here, the variations through the thickness of the tube are small for the shear stress but can be large for the other stress components. It has been verified that if the tubes are very thin, then the deformation can be approximated as being homogeneous with fair accuracy and experimental results for torsion can be easily interpreted; but, such a specimen is known to be unstable at large strains (torsional buckling is a primary mode of failure for such a specimen). On the other hand, the numerical method developed here is capable of simulating large strain torsion of tubes with any values of R_{i0} $(0 \le R_{i0}/R_{o0} < 1)$. Furthermore, it is fairly easy to incorporate other viscoplastic constitutive models into this special finite element program. Therefore, it provides a useful tool to interpret experimental torsion results on thick-walled tubes or solid specimens, and thus to determine the material parameters appearing in the constitutive models.

The axial force in fixed-end torsion and the axial elongation in free-end torsion are mainly due to the development and the subsequent rotation of the induced anisotropy. For the amorphous polymers considered here, this anisotropy is associated with the stretching of the entangled molecular chain structure. It is well-known that the prediction of such second-order phenomena generally shows a rather strong dependence on the constitutive models—in particular the description of anisotropic hardening. For large strain torsion of a solid bar of polycarbonate, this has been studied by Wu and Van der Giessen (1993b) by considering in addition to the full network model, the simplified three- and eight-chain model. It is observed that all three orientation hardening models discussed in Sec. 4.2 give virtually identical axial force predictions up to $\Gamma \approx 1$ (Wu and Van der Giessen, 1993b). For large twists, the three-chain model predicts very large compressive axial forces, but when using the eight-chain model, the magnitude of the axial force reduces drastically. The predicted axial force by the full network model is in between that predicted by the three-chain model and eight-chain model, respectively. Similar phenomena have been observed for the predicted axial elongations during free-end torsion. Unfortunately, we have not been able to find any experimental data on axial force or elongation development during torsion of PC in order to compare these predicted results with experiments [Wang *et al.* (1982) only gives such data prior to yield].

One of the most important differences between simulated and experimental response to fixed-end torsion is that our simulations tend to overestimate the strain hardening at large plastic strains. This is intimately connected with the affine network theory used here to model orientational hardening. As discussed in some detail by Wu and Van der Giessen (1993a), the idea of using an affine network theory to model the stretching of the molecular network assumes that the junction points in the network remain in tact. However, it has been suggested in the literature [see e.g. Raha and Bowden, 1972; Botto *et al.*, 1987] that physical entanglements in amorphous polymers are being pulled out during deformation. In terms of our network model this would mean that the number of chains n reduces in the course of the deformation process, while the number of links N per chain increases, thus reducing the stiffness of the network.

Furthermore, especially the axial effects predicted here may depend sensitively on the particular way of incorporating deformation-induced anisotropy by means of the effective stress concept in (4.3). This is likely to be rather important in the above torsional problem, where the stress history is non-proportional and significant rotations of the principal axes occur. A totally different approach to modelling orientational hardening has been adopted by Batterman and Bassani (1990). All these constitutive aspects require further study. The formulation of improved models and their implications for large strain torsion are in progress and will be reported elsewhere.

Chapter 5

Analysis of Shear Band Propagation in Amorphous Glassy Polymers

Abstract—Similar to the well-known neck propagation phenomenon, shearing of polymer materials often reveals the initiation and subsequent propagation of a shear band. Finite element analysis is used to numerically simulate large plane strain, simple shear tests, focussing attention on the initiation and propagation of the shear band. The mesh sensitivity and effects of initial imperfection, strain softening, orientation hardening, strain-rate as well as the edge effects are discussed in detail. It appears that the intrinsic softening is the driving force to promote initiation of the shear band and its propagation in the shear direction, while the orientation hardening is the driving force for widening of the shear band. The predicted numerical results are compared with experimental data for polycarbonate found in the literature.

5.1. INTRODUCTION

Localization instabilities in the form of shear bands appear to be almost inevitable when a ductile solid undergoes large plastic flow. Such plastic instabilities have a dual significance; as a precursor to fracture and as a mechanism for further deformation. Developing the ability to predict their onset, evolution and subsequent failure is essential for the control of a variety of manufacturing processes and for the design of material microstructures.

The shear localization phenomenon has been widely studied since the early 1970's, primarily for metals [the proceedings edited by Zbib *et al.* (1992) gives a state-of-the-art overview]. It is well-known that localization of plastic flow is strongly directionally sensitive and, therefore, is severely influenced by the evolution of hardening anisotropy that develops with large plastic strains (Rice, 1977). Examples of anisotropic hardening include slip system hardening in metallic single crystals , and the strain-induced molecular orientational hardening that occurs during the drawing of polymers. Commonly, anisotropic hardening has a first-order effect on predictions of localization when compared to an isotropic analysis. More precise and quantitative predictions of localization therefore require improved descriptions of evolving anisotropy.

Although advances in the understanding of plastic instabilities appear to come primarily from researches on polycrystalline metals and soils, a number of characteristic aspects of localization instabilities in polymers begins to be assessed [see e.g. Bowden (1973) and G'Sell (1986)]. It is now widely acknowledged that glassy polymers exhibit plastic deformation below the glass transition temperature mainly through the activation of microscopic shear bands. Macroscopic strain localization in polymers can be very different from that in metals due to the dramatic stiffening of polymers at large strains, which is associated with molecular chains orienting and stretching during the deformation process. While plastic instabilities like necks or shear bands in metals almost invariably tend to localize progressively until failure intervenes, necks and macroscopic shear bands in polymers typically do not continue to localize but tend to propagate along the specimen [see e.g. G'Sell *et al.* (1983), Neale and Tugcu (1985), and Buisson and Ravi-Chandar (1990)]. The propagation of localized deformation is fundamental to the processing of polymers since the permanently oriented state generally has enhanced properties, but can also affect subsequent failure. However, the quantitative understanding of thermal-viscoplastic localizations in polymers is still in its infancy. In part, this is due to the fact that appropriate constitutive equations have been developed only fairly recently. In this study, we focus on a particular type of macroscopic shear localization in amorphous glassy polymers.

Experiments carried out by G'Sell and co-workers have shown that shear band propagation may indeed occur during simple shear of an amorphous polymer such as polycarbonate (e.g. G'Sell and Gopez, 1985). In those experiments, special specimens were used which were designed to create a uniform state of plane simple shear in the gauge section. However it was found that due to some inhomogeneity in the material, a highly localized shear band appeared near the center of the specimen, which subsequently grew and widened in the direction perpendicular to the shear direction. Grenet and G'Sell (1990) also performed an approximate analysis, using a 1-D constitutive model proposed by G'Sell and Jonas (1979), by means of a simple finite difference method. As a first approximation, they took into account only the shear component of the strain tensor. Recently, Arruda and Boyce (1992) presented a fully three-dimensional finite element analysis of the test in order to address the effects of edge distortion and material drawn in from the grip sections. Although the predicted nominal shear stress-strain curve was found to accurately capture the observed test data, their analysis did not show the formation of a shear band in the center of the specimen.

In this chapter, we first briefly recapitulate the Boyce *et al.* (1988) 3-D constitutive model of large inelastic deformations of amorphous glassy polymers. The yield of initially isotropic glassy polymers has been found to depend on pressure, strain rate, and temperature. After yielding, glassy polymers often strain soften and subsequently strain harden. Adopting a constitutive framework with internal variables, the molecular chain network structure of polymers and its affine deformation attributes particular features to the constitutive formulation. A full network model of rubber elasticity (Wu and Van der Giessen, 1992a, 1993a), which is capable of capturing the deformation dependence of hardening, is used to develop a tensorial internal state variable model of evolving anisotropic polymer response. This fully 3-D constitutive model has been found to be able to predict many aspects of the large plastic strain behaviour of glassy polymers observed experimently (Wu and Van der Giessen, 1993a, 1993b, 1993c). In a recent study, a finite element simulation of shear band propagation in glassy polymers was carried out (Wu and Van der Giessen, 1992b). In that preliminary study, we considered the simple shear of a polycarbonate specimen of infinite length in the shear direction, based on the fully

3-D constitutive model. Although the problem we solved (Wu and Van der Giessen, 1992b) was effectively a one-dimensional problem across the width of the slab, the results showed that the shear band propagation phenomenon could be, at least qualitatively, captured by the type of constitutive models available at the present moment. However, edge effects could not be taken into account in such a 1-D simulation. Based on detailed experimental observations, G'Sell (1986) suggested that a plane strain type 2-D simulation should be able to reproduce the main features of the experiment. In the present chapter, the constitutive model is incorporated in finite element computations of the plane simple shear test, focusing attention on the initiation and propagation of the shear band. Numerical results predicted by the model are compared with experimental results for polycarbonate found in the literature.

Tensors will be denoted by bold-face letters. The tensor product is denoted by $\otimes$ and the following operations for second and fourth-order tensors apply ($\mathbf{a} = a_{ij}\mathbf{e}_i \otimes \mathbf{e}_j$, $\mathbf{b} = b_{ij}\mathbf{e}_i \otimes \mathbf{e}_j$, $\underset{\sim}{\mathcal{A}} = \mathcal{A}_{ijkl}\mathbf{e}_i \otimes \mathbf{e}_j \otimes \mathbf{e}_k \otimes \mathbf{e}_l$, $\mathbf{e}_i$ being a Cartesian basis): $\mathbf{ab} = a_{ik}b_{kj}\mathbf{e}_i \otimes \mathbf{e}_j$ and $\underset{\sim}{\mathcal{A}}\mathbf{b} = \mathcal{A}_{ijkl}b_{kl}$. Superscripts T and -1 denote the transverse and inverse of a second-order tensor, respectively. The trace is denoted by tr, and a superposed dot denotes the material time derivative or rate.

5.2. CONSTITUTIVE EQUATIONS

The yield of initially isotropic glassy polymers has been found to depend on pressure, strain rate, and temperature. After yielding, glassy polymers often strain soften and subsequently strain harden. Here, we briefly recapitulate the model for large inelastic deformations of glassy polymers developed by Boyce, Parks and Argon (1988), which will be referred to henceforth as the BPA model. The BPA model is developed within an internal variable framework, but at the same time is to a certain extent based on the micromechanical considerations of the molecular chain network structure of polymers. In the BPA model, the microstructure of an initially isotropic amorphous polymer is assumed to consist primarily of long molecular chains, which are randomly coiled in space. Side groups protrude from the backbone chains at various locations and, in conjunction with overall chain trajectory, can act as nodes, or points of physical entanglement. This results in a network-like structure much like that of rubber, but with the chemical crosslinks replaced by physical entanglements.

Following the pioneering work of Haward and Thackray (1968), it is assumed that a glassy polymer must overcome two physical distinct sources of resistance before large strain inelastic flow may occur. Below the glass transition temperature, prior to initial yield, the material must be stressed to exceed its intermolecular resistance to segment rotation; this will be discussed in Sec. 5.2.1. Once the material is free to flow, molecular alignment occurs, resulting in an anisotropic internal resistance to further inelastic deformation, which is called orientational hardening; this will be discussed in Sec. 5.2.2.

5.2.1. Intermolecular resistance

The intermolecular resistance to plastic flow is considered to be due to the impedance imposed by neighbouring chains on the ability of a chain segment to rotate either individually or in a cluster. Based upon the assumption that plastic flow under an applied shear stress τ occurs by double-kinking of molecular chains, Argon (1973) developed the following expression for the resulting plastic shear strain rate $\dot{\gamma}^{\mathrm{p}}$:

$$\dot{\gamma}^{\mathrm{p}} = \dot{\gamma}_0 \exp\left[-\frac{As_0}{T}\left(1 - \left(\frac{\tau}{s_0}\right)^{5/6}\right)\right]. \tag{5.1}$$

Here, $\dot{\gamma}_0$ is a pre-exponential factor, A is a material parameter that is proportional to the activation volume/Boltzmann's constant, T is the absolute temperature and s_0 is the athermal shear strength, which in Argon's model is given by $s_0 = 0.077\mu/(1-\nu)$ in terms of the elastic shear modulus μ and Poisson's ratio ν. Boyce *et al.* (1988) extended this expression to include the effect of pressure and strain softening. They used $s + \alpha p$ instead of s_0, where p is the pressure and α is a pressure dependence coefficient. Furthermore, s is assumed to evolve with plastic straining via

$$\dot{s} = h(1 - s/s_{\mathrm{ss}})\,\dot{\gamma}^{\mathrm{p}} \tag{5.2}$$

where h is the rate of resistance drop with respect to the plastic strain and s_{ss} is the assumed saturation value of s. The incorporation of this expression (5.1) into a 3-D constitutive model for rate-dependent plastic flow was also proposed by Boyce *et al.* (1988); for completeness, we give a brief recapitulation in Sec. 5.2.3.

5.2.2. Anisotropic internal resistance

Once the material is stressed to the point of overcoming intermolecular barriers to chain motion, the molecular chains will tend to align along the direction of principal plastic stretch [see e.g. Haward and Thackray (1968) and Argon (1973)]. This action decreases the configurational entropy of the system which, in turn, creates an internal network stress. This process of network distortion is very similar to that of rubber network, and Haward and Thackray (1968) suggested to describe this for uniaxial extension by means of a back stress determined through a Langevin spring, as suggested by non-Gaussian network theory. Boyce *et al.* (1988) extended this approach to general three-dimensional plastic deformations by introducing a back stress tensor $\mathbf{B}$ which is taken to be coaxial with the plastic left stretch tensor $\mathbf{V}^{\mathrm{p}}$ (the precise definition of $\mathbf{V}^{\mathrm{p}}$ will be given in Sec. 5.2.3. Thus, if $\mathbf{e}_i^{\mathrm{p}}$ are the unit eigen vectors of $\mathbf{V}^{\mathrm{p}}$, corresponding to a plastic stretch λ_i^{p}, the back stress $\mathbf{B}$ is constructed as

$$\mathbf{B} = \sum_i B_i(\mathbf{e}_i^{\mathrm{p}} \otimes \mathbf{e}_i^{\mathrm{p}}) \tag{5.3}$$

from the principal components B_i. Originally, Boyce *et al.* (1988) adopted the classical so-called three-chain model for which the principal components $B_i^{3-\mathrm{ch}}$ of the back stress tensor are given in terms of the plastic stretches λ_i^{p} by (Wang and Guth, 1952)

$$B_i^{3\text{-ch}} = \frac{1}{3} C^{\mathrm{R}} \sqrt{N} \left[\lambda_i^{\mathrm{p}} \mathcal{L}^{-1}\left(\frac{\lambda_i^{\mathrm{p}}}{\sqrt{N}}\right) - \frac{1}{3} \sum_{j=1}^{3} \lambda_j^{\mathrm{p}} \mathcal{L}^{-1}\left(\frac{\lambda_j^{\mathrm{p}}}{\sqrt{N}}\right) \right] \text{ (no sum over } i\text{)}, \tag{5.4}$$

where C^{R} is known as the rubbery modulus, N is a statistical network parameter related to the network locking stretch and $\mathcal{L}$ is the Langevin function defined by $\mathcal{L}(\beta) = \coth\beta - 1/\beta$.

More recently however, Arruda and Boyce (1991, 1993b) found that the three-chain non-Gaussian network model was not capable of picking up the strain hardening observed experimentally in polycarbonate (PC) and polymethylmetacrylate (PMMA). At the same time, they suggested to model the network by eight equivalent chains instead of three, and obtained more close agreement with their experimental results for PC and PMMA. The principal components of the back stress tensor according to this eight-chain non-Gaussian network model are given by

$$B_i^{8\text{-ch}} = \frac{1}{3} C^{\mathrm{R}} \sqrt{N} \mathcal{L}^{-1}\left(\frac{\lambda^{\mathrm{p}}}{\sqrt{N}}\right) \frac{\lambda_i^{\mathrm{p}^2} - \lambda^{\mathrm{p}^2}}{\lambda^{\mathrm{p}}} \text{ (no sum over } i\text{)}, \tag{5.5}$$

where λ^{p} is defined through

$$\lambda^{\mathrm{p}^2} = \frac{1}{3} \sum_{j=1}^{3} \lambda_j^{\mathrm{p}^2}.$$

Both the three-chain and eight-chain model are based on approximate representations of the actual spatial distributions of molecular chains by "lumping" their orientations in three and eight specific directions, respectively. Very recently, the authors developed the so-called full network model in which full account is taken of the 3-D orientation distribution of the individual chains in the network (Wu and Van der Giessen, 1992a, 1993a). This model is a 3-D generalization for arbitrary deformation paths of the 2-D model for proportional deformations proposed by Treloar and Riding (1979a). The principal back stresses according to this model can be given in two equivalent ways, depending on whether one considers the chain orientation distribution in the undeformed isotropic state or in the current deformed state; here, we only reiterate the expression according to the first point of view because it is more convenient for applications, i.e.

$$B_i = \frac{1}{4\pi} C^{\mathrm{R}} \sqrt{N} \int_0^{\pi} \int_0^{2\pi} \mathcal{L}^{-1}\left(\frac{\lambda^{\mathrm{p}}}{\sqrt{N}}\right) \frac{\lambda_i^{\mathrm{p}^2} m_i^{0^2} - \lambda^{\mathrm{p}^2}/3}{\lambda^{\mathrm{p}}} \sin\theta_0 d\theta_0 d\varphi_0 \text{ (no sum over } i\text{)}. \tag{5.6}$$

Here, λ^{p} is defined by

$$\lambda^{\mathrm{p}^2} = \sum_{j=1}^{3} \lambda_j^{\mathrm{p}^2} m_j^{0^2}$$

and m_i^0 are the unit vector components in orientation space defined by

$$m_1^0 = \sin\theta_0\cos\varphi_0\ , \qquad m_2^0 = \sin\theta_0\sin\varphi_0\ , \qquad m_3^0 = \cos\theta_0\ ,$$

in terms of the angles θ_0 and φ_0 which measure the orientation of molecular chains relative to the principal stretch directions in the undeformed configuration. The numerical evaluation of the integral in (5.6) is rather time-consuming, but an accurate approximation of the full network predictions according to (5.6) has been found (Wu and Van der Giessen, 1992a) in the form of a combination of the three-chain and eight-chain model predictions (5.4), (5.5) through

$$B_i = (1-\rho^{\mathrm{p}})B_i^{3\text{-ch}} + \rho^{\mathrm{p}} B_i^{8\text{-ch}}. \tag{5.7}$$

Excellent agreement with full integration is obtained by taking ρ^{p} to be related to the maximum principal plastic stretch $\lambda^{\mathrm{p}}_{\max} = \max(\lambda^{\mathrm{p}}_1, \lambda^{\mathrm{p}}_2, \lambda^{\mathrm{p}}_3)$ via $\rho^{\mathrm{p}} = 0.85\lambda^{\mathrm{p}}_{\max}/\sqrt{N}$. All computations to be reported here have used the expression (5.7).

5.2.3. Three-dimensional representation

Boyce *et al.* (1988) developed the 3-D constitutive relations on the basis of the multiplicative decomposition of the deformation gradient $\mathbf{F}$ into elastic and plastic parts, $\mathbf{F} = \mathbf{F}^{\mathrm{e}}\mathbf{F}^{\mathrm{p}}$. Following Lee (1969) and others, the elastic part $\mathbf{F}^{\mathrm{e}}$ is taken to be symmetric, so that $\mathbf{F}^{\mathrm{p}}$ represents the relaxed configuration obtained by unloading without rotation (in the polar decomposition sense). Hence, $\mathbf{F}^{\mathrm{p}}$ can be decomposed as $\mathbf{F}^{\mathrm{p}} = \mathbf{V}^{\mathrm{p}}\mathbf{R}$ with the plastic stretch $\mathbf{V}^{\mathrm{p}}$ and the total stretch $\mathbf{V}$ in polar decomposition $\mathbf{F} = \mathbf{V}\mathbf{R}$ being related by $\mathbf{V} = \mathbf{F}^{\mathrm{e}}\mathbf{V}^{\mathrm{p}}$. According to this decomposition, the velocity gradient $\mathbf{L}$ is decomposed as

$$\mathbf{L} = \dot{\mathbf{F}}\mathbf{F}^{-1} = \mathbf{D}+\mathbf{W} = \dot{\mathbf{F}}^{\mathrm{e}}\mathbf{F}^{\mathrm{e}^{-1}} + \mathbf{F}^{\mathrm{e}}\mathbf{L}^{\mathrm{p}}\mathbf{F}^{\mathrm{e}^{-1}}$$

where $\mathbf{D}$ is the rate of deformation, $\mathbf{W}$ is the spin, and $\mathbf{L}^{\mathrm{p}} = \mathbf{D}^{\mathrm{p}} + \mathbf{W}^{\mathrm{p}} = \dot{\mathbf{F}}^{\mathrm{p}}\mathbf{F}^{\mathrm{p}^{-1}}$ is the velocity gradient in the relaxed configuration. With the adopted symmetry of $\mathbf{F}^{\mathrm{e}}$, the skewsymmetric part $\mathbf{W}^{\mathrm{p}}$ is algebraically given as $\mathbf{W}$ plus a term dependent on $\mathbf{F}^{\mathrm{e}}$ and $\mathbf{D}+\mathbf{D}^{\mathrm{p}}$ (see Boyce *et al.*, 1988). Since the elastic strains will remain small, we can neglect geometry differences between current and relaxed configurations, $\mathbf{F}^{\mathrm{e}} \approx \mathbf{I}$. When this approximation is carried through consistently, the constitutive equations can be simplified significantly, as discussed by Boyce *et al.* (1988). In particular it is noted that in this case $\mathbf{W}^{\mathrm{p}} \approx \mathbf{W}$ and $\mathbf{D} \approx \mathbf{D}^{\mathrm{e}} + \mathbf{D}^{\mathrm{p}}$, with $\mathbf{D}^{\mathrm{e}}$ the symmetric part of $\dot{\mathbf{F}}^{\mathrm{e}}\mathbf{F}^{\mathrm{e}^{-1}}$.

The rate of change of shape of the relaxed configuration, $\mathbf{D}^{\mathrm{p}}$, must be constitutively prescribed. In the BPA model, the magnitude of $\mathbf{D}^{\mathrm{p}}$ is taken to be given by the plastic shear strain rate, $\dot{\gamma}^{\mathrm{p}}$, according to (5.1) while the tensor direction of $\mathbf{D}^{\mathrm{p}}$ is specified by $\mathbf{N}$, so that

$$\mathbf{D}^{\mathrm{p}} = \dot{\gamma}^{\mathrm{p}}\mathbf{N}, \tag{5.8}$$

where the direction $\mathbf{N}$ is the deviatoric part of the driving stress, normalized by the effective equivalent shear stress τ:

$$\mathbf{N} = \frac{1}{\sqrt{2}\tau}\tilde{\boldsymbol{\sigma}}'$$

$$\tau = \sqrt{\frac{1}{2}\tilde{\boldsymbol{\sigma}}' \cdot \tilde{\boldsymbol{\sigma}}'} \tag{5.9}$$

Based on the suggestion by Haward and Thackray (1968), the driving stress $\tilde{\boldsymbol{\sigma}}$ itself is defined by

$$\tilde{\boldsymbol{\sigma}} = \boldsymbol{\sigma} - \mathbf{B} \tag{5.10}$$

where $\boldsymbol{\sigma}$ is the Cauchy stress tensor and $\mathbf{B}$ is the back stress tensor, according to (5.3) and (5.6)–(5.7), due to the strain hardening resulting from molecular alignment, as discussed in Sec. 5.2.2. Consistent with the approximation $\mathbf{F}^e \approx \mathbf{I}$, the plastic principal stretches λ_i^p to be substituted into (5.4)–(5.6) are approximated by the principal values of $\mathbf{V} \approx \mathbf{V}^p$.

In Boyce *et al.* (1988), the Cauchy stress is taken to be given by the elastic constitutive law (Anand, 1979)

$$\boldsymbol{\sigma} = \frac{1}{J}(\underset{\sim}{\mathcal{L}}_e \ln \mathbf{F}^e) \tag{5.11}$$

where $\underset{\sim}{\mathcal{L}}_e$ is the fourth-order isotropic elastic modulus tensor:

$$\underset{\sim}{\mathcal{L}}_e = \mathcal{L}_e^{ijkl}\mathbf{e}_i \otimes \mathbf{e}_j \otimes \mathbf{e}_k \otimes \mathbf{e}_l,$$

$$\mathcal{L}_e^{ijkl} = \frac{E}{2(1+\nu)}\left[(\delta^{ik}\delta^{jl} + \delta^{il}\delta^{jk}) + \frac{2\nu}{1-2\nu}\delta^{ij}\delta^{kl}\right], \tag{5.12}$$

with $E = 2(1+\nu)\mu$ being Young's modulus and $J = \det \mathbf{F}^e$. On the basis of these relations, Boyce *et al.* (1988) briefly discuss a possible implementation for the solution of boundary value problems, we here wish to adopt a more typically viscoplastic rate formulation as will be discussed in detail in the Sec. 5.3. As a consequence, we need the equivalent rate form of the elasticity equations (5.11)–(5.12). Since the elastic strains are assumed to remain small, we may replace the hyperelastic law (5.11) with the hypoelastic rate form

$$\overset{\nabla}{\boldsymbol{\sigma}} = \underset{\sim}{\mathcal{L}}_e \mathbf{D}^e \tag{5.13}$$

in terms of the same modulus tensor $\underset{\sim}{\mathcal{L}}_e$ and employing the Jaumann stress rate, $\overset{\nabla}{\boldsymbol{\sigma}} = \dot{\boldsymbol{\sigma}} - \mathbf{W}\boldsymbol{\sigma} + \boldsymbol{\sigma}\mathbf{W}$ to retain objectivity. The constitutive equations (5.13) can be finally arranged in the following form:

$$\overset{\nabla}{\boldsymbol{\sigma}} = \underset{\sim}{\mathcal{L}}_e \mathbf{D} - \dot{\boldsymbol{\sigma}}_v \tag{5.14}$$

where $\dot{\boldsymbol{\sigma}}_v = \underset{\sim}{\mathcal{L}}_e \mathbf{D}^p$ acts as an instantaneous stress rate term that represents the viscoplastic contribution.

5.3. PROBLEM FORMULATION AND METHOD OF SOLUTION

The simple shear deformation of a parallelepiped solid of initial length $2B_0$ and width $2A_0$

can be basically defined, as illustrated in Fig. 5.1, by the homogeneous relative glide of parallel planes along the shear direction. The amount of shear is commonly expressed by the ratio $\Gamma = U/(2A_0)$, where U is the relative displacement of the opposite faces of the parallelepiped. In order to impose a constant shear rate $\dot{\Gamma} = \dot{U}/(2A_0)$, the opposite faces are displaced at a constant velocity $\dot{U} = \dot{\Gamma}(2A_0)$. Variations of the thickness during the deformation are relevant only to second order terms in the strain tensor and may be neglected to a first approximation (G'Sell, 1986); thus, this deformation mode is of a 2-D plane strain type. The conventional nominal shear stress and normal stress are defined by $F_s/(2B_0)$ and $F_n/(2B_0)$, respectively, where F_s and F_n are the applied shearing force and the force required to maintain the width of the specimen, respectively.

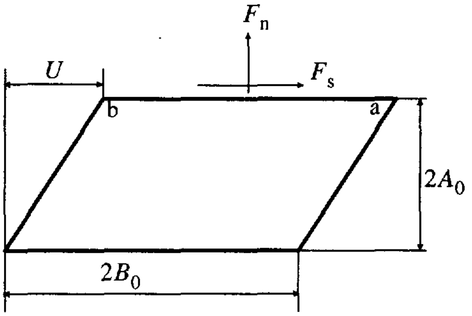

Fig. 5.1. Schematic definition of the specimen under the plane strain simple shear.

In the experiments carried out by Gopez (1983) and by G'Sell and Gopez (1985), specimens were used which were designed to create a uniform state of plane simple shear in the gauge section. However it was found that due to some inhomogeneity in the material, a highly localized shear band appeared near the center of the specimen, which subsequently grew and widened in the direction perpendicular to the shear direction. To trigger the initiation of such a macroscopic shear band at the center of the specimen in our 2-D analysis, we assume here an initial imperfection of the shear strength s_0 of the form

$$\Delta s_0 = \zeta s_0 \exp\left[-\frac{(x-B_0)^2 + (B_0/A_0)^2 (y-A_0)^2}{0.01\,(B_0^2 + A_0^2)}\right] \tag{5.15}$$

such that the initial shear strength is $s_0 - \Delta s_0$, where ζ determines the intensity.

A numerical analysis is performed by employing a finite element scheme in a manner similar to that described by Needleman and Tvergaard (1984). When the elastic-viscoplastic constitutive law (5.14) is employed, the time-dependent terms $\dot{\boldsymbol{\sigma}}_v$ affect only the nodal traction-rate vector. No contribution to the stiffness matrix arises from the variations of plastic deformation rate since these do not explicitly depend on stress rates. We use quadrilateral elements, each built up of four linear velocity, triangular subelements arranged in a 'crossed triangle' configuration. An equilibrium correction procedure is employed to avoid drifting away from the true equilibrium path during the incremental procedure. Integrations with respect to time are computed using an explicit Euler integration method. Since the elements of the stiffness matrix are of the order of the elastic moduli, as given by (5.12), very small time steps have to be employed to achieve satisfactory convergence in the early stages of viscoplastic flow; however, at later stages of well-developed viscoplastic flow, much large steps may be used. For this reason we use an adaptive time stepping method proposed very recently by Van der Giessen and Neale (1993), in which the time step size Δt to be used for each increment is determined adaptively through an automatic procedure consisting of three key parts:

Part 1: The first two steps are performed with very small time steps such that any plastic deformation is excluded. The size of the time step is defined as a small fraction of a reference time scale t_R,

$$\Delta t = 10^{-8} t_R \ , \quad t_R = \frac{s_0}{\mu \dot{\gamma}^p}\left[1 + \frac{T}{A s_0}\ln\left(\frac{\dot{\gamma}^p}{\dot{\gamma}_0}\right)\right]^{6/5} ,$$

which, in a loose sense, relates the viscoplastic shear rate $\dot{\gamma}^p$ according to Eq. (5.1) with the elastic shear rate $\dot{\Gamma}$ under the same stress.

Part 2: At the beginning of the third time step, the time increment is determined on the basis of a prescribed work rate per unit volume, $W = (\dot{F}_s \dot{U} \Delta t) / (4 A_0 B_0)$, during that step. The applied work rate is estimated on the basis of the 'elastic' stress state determined as discussed above, and W is scaled with the elastic shear modulus μ, i.e. $W \equiv \varepsilon_W \mu$. Thus, the time increment is obtained from

$$\Delta t = \varepsilon_W \frac{4 \mu A_0 B_0}{\dot{F}_s \dot{U}}$$

and its size is controlled by the parameter ε_W.

Part 3: During all subsequent increments, a maximum allowable time step Δt_m is determined as the maximum value of $\Delta t'$ computed from each of the following criteria:

$$\Delta t' \le \varepsilon_s \frac{s}{h\left|1 - s/s_{ss}\right| \dot{\gamma}^p} \ ;$$

$$\Delta t' \le \frac{\Delta \gamma^p_{\max}}{\dot{\gamma}^p} \ . \qquad (5.16)$$

The first criterion ensures that the shear stress drop during a time increment $\Delta t'$ does not exceed a fraction ε_s of the current shear strength. The second criterion ensures that the plastic shear strain increment during a time increment $\Delta t'$ does not exceed a maximum shear increment $\Delta \gamma^p_{\max}$. If at the end of the increment, Δt_m is smaller than the current time step Δt, the time step of the next increment is taken equal to Δt_m; if Δt_m exceeds Δt for a number of consecutive increments (say, five), Δt is increased by a factor 1.5.

As pointed out by Van der Giessen and Neale (1993), the procedure is rather heuristic, but extremely simple to implement in an incremental code. This adaptive time step selection procedure involves three parameters, the values of which have to be determined empirically. The results to be presented in the next two sections have all been obtained with the following values: $\varepsilon_W = 10^{-8}s^{-1}$, $\Delta\gamma^p{}_{max} = 0.0025$, $\varepsilon_s = 0.01$. These values have been found to ensure numerical stability in all cases to be presented. Several cases have been repeated with half of the above values, and in each case the differences in the global response quantities (shear and normal stresses) remained smaller than 0.1%.

We would like to note that powerful forward gradient approaches for the time integration of viscoplastic constitutive equations have been proposed in the literature (e.g. Peirce *et al.*, 1984). However, these methods are very difficult to apply to the present set of constitutive equations because of the structure of the back stress equations (5.3)–(5.7). By employing the afore-mentioned, simple adaptive time stepping scheme we have been quite efficient in obtaining stable solutions with acceptable numbers of increments.

5.4. PARAMETER STUDY

The problem described in Sec. 5.3 involves a number of dimensionless groups, and therefore we introduce the following nondimensional quantities:

$$\text{loading:} \quad \Gamma = \frac{U}{2A_0}\,,\ \sigma_s = \frac{F_s}{2B_0 s_0}\,,\ \sigma_n = \frac{F_n}{2B_0 s_0}\,,\ \frac{\dot{\Gamma}}{\dot{\gamma}_0}; \tag{5.17}$$

$$\text{geometry:} \quad B_0/A_0; \tag{5.18}$$

$$\text{material:} \quad \frac{E}{s_0}\,,\ \frac{s_{ss}}{s_0}\,,\ \frac{As_0}{T}\,,\ \frac{h}{s_0}\,,\ \nu\,,\ \alpha\,,\ N\,,\ \frac{C^R}{s_0}. \tag{5.19}$$

The overall response of the specimen can be conveniently presented in terms of the applied shear strain Γ, and the normalized nominal shear stress and normal stress, σ_s and σ_n respectively.

5.4.1. A typical result

Figure 5.2 shows the predicted response to plane strain simple shear, using a regular mesh with 12×60 elements (12 equally sized elements in the direction perpendicular to the shear direction, 60 in the shear direction). The specimen dimensions are specified by $B_0/A_0 = 15$, and the following values of the material parameters were used: $\dot{\Gamma}/\dot{\gamma}_0 = 1.5 \times 10^{-18}$, $E/s_0 = 9.38$, $s_{ss}/s_0 = 0.92$, $As_0/T = 79.2$, $h/s_0 = 9.28$, $\nu = 0.3$, $\alpha = 0.08$, $N = 6.3$, $C^R/s_0 = 0.06$. These values, except the value E/s_0 , were primarily used as representative values of the parameters, but are reasonable for polycarbonate among other amorphous glassy polymers. In the BPA model, the value of E/s_0 is determined uniquely by Poisson's ratio. However, here we consider it to be an independent material parameter. The reason for this is that the constitutive model described in Sec. 5.2 cannot account for the small strain viscoelastic behaviour observed in experiments, resulting in a nonlinear stress-strain response prior to yielding. Now, since we are mainly interested in large plastic deformations, these viscoelastic effects need not be considered in detail, and we shall simply characterize the behaviour prior to yielding by an appropriate value of E. The intensity ξ of the initial imperfection (see Eq. (5.15)) is assumed to be 0.01. We will use these values of the parameters throughout Sec. 5.4, except were noted otherwise.

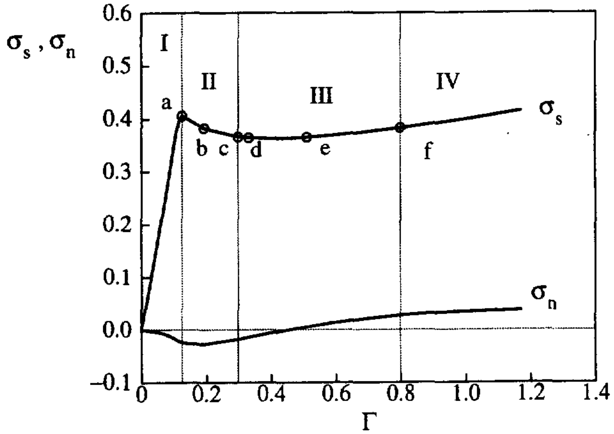

Fig. 5.2. Typical predicted simple shear behaviour for a specimen with $B_0/A_0 = 15$, $\xi = 0.01$ and for the following values of the material parameters: $\dot{\Gamma}/\dot{\gamma}_0 = 1.5 \times 10^{-18}$, $E/s_0 = 9.38$, $s_{ss}/s_0 = 0.92$, $As_0/T = 79.2$, $h/s_0 = 9.28$, $\nu = 0.3$, $\alpha = 0.08$, $N = 6.3$, $C^R/s_0 = 0.06$. Stages a–f correspond to the plots shown in Fig. 5.3.

The four successive stages of the experimental shear stress–shear strain curve distinguished by G'Sell and Gopez (1985) are picked up qualitatively by the simulation (Fig. 5.2): (I) the elastic response ending at a yield strain of about 0.12; (II) a small but significant shear stress drop, spreading over a strain range from 0.12 to 0.3; (III) a plastic domain with a very small apparent slope, spreading over a strain range from 0.3 to about 0.8; (IV) large plastic flow of the sample with enhanced hardening. The calculation ended when the maximum plastic stretch approached the locking stretch $\sqrt{N}$ of the macromolecular chain network at some point in the specimen.

Figure 5.2 also shows the development of the normal stress σ_n during simple shear. The compressive normal stress increases up to an applied strain of 0.18, where it approaches its maximum of about 0.027. From that point on, the normal stress starts to increase increases monotonically towards a constant positive value. The normal stresses remains compressive up to an applied strain of about 0.5, and then becomes tensile.

G'Sell and Gopez (1985) showed that the four stages in the shear stress–shear strain behaviour can be partly attributed to the intrinsic material behaviour, and partly to the occurrence of a macroscopic shear band. In order to clearly show the initiation and propagation of the shear band, Fig. 5.3 shows contour plots of the plastic shear strain γ^p normalized by the "applied plastic strain"

$$\Gamma^p = \Gamma - F_s/(2B_0\mu),$$

at different stages of the deformation (the stages a–f correspond to the points marked a–f in Fig. 5.2). As the shear stress passes through its maximum at $\Gamma \approx 0.12$, a region of enhanced shear appears at the location of the initial imperfection (see Fig. 5.3.a). It is noted that in addition, two regions of enhanced shear are found near the free edges. During continued deformation, these regions quickly grow into shear bands: the shear band initiated at the center elongates in the shear direction while the other two propagate towards the center of the specimen (see Fig. 5.3.b) until they link up with each other and form a single shear band at around $\Gamma = 0.30$ (see Fig. 5.3.c). Then the so-formed single shear band gradually widens (Fig. 5.3.d and Fig. 5.3.e). As observed in experiments, the local plastic shear strain within the shear band continues to increase at a very slow rate during band widening. Figure 5.3.f shows the contour plots when the band occupies the whole specimen.

Fig. 5.3. Contours of normalized plastic shear strain γ^p/Γ^p under simple shear predicted with the 12×60 mesh at various shears: (a) $\Gamma = 0.12$, (b) $\Gamma = 0.20$, (c) $\Gamma = 0.30$, (d) $\Gamma = 0.33$, (e) $\Gamma = 0.51$, (f) $\Gamma = 0.80$.

The physical cause for shear band propagation is evident from the evolution of the shear stress. When the band of increased plastic flow is initiated near the center, the local shear stress drops sharply as a consequence of the intrinsic softening. With continued applied shearing, orientation hardening starts to develop in the shear band, causing the neighbouring material to reach the local shear resistance and initiate substantial plasticity. This process continues until most of the specimen is well in the plastic, strain hardening regime.

5.4.2. Influence of the mesh

Shear band localization phenomena are notorious for sometimes exhibiting a pathological mesh sensitivity. However, as put forward unequivocally by Needleman (1988), this is not necessarily the case for the problem under consideration here since the material response according to the constitutive model of Sec. 5.2 is intrinsically rate-dependent. Nevertheless, the selection of a proper mesh does require attention. Numerical experiments have shown that the overall response of the specimen, in terms of the overall shear stress and normal stress are not sensitive to the mesh; but it turned out that details of shear band formation and propagation are indeed rather sensitive to the mesh used. In order to obtainsufficiently accurate results, we have to use somewhat fine mesh.

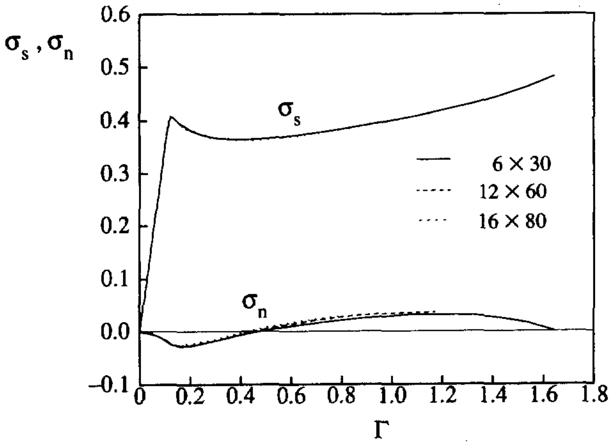

Fig. 5.4. Shear and normal stress responses under simple shear predicted with different finite element meshes.

Figure 5.4 shows the predicted responses to plane strain simple shear, using three different regular meshes consisting of 6×30, 12×16 and 16×80 elements. In all these calculations, we have used the same parameters as given in Sec. 5.4.1.

Figure 5.5 gives the contour plots of plastic shear strain at various stages of the deformation with the mesh (16×18). It is clear that the contour plots with mesh (16×80) are almost identical to these with mesh (12×60), which have been discussed in detail before. However, when the crude mesh (6×30) is used (see Fig. 5.6), we do not observe the thin shear band at the location of the initial imperfection up to shear strains about 0.3 (stages a and b of Fig. 5.6). The reason for this is that the width of a shear band at the early stages is very small; if it is smaller than the element size of the mesh, it will not be picked up in the analysis.

Further detailed studies of the distributions of plastic shear strain and stresses reveal that the edge effects are very strong. Indeed, the maximum plastic stretch always approaches the locking stretch of the macromolecular chain network at a location near the edges. On the other hand, the extent of the stress concentration is sensitive to the mesh used. Using a crude mesh tends to reduce the stress concentration. Actually, the most important difference between the crude and the fine meshes in Fig. 5.4 is that the maximum plastic stretch formed with the fine mesh (16×80) approaches the locking stretch at an applied shear strain of about only 0.8, while in the crude mesh (6×30) the locking stretch is not reached prior to $\Gamma = 1.6$. Based on all those observations, we decided that the relatively fine mesh (12×60) would be sufficiently accurate. We will use this mesh in the rest of this paper, except where noted otherwise.

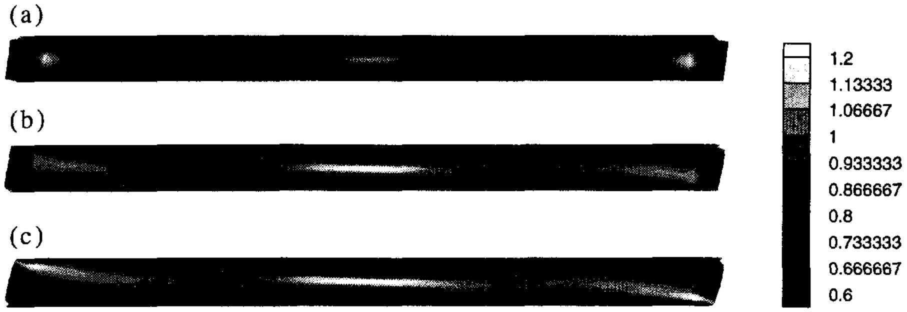

Fig. 5.5. Contours of normalized plastic shear strain γ^p/Γ^p for the 16×80 mesh at various deformation stages: (a) $\Gamma = 0.12$, (b) $\Gamma = 0.20$, (c) $\Gamma = 0.30$.

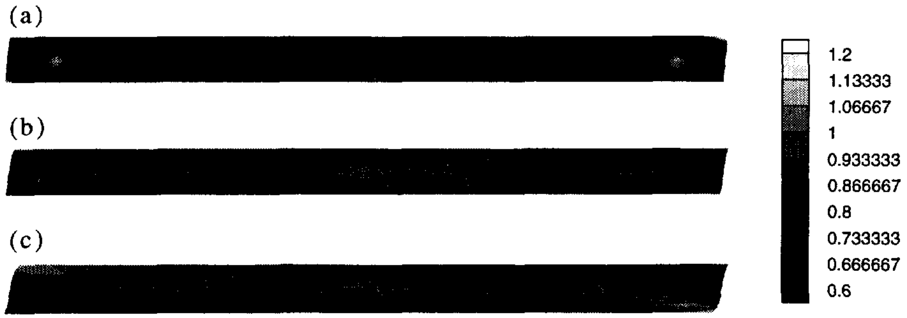

Fig. 5.6. Contours of normalized plastic shear strain γ^p/Γ^p for the 6×30 mesh at various deformation stages: (a) $\Gamma = 0.12$, (b) $\Gamma = 0.20$, (c) $\Gamma = 0.30$.

5.4.3. Effects of initial imperfection

To check the influence of the initial imperfection on the localization results, we have used different imperfection shapes and sizes. It was found in all cases that, within the strain-range considered, the overall response is not sensitive to the initial imperfection. In fact, we hardly see the effect of the initial imperfection on the overall response from the predicted shear and normal stresses. We have also studied the normalized plastic shear strain distribution by using the same imperfection shape, given by Eq. (5.15), but with different intensities ξ ranging from 0.005 to 0.02: the differences were found to be very small.

Nevertheless, it is interesting to consider the limiting case of an idealized specimen without initial imperfection ($\xi = 0$). Figure 5.7 shows the normalized plastic shear strain distribution in this case. As opposed to Fig. 5.3, there is no shear band initiated at the centre of the specimen. However, we do observe the two regions of intense shear near the free edges (Fig. 5.7.a), which propagate towards the center of the specimen during softening (see Figs. 5.7.b,c) until they join each other and form a single shear band at an applied shear strain about 0.33. Then the so-formed shear band gradually widens until it occupies the entire area of the specimen (see Fig. 5.7.d). From that point on, the differences in plastic shear strain distribution between the specimens with and without an initial imperfection are no longer distinguishable.

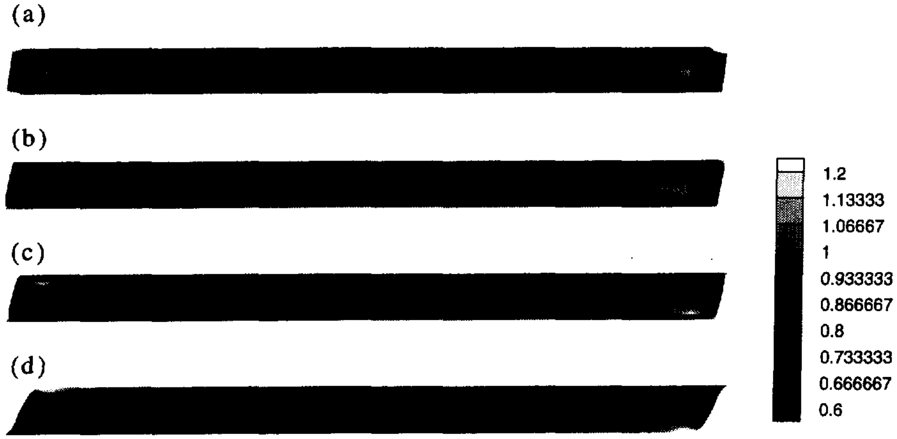

Fig. 5.7. Contours of normalized plastic shear strain γ^p/Γ^p in an idealized specimen without an initial imperfection at various deformation stages: (a) $\Gamma = 0.12$, (b) $\Gamma = 0.19$, (c) $\Gamma = 0.30$, (d) $\Gamma = 0.80$.

5.4.4. Effects of material properties

It is generally agreed that the yield and postyield behaviour of glassy polymers exhibit true strain softening [see e.g. Haward (1980)]. In the BPA model, the effects of softening are described in terms of the evolution equation of the athermal yield strength (5.2). We study the effects of softening on shear band initiation and propagation by considering different intensities of softening, by taking $s_{ss}/s_0 = 0.92$ and 0.79, respectively. The associated value of the parameter h, the slope of the yield drop with respect to plastic strain, is adjusted in such a way that the initial slope of softening, $h\,(1 - s_0/s_{ss})$, remains constant. We also include the limiting case of no softening by assuming $s_{ss}/s_0 = 1$.

Figure 5.8 shows the effects of softening on the predicted shear and normal stress responses. As expected, the parameter s_{ss}/s_0 determines the extent of softening. Detailed consideration of the plastic shear strain distributions for the various cases indicates that there is no evidence of initiation and propagation of a shear band in the limiting case of no intrinsic softening. Discussion on the distributions of normalized plastic shear strain predicted with $s_{ss}/s_0 = 0.79$ will be given later.

The parameters N and C^R govern the orientation hardening through the non-Gaussian network model for rubber elasticity (5.6). Here, we study the effect of orientation hardening by first using the same value of N ($N = 6.3$) but different values of C^R: $C^R/s_0 = 0.06, 0.12$ and 0.18, respectively. Furthermore, we include a limiting case of no orientation hardening by taking $C^R/s_0 = 0$. In all these calculations, the intensity of softening is assumed to be $s_{ss}/s_0 = 0.79$. The numerical results are presented in Fig. 5.9. It is clear from the predicted shear stresses that a larger value of C^R/s_0 increases the stiffness of the network and therefore increases the orientation hardening. The value of C^R/s_0 is observed to affect the apparent overall yield stress too. The reason for this is that at the yield strain $\Gamma \approx 0.12$, significant plastic deformation has already occurred at some locations due to the intrinsic inhomogeneity of deformation. If C^R is large, orientation hardening would be already significant at that moment, resulting in a noticeable increase of the yield stress. The normal stress responses with different values of C^R/s_0 give virtually identical predictions up to $\Gamma = 0.2$, where they approach the maximum compressive stresse. From that point on, the normal stress for little ($C^R/s_0 = 0.06$) or no hardening ($C^R/s_0 = 0$) increases monotonically and becomes tensile at an applied shear strain of 0.25. As opposed to this result, the normal stress response for larger values of C^R/s_0 of 0.12 or 0.18 is not monotonic but reaches a maximum and then drops monotonically again. In the case of $C^R/s_0 = 0.18$ the normal stress response maintains compressive during the entire deformation process.

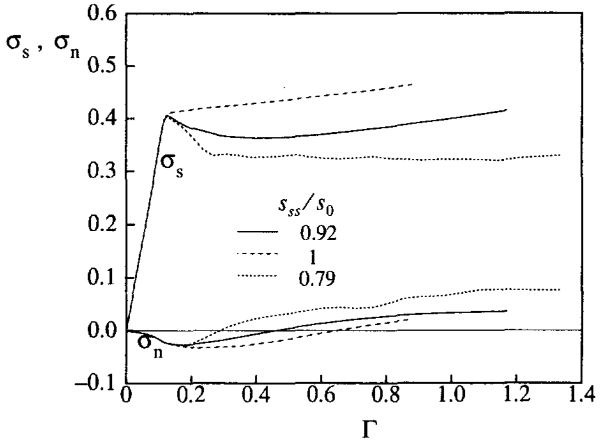

Fig. 5.8. Influence of the softening parameter s_{ss}/s_0 on the predicted shear and normal stress responses under simple shear. All other parameters are as in Fig. 5.2.

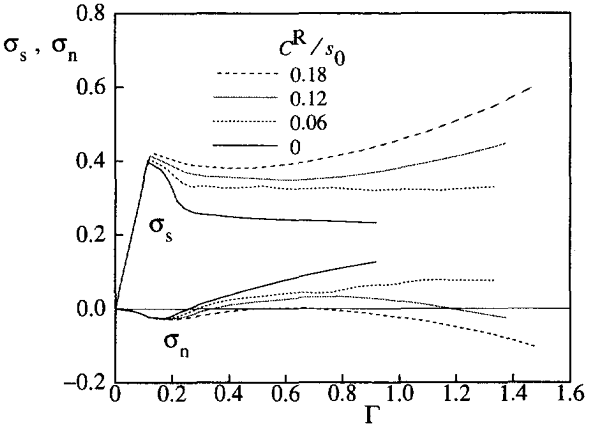

Fig. 5.9. Influence of the orientation hardening parameter C^R/s_0 on the predicted shear and normal stress responses under simple shear. Softening is characterized by $s_{ss}/s_0 = 0.79$, and all other parameters are as in Fig. 5.2.

The distributions of the normalized plastic shear strain predicted with relatively large values of C^R/s_0 (0.12 or 0.18) are found to be similar to those shown in Fig. 5.3. The distributions of normalized plastic shear strain obtained with $C^R/s_0 = 0$ (i.e. no orientation hardening) are given in Fig. 5.10. We did not observe a shear band at small strains up to $\Gamma \approx 0.16$. During continued deformation, the shear band initiated at the center (see Fig. 5.10.a) elongates in the shear direction while the other two, initiated near the free edges, propagate towards the center of the specimen (see Fig. 5.10.b) until they link up each other and form a single shear band (see Fig. 5.10.c). It is found that the so-formed shear band does not widen as we observed in the cases with a positive value of C^R/s_0,but localizes with further shearing (Figs. 5.10.d–e). The strain is concentrated in the shear band, as is seen from the profiles of the specimen in Figs. 5.10.d–e, while strains outside the band remain almost constant or even slightly decrease. This is also the reason why the predicted shear stress continues to decrease at large strains, as shown in Fig. 5.9. Eventually, the maximum plastic shear strain approachesthe limit value $\sqrt{N}$ at the surface of the shear band near the center of the specimen. In the case of small orientation hardening ($C^R/s_0 = 0.06$), the shear band is found to widen but very slowly.

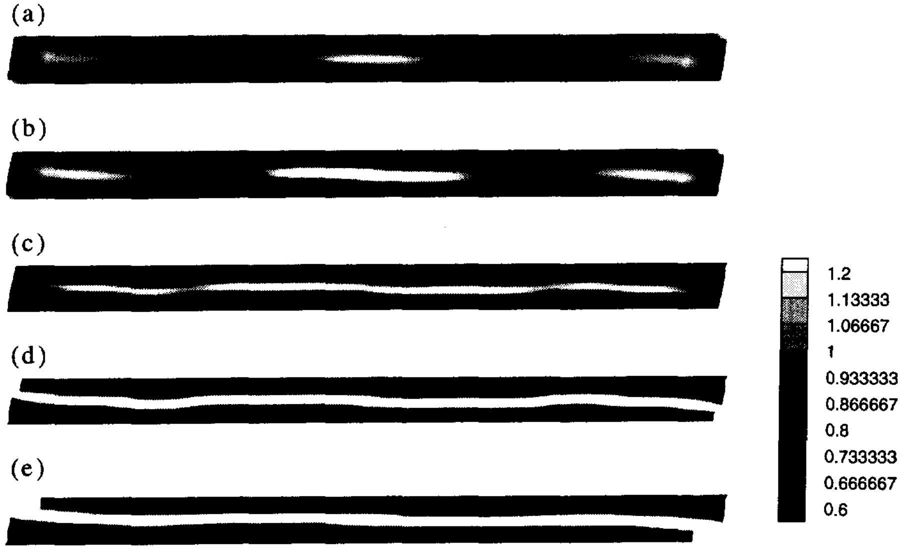

Fig. 5.10. Contours of normalized plastic shear strain γ^p/Γ^p for $C^R/s_0 = 0$ at various deformation stages: (a) $\Gamma = 0.16$, (b) $\Gamma = 0.18$, (c) $\Gamma = 0.22$, (d) $\Gamma = 0.34$, (e) $\Gamma = 0.77$.

We proceed by studying the effects of orientation hardening by using the same value of C^R ($C^R/s_0 = 0.06$) but different values of N: $N = 3.0, 6.3$ and 9.0. The results are presented in Fig. 5.11. The effects of N on the overall response of the simple shear test are not very strong, except for the fact that the limit stretches being reached at different strain levels.

Flow in amorphous glassy polymers appears to be a viscous process and the yield stress is strongly strain-rate dependent. Figure 5.12 shows the overall responses to simple shear deformation at normalized applied strain-rates $\dot{\Gamma}/\dot{\gamma}_0$ ranging over several orders of magnitude. The increase of the plastic flow stress due to an increase of the strain rate is seen to be small, about 7% for one decade of strain-rate. It seems that the main effect of strain-rate is to shift the shear stress strain curve vertically without changing its shape, while the normal stress is insensitive to the shear rate. The differences in plastic shear strain distributions under different strain-rates are found to be small, so that it is concluded that shear band initiation and propagation are not sensitive to strain-rate within the range considered.

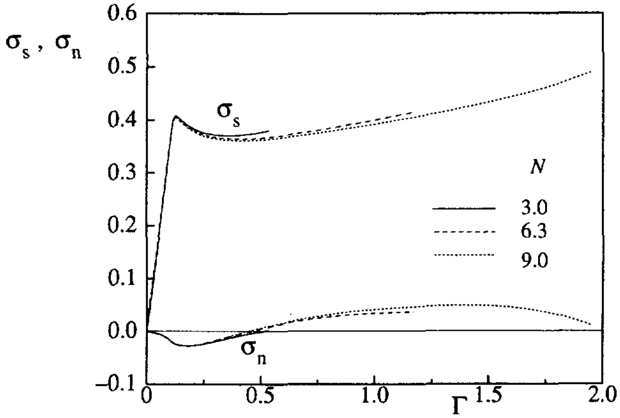

Fig. 5.11. Influence of the orientation hardening parameter N on the predicted shear and normal stress responses under simple shear for a material with $C^R/s_0 = 0.06$. All other parameters are as in Fig. 5.2.

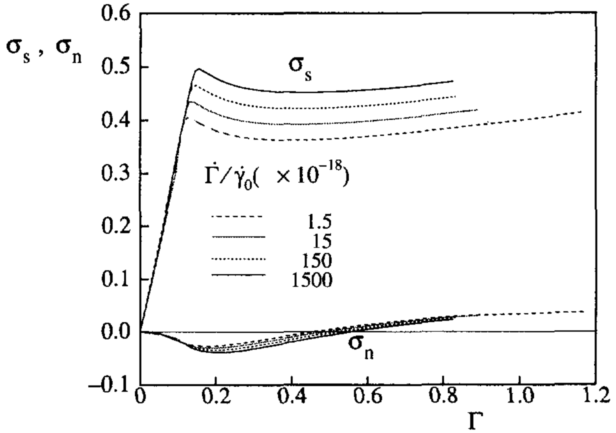

Fig. 5.12. Influence of the normalized applied strain-rate $\dot{\Gamma}/\dot{\gamma}_0$ on the predicted shear and normal stress responses to simple shear.

5.4.5. Edge effects

As mentioned before, the simple shear test carried out by G'Sell and co-workers is a highly inhomogeneous deformation process due to mainly the free edge effects. G'Sell *et al.* (1983) observed that the free edges of the specimen were curved and had a convex (bulging) curvature (see also the profiles of the specimen in Fig. 5.3). They explained these observations by, on one hand, the constraint effect of the grips, which react against the rotational moment imposed by the couple of the shearing forces, and on the other hand by the departure from the ideal simple shear condition in which the ends of the specimen must also carry appropriate tractions, in general normal to and parallel to the end surfaces.

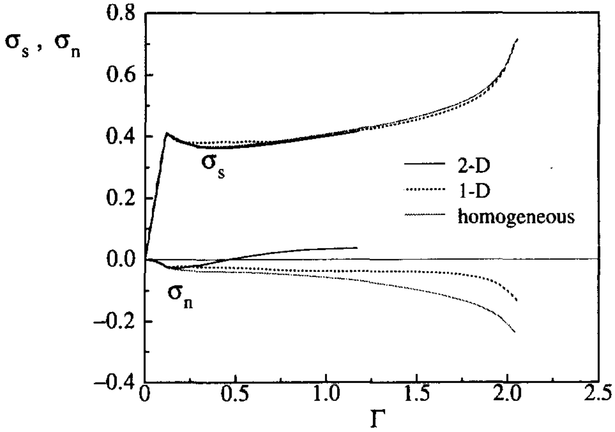

Fig. 5.13. Predicted shear and normal stress responses to homogeneous, 1-D ($B_0/A_0 \to \infty$) and 2-D ($B_0/A_0 = 15$) simple shear deformations, respectively. The material parameters are as in Fig. 5.2.

In a preliminary study, Wu and Van der Giessen (1992b) have considered the simple shear of a polycarbonate specimen of infinite length in the shear direction, i.e. $B_0/A_0 \to \infty$. The problem solved (Wu and Van der Giessen, 1992b) was effectively a one-dimensional problem across the width of the slab. In that analysis, the deformation inhomogeneity was reduced substantially because of the absence of free edges. To further assess the edge effects, we also calculated the stress response to homogeneous simple shear to a shear strain Γ by direct straighforward integration of the constitutive equations. The numerical results of these three different cases (referred to as homogeneous, 1-D and 2-D simple shear deformations, respectively) are presented in Fig. 5.13. Generally, the differences in predicted shear stress are small. This is further substantiated by Fig. 5.14 which shows the shear and normal stress distributions over the boundary a–b in the specimen (see Fig. 5.1) in the 2-D analysis at an applied shear strain of 0.6. It is seen that the shear stress distribution is relatively uniform over the boundary. Perhaps the only noteworthy difference in predicted shear stress response is that the 1-D calculation somewhat underestimates the strain softening (see Fig. 5.13). The reason for this is that in the 1-D analysis we essentially neglect the shear band propagation in the shear direction, while during those stages the shear stress should drop according to the experimental observation (G'Sell and Gopez, 1985). Once the shear band is complete at an applied strain of about 0.80, the shear stress response found in the 2-D case is virtually identical to that in the 1-D case. The very small systematic differences in predicted shear stress between the homogeneous case and the finite element calculations is probably due to the initial imperfection assumed in the latter.

Quite remarkably, the differences seen in Fig. 5.13 among the three cases in predicted overall normal stress are much larger than in the predicted shear stress. The calculations of all cases give virtually identical predictions of the compressive normal stress for applied strains up to $\Gamma = 0.12$. From that point on, the normal stresses in the homogeneous and 1-D cases evolve monotonically and remain compressive, whereas the overall normal stress found in the 2-D analysis becomes tensile eventually. Figure 5.14 now shows that the predicted normal stresses in the 2-D case along a–b are small and quite uniformly distributed over most of the boundary except at the corners b and a, where, high compressive and very high tensile stresses were found, respectively. The resulting average normal stress turns out to be tensile.

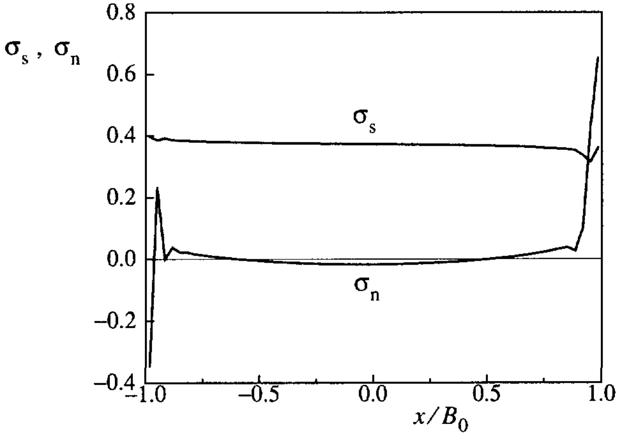

Fig. 5.14. Shear and normal stress distributions over the boundary a–b of the specimen (see Fig. 5.1) at an applied shear strain of $\Gamma = 0.6$.

Furthermore, G'Sell *et al.* (1983) reported that the perturbation in strain distribution caused by the free edges was significant in end zones of length equal to the width A_0 of the specimen. This means that the edge effects themselves depend on the aspect ratio B_0/A_0, and that the larger the value of B_0/A_0, the smaller the edge effects. While $B_0/A_0 = 15$ in previous computations, Fig. 5.15 shows the predicted shear and normal stress responses of a specimen with $B_0/A_0 = 7.5$. In this calculation, we used a regular mesh consisting of 24 × 60 elements. It is found that the shear stresses in the thick specimen ($B_0/A_0 = 7.5$) are slightly lower than these in the slender specimen ($B_0/A_0 = 15$); this is probably due to the fact that in all calculations we use the same initial imperfection shape (5.15), so that the average value of the initial shear strength ($s_0 - \Delta s_0$) in the thick specimen is then slightly smaller than that in the slender specimen. At large strains, the predicted tensile normal stresses in the thick specimen are much higher than that in the narrow specimen. Furthermore, the calculation for the thick specimen stopped at $\Gamma \approx 0.71$ when the maximum plastic stretch approached the locking stretch $\sqrt{N}$ of the network, while for the narrow specimen the locking stretch was not reached prior to $\Gamma \approx 1.2$. These observations clearly show that the edge effects increase with the thickness of the specimen. This is consistent with the conclusion of G'Sell *et al.* (1983).

To assess the influence of the geometry on the initiation and propagation of the shear band, Fig. 5.16 shows contour plots of the normalized plastic shear strain in the wide specimen at various stages of the deformation. Comparing with Fig. 5.3, it is clear that the velocity of the shear band propagation in the shear direction is much faster in the wide specimen than in the slender specimen; furthermore, the velocity in the thickness direction is lower in the wide specimen than in the slender specimen. Finally, the plastic strain concentration at the corner a of the wide specimen is much higher than that in the slender specimen.

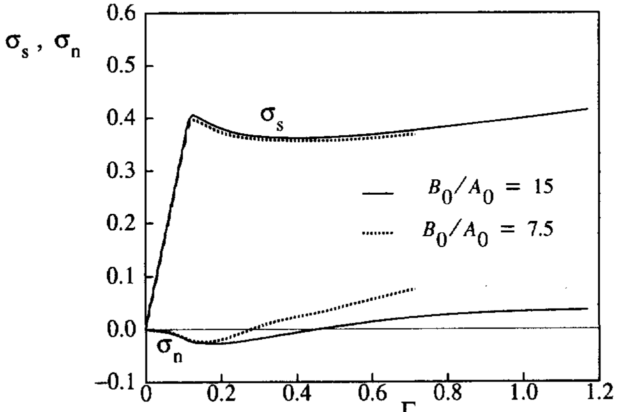

Fig. 5.15. Influence of the geometry parameter B_0/A_0 on the predicted shear and normal stress responses under simple shear.

Fig. 5.16. Contours of normalized plastic shear strain γ^p/Γ^p for the specimen with $B_0/A_0 = 7.5$ at various deformation stages: (a) $\Gamma = 0.12$, (b) $\Gamma = 0.20$, (c) $\Gamma = 0.30$, (d) $\Gamma = 0.71$. The material parameters are as in Fig. 5.2.

5.5. AN EXAMPLE FOR POLYCARBONATE

To enable a direct comparison with experimental data for polycarbonate (PC) by Gopez (1983) we have taken the actual dimensions to be the same as in (Gopez, 1983), i.e. $2A_0 = 4$

mm and $2B_0 = 60$ mm (see Fig. 5.1). The opposite faces are displaced at a constant velocity $\dot{U} = 1.2 \times 10^{-5} \mathrm{m/s}$ corresponding to an applied shear rate of $\dot{\Gamma} = 3 \times 10^{-3} \mathrm{s}^{-1}$.

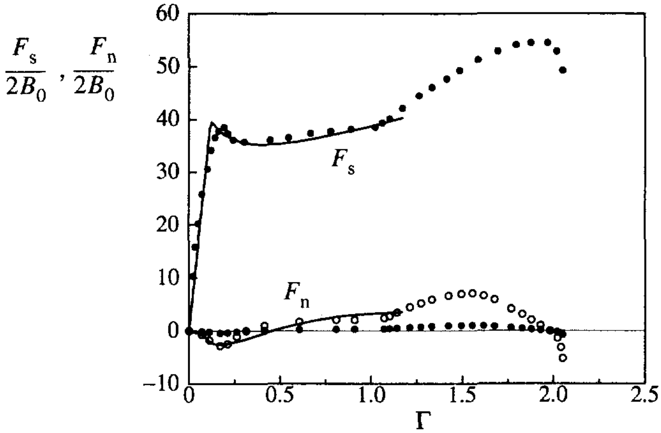

Fig. 5.17. Predicted overall shear and normal stress response to simple shear for polycarbonate. The dots (●) are experimental data points from Gopez (1983). The open circles (○) are the experimental values for the average normal stress σ_n multiplied by a factor 7.

At room temperature ($T = 294$ K), the following values of the parameters that determine the stress-rate, temperature dependence and softening behaviour for PC are used: $\dot{\gamma}_0 = 2 \times 10^{15} \mathrm{s}^{-1}$, $A = 240 \mathrm{K/MPa}$, $s_0 = 97$ MPa, $s_{ss}/s_0 = 0.92$, $h = 500 \mathrm{MPa}$ and $\alpha = 0.08$, while Young's modulus and Poisson's ratio are taken as $E = 910 \mathrm{MPa}$ and $\nu = 0.3$, respectively. Most of this data has been taken from the experiment carried out by Boyce and Arruda (1990); but, the saturation value s_{ss} has been chosen to fit the softening behaviour observed during large strain plastic torsion of PC by Wu and Turner (1973) (see also Wu and Van der Giessen, 1993c), while Young's modulus is chosen smaller than the experimental value of $E = 2300 \mathrm{MPa}$ for reasons discussed in the previous section. The parameters C^R and N that govern the orientation hardening are taken as $C^R = 5.7 \mathrm{MPa}$ and $N = 6.3$, which are reasonable compared with experimental values [see Reference 27 in (G'Sell, 1986)]. Admittedly, the material parameters have been compiled from different sources involving different experiments on material that is likely to be not exactly the same, but because of lack of sufficient experimental data this was the best we could do. We shall simply employ these parameters, bearing in mind that the major purpose of this paper is to numerically study the initiation and propagation of shear bands.

Figure 5.17 shows the predicted stress responses to plane strain simple shear, along with the experimental data by Gopez (1983). The characteristics of the predictions have already been discussed following Fig. 5.2, in which the numerical results were presented in terms of the nondimensional shear stress σ_s and normal stress σ_n defined in (5.17). The predicted shear stress is in a good agreement with the experimental data, but the predicted normal stress is found to be about 6 times larger in magnitude than the experimental data. For the prupose of a qualitative comparison with the experimental data, the figure also shows the experimental normal stress results multiplied by 7. It is seen that the shape of the predicted normal stress curve is quite unusual but similar to that observed experimentally in polycarbonate (Gopez, 1983). The contour plots of plastic shear strain at various deformation stages have been presented in

Fig. 5.3. The predicted initiation and subsequent propagation of the shear band is found to be in good agreement with experimental observations (G'Sell and Gopez, 1985). Therefore we conclude that the constitutive model, together with the numerical tool used here, is capable of capturing the major characteristics of the large simple shear behaviour in a qualitatively reasonable way.

5.6. DISCUSSION AND CONCLUSION

In this chapter, 2-D finite element analysis has been used to simulate large simple shear tests of amorphous glassy polymers, focussing attention on the initiation and propagation of the shear band. The mesh sensitivity and the effects of initial imperfection, strain softening, orientation hardening, strain-rate as well as the edge effects have been discussed in detail.

The predicted numerical results have been compared with experimental data for polycarbonate, based on material properties taken from independent sources. In general, the agreement is reasonable, and the initiation and propagation of shear bands is predicted well. However, a number of features in the experimental results are not picked up by the analysis.

Although the variations of thickness of the specimen are relevant to second-order terms in the strain tensor and may be neglected to a first approximation as suggested by G'Sell (1986), the simple shear test is in fact a three-dimensional problem. As reported by G'Sell and Gopez (1985), phenomena as cracking and the drawing of the material from outside the gauge section significantly affect the overall response at large strains. These 3-D effects can not be taken into account in the 2-D simulation. Therefore, the decrease in hardening slope, due to the microcracking and the drawing-in of material from the grip section at very large strains, is not picked up by the analysis (see Fig. 5.17). However, a constitutive model for describing the microcracking phenomenon is not available, while full 3-D analyses still impose severe computational requirements. On the other hand, these 3-D effects become critical only at very large strains (G'Sell *et al.*, 1983). Therefore, a proper plane strain type simple shear analysis should be of practical use.

The experiment carried out by Gopez (1983) showed increased hardening in the nominal shear stress-shear strain curve at strains beyond $\Gamma \approx 1.2$ (see Fig. 5.17). In the homogeneous and 1-D simple shear deformations, the predicted shear stresses go up rapidly when the maximum plastic stretches approach the locking stretch $\sqrt{N}$ of the molecular chain network (see Fig. 5.13). However, our plane strain type 2-D analysis did not reveal similar effects (see Fig. 5.13 or Fig. 5.17). This too is due to the inhomogeneity resulting from the edge effects. Actually, the local shear stress near the free edges does show accelerated hardening when the local maximum plastic stretch approaches $\sqrt{N}$. However, the maximum plastic stretch in locations away the free edges is still much less than $\sqrt{N}$, so that the resulting average shear stress does not exhibit this enhanced hardening.

We have demonstrated that a sufficiently fine mesh is needed in order to resolve the shear band. In a 3-D simulation of simple shear, Arruda and Boyce (1992) did not observe a shear band at the location of the initial imperfection. It is likely that this is caused by the fact that their mesh, which used only 6 elements in the direction perpendicular to the shear direction, was not fine enough. Our plastic shear strain distributions obtained with a sufficiently fine mesh clearly show the initiation and propagation of the shear band (see Fig. 5.3 or Fig. 5.5), which is in good agreement with the experimental observations (G'Sell and Gopez, 1985). However, it is worthwhile to point out that —perhaps unexpectedly— the predicted shear band is not a straight line parallel to the shear direction (see Fig. 5.3.c or d). G'Sell and co-workers have not clearly indicated the shape of the shear band in their experimental observations, but the experiments carried out very recently by Meijer and co-workers (1993) at Eindhoven University of Technology strongly support our predicted shear band shapes.

As pointed out by Grenet and G'Sell (1990), an important problem in polymer science is to understand what are the driving factors that control the kinetics of shear band propagation. Our numerical results indicate that there is no evidence of initiation and propagation of a shear band in the limiting case of no intrinsic softening. Thus, it appears that the intrinsic softening is the driving force to promote initiation of the shear band and its propagation in the shear direction. The effects of orientation hardening on initiation and propagation of shear band have also been studied. In the limiting case of no orientation hardening, the fully elongated shear band will localize (see Fig. 5.10) and the applied strain will concentrate entirely in the band. Therefore we conclude that orientation hardening is the driving force for widening of the shear band.

The secondary normal stress during simple shear is mainly due to the development and subsequent rotation of the induced anisotropy. For the amorphous polymers considered here, this anisotropy is associated with the stretching of the entangled molecular chain structure. It is well-known that the prediction of such second-order phenomena generally shows a rather strong dependence on the constitutive models —in particular the description of anisotropic hardening—and thus provide an effective means for assessing the adequacy of such constitutive models. Although advances in the understanding of second-order effects appear to come primarily from researches on metals (see e.g. Harren *et al.*, 1989; Van der Giessen *et al.*, 1992a), a number of characteristic aspects in amorphous glassy polymers now begins to be assessed (see e.g. Wu and Van der Giessen, 1993a, 1993b, 1993c). Figure 5.17 shows that although the normal stress predicted with the present constitutive model is much larger than the experimental data, its shape is similar to that observed experimentally. As we mentioned before, the unrealistically large normal stress is likely to be due in part to the high stress concentration at the corners (see Fig. 5.14). Taking into account the effects of microcracking and the drawing-in of the material from outside the gauge section, will reduce the stress concentration, and the resulting nominal normal stress will be improved significantly.

We have discussed the effects of initial imperfections in some detail. It was found that, within the strain-range considered, the overall response in terms of nominal shear and normal stresses is not sensitive to the initial imperfection. This supports the approximation involved in previous numerical simulations of the large strain plastic torsion test (Wu and Van der Giessen, 1993c): the overall response is only affected slightly by the shear band propagation process. This is particularly convenient when such tests are to be used for the determination of material parameters. It thus seems that the torsion test provides an excellent means for obtaining experimental data for the constitutive behaviour of elastic-plastic solids at large to very large deformations. The major advantage over the simple shear test is that deformations of a solid bar in torsion remain axially homogeneous up to final failure without having to give attention to shear banding (Wu and Van der Giessen, 1993c).

Concerning the constitutive aspects, it is noted that we used the affine network theory to model orientational hardening. The idea of using an affine network theory to model the stretching of the molecular network assumes that the junction points in the network remain in tact.

However, it has been suggested in the literature [see e.g. Raha and Bowden (1972) and Botto *et al.* (1987)] that physical entanglements in amorphous polymers are being pulled out during deformation. In terms of our network model this would mean that the number of chains n reduces in the course of the deformation process, while the number of links N per chain increases, thus reducing the stiffness of the network. This would reduce the predicted normal stress level, and at the same time extend the numerical simulation to larger strains by increasing the limit stretch. Furthermore we note that especially the normal stress predicted here may depend sensitively on the particular way of incorporating deformation-induced anisotropy by means of the Mises type effective shear stress concept in (5.9). This is likely to be rather important in the above simple shear problem, where the stress history is non-proportional and significant rotations of the principal axes occur. A totally different approach to modelling orientational hardening has been adopted by Batterman and Bassani (1990). All these constitutive aspects require further study. The formulation of improved models and their implications are in progress and will be reported elsewhere.

Chapter 6

On Neck Propagation in Amorphous Glassy Polymers under Plane Strain Tension

Abstract—Unlike metals, necking in polymers under tension does not lead to further localization of deformation, but to propagation of the neck along the specimen. Finite element analysis is used to numerically study necking and neck propagation in amorphous glassy polymers under plane strain tension during large strain plastic flow. The constitutive model used in the analyses features strain-rate, pressure and temperature dependent yield, softening immediately after yield and subsequent orientational hardening with further plastic deformation. The latter is associated with distorting the underlying molecular network structure of the material, and is modelled here by adopting a recently proposed network theory developed for rubber elasticity. Previous studies of necking instabilities have almost invariably employed idealized prismatic specimens; here, we explicitly account for the unavoidable grip sections of test specimens. The effects of initial imperfections, strain softening, orientation hardening, strain-rate as well as of specimen geometry and boundary conditions are discussed. The physical mechanisms for necking and neck propagation, in terms of the present constitutive model, are discussed on the basis of a detailed parameter study.

6.1. INTRODUCTION

Necking and neck propagation are typical examples of plastic instability phenomena in amorphous glassy polymers. Although our understanding of plastic instabilities appears to come primarily from researches on polycrystalline metals and soils, a number of characteristic aspects of localization instabilities in polymers begins to be assessed [see e.g. Bowden (1973), G'Sell (1986), Boyce *et al.*, (1989), Wu and Van der Giessen (1993d)]. It is now widely acknowledged that glassy polymers exhibit plastic deformation below the glass transition temperature mainly through the activation of microscopic shear bands. On the macroscopic scale, it is well-known that macroscopic strain localization in polymers can be very different from that in metals due to the dramatic stiffening of polymers at large strains. While plastic instabilities like necks or shear bands in metals almost invariably tend to localize progressively until failure intervenes, necks and macroscopic shear bands in polymers typically do not continue to localize but tend to propagate along the specimen [see e.g. G'Sell *et al.* (1983), Neale and Tugcu (1985), Buisson and Ravi-Chandar (1990), Tomita (1993), Wu and Van der Giessen (1993d)].

Neck propagation, or commonly termed cold drawing, is a standard technique used to orient the molecular chains of the polymers and thereby to harden the polymer of products such as fibres (axisymmetric deformation) and magnetic tape and sheet materials (plane strain deformations). Cold drawing has been studied experimentally for instance by G'SELL and co-workers [see e.g. G'Sell and Jonas (1979), Marquez-Lucero *et al.* (1989), and G'Sell *et al.* (1992)]. Except under conditions of very slow neck propagation, frictional heating of the polymer undergoing large deformations brings thermodynamic considerations into the problem. However, the phenomenon of neck propagation is in essence a mechanical one, and therefore the problem is usually considered as a quasi-static deformations under isothermal conditions.

Coleman (1983) and Hutchinson and Neale (1983) consider the ideal steady-state phase of neck propagation. For a nonlinear elastic solid described by J_2 deformation theory, Hutchinson and Neale (1983) determined the states on both sides of the neck from the jump conditions (across the neck) that result from conservation of mass, momentum and energy. An approximate solution was given for an elastic-plastic solid described by J_2 flow theory that was based on introducing a parameterized stream function into a variational principle. Subsequently, full finite element analyses have been carried out for axisymmetric neck propagation [Neale and Tugcu (1985), Tomita *et al.* (1990)] and for plane strain neck propagation [Fager and Bassani (1986), Tugcu and Neale (1987a)]. The effects of strain rate sensitivity (Tugcu and Neale, 1987a, b, 1988), and kinematic hardening (Tugcu and Neale, 1987a) on neck propagation behaviour have been also investigated.

The constitutive models used in the above mentioned studies are rather simple and entirely phenomenological. In most studies, the hardening response was simply chosen to fit the characteristic uniaxial stress-strain response of highly deformable, (semi-)crystalline polymers. Potentially more accurate constitutive models, based on detailed micromechanical considerations, have appeared very recently. In this paper we focus on the class of amorphous glassy polymers for which, on the one hand, the more phenomenological constitutive models used in previous necking studies do not apply, and for which on the other hand more physically based models have appeared recently. Using the 3-D constitutive model for amorphous glassy polymers proposed by Boyce *et al.* (1988), Boyce and Arruda (1990) studied the large strain tensile response of glassy polymers. Although the predicted true stress-strain curve was found to accurately capture the observed test data, the kinetics of necking and neck propagation was not discussed in their paper.

The fully 3-D constitutive model for amorphous glassy polymers, proposed originally by Boyce *et al.* (1988) and modified by Wu and Van der Giessen (1993a), has been found to be able to predict many aspects of the large plastic strain behaviour of glassy polymers observed experimentally (Wu and Van der Giessen, 1993a, 1993b, 1993c). In a recent study, a finite element simulation of shear band propagation in glassy polymers during plane strain simple shear was carried out (Wu and Van der Giessen, 1993d), focusing attention on the initiation and propagation of the shear band. The numerical results showed that the shear band propagation phenomenon could be captured by the type of constitutive models available now. In this chapter, the constitutive model is incorporated in finite element simulations of the plane strain tension of amorphous glassy polymers, focusing attention on the initiation of necking and neck propagation along the specimen. Results are given for the overall load-elongation response and the thickness reduction-elongation response of the specimen. In some cases the deformed meshes and the distributions of plastic strain rate at various deformation stages are provided. Based on the detailed parameter analyses, the mechanisms of necking and neck propagation are discussed in some detail.

Tensors will be denoted by bold-face letters. The tensor product is denoted by ⊗ and the following operations for second and fourth-order tensors apply ($\mathbf{a} = a_{ij}\mathbf{e}_i \otimes \mathbf{e}_j$, $\mathbf{b} = b_{ij}\mathbf{e}_i \otimes \mathbf{e}_j$, $\underset{\sim}{\mathcal{A}} = \mathcal{A}_{ijkl}\mathbf{e}_i \otimes \mathbf{e}_j \otimes \mathbf{e}_k \otimes \mathbf{e}_l$, $\mathbf{e}_i$ being a Cartesian basis): $\mathbf{ab} = a_{ik}b_{kj}\mathbf{e}_i \otimes \mathbf{e}_j$ and $\underset{\sim}{\mathcal{A}}\mathbf{b} = \mathcal{A}_{ijkl}b_{kl}$. Superscripts T and −1 denote the transverse and inverse of a second-order tensor, respectively. The trace is denoted by tr, and a superposed dot denotes the material time derivative or rate. The deviatoric part of a second-order tensor $\mathbf{a}$ is denoted by a prime, i.e. $\mathbf{a}' = \mathbf{a} - (\mathrm{tr}\,\mathbf{a}/3)\,\mathbf{I}$, with $\mathbf{I}$ being the unit tensor.

6.2. CONSTITUTIVE EQUATIONS

In this section, we briefly recapitulate the constitutive framework we are going to adopt throughout this paper, mainly for the purpose of definition and notation. For details we refer to Boyce *et al.*, (1988) and Wu and Van der Giessen (1993a). It is assumed that before large strain inelastic flow may occur a glassy polymer must overcome two physical distinct sources of resistance: (a) an intermolecular resistance to segment rotation; and (b) an anisotropic internal resistance due to molecular alignment.

Argon (1973) has developed a relatively simple model for plastic flow made possible by the cooperative rotation of segments. According to this model, the plastic shear strain rate $\dot{\gamma}^{\mathrm{p}}$ due to an applied shear stress τ is given by

$$\dot{\gamma}^{\mathrm{p}} = \dot{\gamma}_0 \exp\left[-\frac{As_0}{T}\left(1 - \left(\frac{\tau}{s_0}\right)^{5/6}\right)\right]. \tag{6.1}$$

Here, $\dot{\gamma}_0$ is a pre-exponential factor, A is a material parameter that is proportional to the activation volume/Boltzmann's constant, T is the absolute temperature and s_0 is the athermal shear strength, which in ARGON's model is given by $s_0 = 0.077\mu/(1-\nu)$ in terms of the elastic shear modulus μ and Poisson's ratio ν. BOYCE *et al.* [1988] extended this expression to include the effect of the pressure p by using $s + \alpha p$ instead of s_0, where α is a pressure dependence coefficient. Furthermore, they accounted for intrinsic softening by assuming s to evolve with plastic straining via

$$\dot{s} = h\,(1 - s/s_{\mathrm{ss}})\,\dot{\gamma}^{\mathrm{p}} \tag{6.2}$$

where h is the rate of resistance drop with respect to the plastic strain and s_{ss} is the assumed saturation value of s.

During continued plastic flow, the molecular chains will tend to align along the direction of principal plastic stretch [see e.g. Haward and Thackray (1968) and Argon (1973)]. This molecular 'texture' development tends to decrease the configurational entropy of the system which, in turn, creates an internal network stress. This process of network distortion is very similar to that of rubber network, and Haward and Thackray (1968) suggested to describe this for uniaxial extension by means of a back stress determined through a Langevin spring, as suggested by non-Gaussian network theory. Boyce *et al.* (1988) extended this approach to general three-dimensional plastic deformations by introducing a back stress tensor **B** which is taken to be coaxial with the plastic left stretch tensor $\mathbf{V}^{\mathrm{p}}$. Thus, if $\mathbf{e}_i^{\mathrm{p}}$ are the unit eigen vectors of $\mathbf{V}^{\mathrm{p}}$, corresponding to a plastic stretch λ_i^{p}, the back stress **B** is constructed as

$$\mathbf{B} = \sum_i B_i (\mathbf{e}_i^{\mathrm{p}} \otimes \mathbf{e}_i^{\mathrm{p}}) \tag{6.3}$$

from the principal components B_i. Originally, BOYCE *et al.* (1988) adopted the classical so-called three-chain model for which the principal components $B_i^{3-\mathrm{ch}}$ of the back stress tensor are given in terms of the plastic stretches λ_i^{p} by (see Wang and Guth, 1952)

$$B_i^{3\text{-ch}} = \frac{1}{3} C^{\mathrm{R}} \sqrt{N} \left[\lambda_i^{\mathrm{p}} \mathcal{L}^{-1}\left(\frac{\lambda_i^{\mathrm{p}}}{\sqrt{N}}\right) - \frac{1}{3} \sum_{j=1}^{3} \lambda_j^{\mathrm{p}} \mathcal{L}^{-1}\left(\frac{\lambda_j^{\mathrm{p}}}{\sqrt{N}}\right) \right] \quad \text{(no sum over } i\text{)}, \tag{6.4}$$

where C^{R} is known as the rubbery modulus, N is a statistical network parameter related to the network locking stretch and $\mathcal{L}$ is the Langevin function defined by $\mathcal{L}(\beta) = \coth\beta - 1/\beta$.

Later, Arruda and Boyce (1991, 1993b) found that the three-chain non-Gaussian network model was not capable of picking up the strain hardening observed experimentally in polycarbonate (PC) and polymethylmetacrylate (PMMA). They suggested to model the network by the so-called eight-chain model which considers a set of eight chains connecting the central junction point and each of the eight corners of the unit cube. The principal components of the back stress tensor according to this eight-chain non-Gaussian network model are given by

$$B_i^{8\text{-ch}} = \frac{1}{3} C^{\mathrm{R}} \sqrt{N} \mathcal{L}^{-1}\left(\frac{\lambda^{\mathrm{p}}}{\sqrt{N}}\right) \frac{\lambda_i^{\mathrm{p}\,2} - \lambda^{\mathrm{p}\,2}}{\lambda^{\mathrm{p}}}, \qquad \lambda^{\mathrm{p}\,2} = \frac{1}{3} \sum_{j=1}^{3} \lambda_j^{\mathrm{p}\,2}. \tag{6.5}$$

Obviously, the eight-chain model is but on approximate representations of the actual spatial distributions of molecular chains by "lumping" their orientations in eight specific directions. More precisely, the eight-chain model would underestimate the stiffness of the network because of the excessive freedom of the central junction point in the unit cube (Dahoun *et al.*, 1993). Very recently, the authors developed the so-called full network model in which full account is taken of the 3-D orientation distribution of the individual chains in the network (Wu and Van der Giessen, 1992a, 1993a). The principal back stresses according to this model can be given by

$$B_i = \frac{1}{4\pi} C^{\mathrm{R}} \sqrt{N} \int_0^{\pi} \int_0^{2\pi} \mathcal{L}^{-1}\left(\frac{\lambda^{\mathrm{p}}}{\sqrt{N}}\right) \frac{\lambda_i^{\mathrm{p}\,2} m_i^{0\,2} - \lambda^{\mathrm{p}\,2}/3}{\lambda^{\mathrm{p}}} \sin\theta_0 \, d\theta_0 \, d\varphi_0 \quad \text{(no sum over } i\text{)}. \tag{6.6}$$

Here, λ^p is defined by

$$\lambda^{p^2} = \sum_{j=1}^{3} \lambda_j^{p^2} m_j^{0^2}$$

and m_i^0 are the unit vector components in orientation space defined by

$$m_1^0 = \sin\theta_0\cos\varphi_0, \qquad m_2^0 = \sin\theta_0\sin\varphi_0, \qquad m_3^0 = \cos\theta_0.$$

in terms of the angles θ_0 and φ_0 which measure the orientation of molecular chains relative to the principal stretch directions in the undeformed configuration. The numerical evaluation of the integral in (6.6) is rather time-consuming, but an accurate approximation of the full network predictions according to (6.6) has been found (Wu and Van der Giessen, 1992a) in the form of a combination of the three-chain and eight-chain model predictions (6.4), (6.5) through

$$B_i = (1-\rho^p)\,B_i^{3\text{-ch}} + \rho^p B_i^{8\text{-ch}}. \tag{6.7}$$

Excellent agreement with full integration is obtained by taking ρ^p to be related to the maximum principal plastic stretch $\lambda_{\max}^p = \max(\lambda_1^p, \lambda_2^p, \lambda_3^p)$ via $\rho^p = 0.85\lambda_{\max}^p/\sqrt{N}$. All computations to be reported here have used the expression (6.7).

The complete tensorial form of the constitutive model has been developed by Boyce *et al.*, (1988), in which the deformation gradient **F** is multiplicatively decomposed into elastic and plastic parts, $\mathbf{F} = \mathbf{F}^e\mathbf{F}^p$. With no loss of generality, the elastic part $\mathbf{F}^e$ is taken to be symmetric, so that $\mathbf{F}^p$ represents the relaxed configuration obtained by unloading without rotation (in the polar decomposition sense). According to this decomposition, the velocity gradient **L** is decomposed as

$$\mathbf{L} = \dot{\mathbf{F}}\mathbf{F}^{-1} = \mathbf{D}+\mathbf{W} = \dot{\mathbf{F}}^e\mathbf{F}^{e^{-1}} + \mathbf{F}^e\mathbf{L}^p\mathbf{F}^{e^{-1}}$$

where **D** is the rate of deformation, **W** is the spin, and $\mathbf{L}^p = \mathbf{D}^p + \mathbf{W}^p = \dot{\mathbf{F}}^p\mathbf{F}^{p^{-1}}$ is the velocity gradient in the relaxed configuration. With the adopted symmetry of $\mathbf{F}^e$, the skewsymmetric part $\mathbf{W}^p$ is algebraically given as **W** plus a term dependent on $\mathbf{F}^e$ and $\mathbf{D}+\mathbf{D}^p$ (Boyce *et al.*, 1988). Since the elastic strains will remain small, we can neglect geometry differences between current and relaxed configurations. Thus, the constitutive equations can be simplified significantly. In particular it is noted that in this case $\mathbf{W}^p \approx \mathbf{W}$ and $\mathbf{D} \approx \mathbf{D}^e + \mathbf{D}^p$, with $\mathbf{D}^e$ the symmetric part of $\dot{\mathbf{F}}^e\mathbf{F}^{e^{-1}}$ (see Boyce *et al.*, 1988).

The magnitude of the strain rate $\mathbf{D}^p$ (the rate of shape change of the relaxed configuration) is taken to be given by the plastic shear strain rate, $\dot{\gamma}^p$, according to (6.1) while the tensor direction of $\mathbf{D}^p$ is specified by **N**, so that

$$\mathbf{D}^p = \dot{\gamma}^p\mathbf{N}, \tag{6.8}$$

where the direction **N** is the deviatoric part of the driving stress, normalized by the effective equivalent shear stress τ:

$$\mathbf{N} = \frac{1}{\sqrt{2}\tau}\tilde{\boldsymbol{\sigma}}', \qquad \tau = \sqrt{\frac{1}{2}\tilde{\boldsymbol{\sigma}}' \cdot \tilde{\boldsymbol{\sigma}}'}. \tag{6.9}$$

The driving stress $\tilde{\boldsymbol{\sigma}}$ itself is defined by

$$\tilde{\boldsymbol{\sigma}} = \boldsymbol{\sigma} - \mathbf{B} \tag{6.10}$$

where $\boldsymbol{\sigma}$ is the Cauchy stress tensor and $\mathbf{B}$ is the back stress tensor, according to (6.3) and (6.6) or (6.7). By observing that $\mathbf{V}^2 = \mathbf{F}^{\mathrm{e}}(\mathbf{V}^{\mathrm{p}})^2(\mathbf{F}^{\mathrm{e}})^T$ it is seen that, consistent with neglecting the elastic geometry changes ($\mathbf{F}^{\mathrm{e}} \approx \mathbf{I}$), the plastic principal stretches λ_i^{p} to be substituted into (6.4)–(6.6) are approximated by the principal values of $\mathbf{V} \approx \mathbf{V}^{\mathrm{p}}$.

The Cauchy stress is taken to be given by the elastic constitutive law with the hypoelastic rate form and employing the Jaumann stress rate, $\overset{\nabla}{\boldsymbol{\sigma}} = \dot{\boldsymbol{\sigma}} - \mathbf{W}\boldsymbol{\sigma} + \boldsymbol{\sigma}\mathbf{W}$ to retain objectivity,

$$\overset{\nabla}{\boldsymbol{\sigma}} = \underset{\sim}{\mathcal{L}}_{\mathrm{e}}\mathbf{D}^{\mathrm{e}} \tag{6.11}$$

where $\underset{\sim}{\mathcal{L}}_{\mathrm{e}}$ is the fourth-order isotropic elastic modulus tensor:

$$\underset{\sim}{\mathcal{L}}_{\mathrm{e}} = \mathcal{L}_{\mathrm{e}}^{ijkl}\,\mathbf{e}_i \otimes \mathbf{e}_j \otimes \mathbf{e}_k \otimes \mathbf{e}_l,$$

$$\mathcal{L}_{\mathrm{e}}^{ijkl} = \frac{E}{2(1+\nu)}\left[(\delta^{ik}\delta^{jl} + \delta^{il}\delta^{jk}) + \frac{2\nu}{1-2\nu}\delta^{ij}\delta^{kl}\right], \tag{6.12}$$

with $E = 2(1+\nu)\mu$ being Young's modulus. The constitutive equations (6.11) can be finally arranged in the following form:

$$\overset{\nabla}{\boldsymbol{\sigma}} = \underset{\sim}{\mathcal{L}}_{\mathrm{e}}\mathbf{D} - \dot{\boldsymbol{\sigma}}_{\mathrm{v}} \tag{6.13}$$

where $\dot{\boldsymbol{\sigma}}_{\mathrm{v}} = \underset{\sim}{\mathcal{L}}_{\mathrm{e}}\mathbf{D}^{\mathrm{p}}$ acts as an instantaneous stress rate term that represents the viscoplastic contribution.

6.3. PROBLEM FORMULATION AND METHOD OF SOLUTION

We consider a tensile test specimen with grips as shown in Fig. 6.1, which has a gauge section with a rectangular cross-section. Contrary to most necking studies found in the literatures, we do not just consider the prismatic gauge section, but also include the thicker grip sections. The reason for doing so is that after substantial neck propagation, the neck will approach the end of the gauge section and may then interact with the grips used to load the specimen. At that stage, velocity or strain fields at the interface between gauge section and grips become distorted, and it would be very difficult to accurately determine the boundary conditions for the gauge section.

In the initial configuration, the gauge section has a length $2B_0$ and a thickness $2A_0$. A Cartesian coordinate system with $x_1 = x$, $x_2 = y$, $x_3 = z$ is used as a reference, in which x is associated with the loading direction, while y refers to the thickness direction. The transition from the gauge section thickness $2A_0$ to the grip thickness $2H_0$ occurs over a length

L_e, and is for simplicity described analytically by

$$y = A_0 + (H_0 - A_0)\left(1 - \frac{\arctan\left(Q\dfrac{L_e + B_0 - x}{L_e}\right)}{\arctan Q}\right), \qquad B_0 \leq x \leq (B_0 + L_e),$$

where the parameter Q determines how steep the transition is. The elongation in the gauge section is commonly expressed by the ratio $\varepsilon = U_g / B_0$, where the gauge section displacement U_g is determined as the average displacement over the section $x = B_0$ in the initial configuration. The specimen is deformed by imposing the displacement rate $\dot{U}$ in the x direction at the free end without restraining the lateral movement so that the rate boundary conditions at $x = L_0$ become

$$\dot{T}^y(L_0, y) = 0, \qquad \dot{u}_x(L_0, y) = \dot{U}, \tag{6.14}$$

where T^y is the nominal traction vector component in y direction. Thus the loading is displacement controlled and the grip surface $x = L_0$ is shear free. From symmetry about $x = 0$, we have

$$\dot{T}^y(0, y) = 0, \qquad \dot{u}_x(0, y) = 0. \tag{6.15}$$

The strain rate in the gauge section is approximately defined by $\dot{\varepsilon} = \dot{U}/B_0$. The lateral surfaces of the specimen are taken to be stress-free. Variations of the width (in z direction) during the deformation are neglected; thus, the deformation is plane strain. The conventional nominal stress or engineering stress is defined by $F_x / (2A_0)$, where F_x is the applied tensile force. Furthermore, we define a thickness-reduction ratio $\kappa = A_N / A_0$ at the minimum section, which for the present problem always coincides with $x = 0$. Because of the symmetry with respect to the mid-planes $x = 0$, $y = 0$, only one quadrant of the symmetry specimen needs to be analysed (see Fig. 6.1).

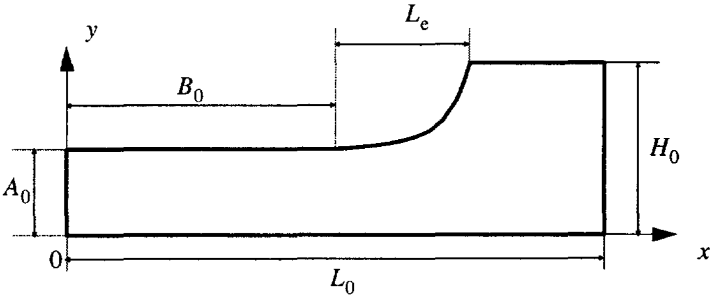

Fig. 6.1. Schematic definition of the plane strain tension specimen under (only one quadrant is shown).

In most experiments and perhaps all numerical simulations [see e.g. G'Sell and Jonas (1979), Neale and Tugcu (1985)], an initial 'geometric' imperfection was used to trigger the initiation of the neck. However, in the experiments carried out by G'Sell *et al.* (1992) and G'Sell and Marquez-Lucero (1993), a predeformation defect was introduced centrally in each specimen by folding and defolding the specimen locally. It was shown that such a 'mechanical' defect acts as an efficient neck initiator in those cases where a neck is likely to be formed (G'Sell and Marquez-Lucero, 1993). To trigger the initiation of the neck at the mid-plane $x = 0$ of the specimen in our numerical analysis, we assume here an initial mechanical imperfection of the shear strength s_0 of the form

$$\Delta s_0 = \zeta s_0 \cos\frac{\pi x}{B_0} \tag{6.16}$$

such that the actual initial shear strength is $s_0 - \Delta s_0$, where ζ determines the intensity of the imperfection.

A numerical analysis is performed by employing a finite element scheme in a manner similar to that described by Needleman and Tvergaard (1984). We use quadrilateral elements, each built up of four linear velocity, triangular subelements arranged in a 'crossed triangle' configuration. The initiation and propagation of the shear bands has been observed during large strain deformations in amorphous glassy polymers [see e.g. Wu and Turner (1973), G'Sell and Gopez (1985)], while the element size defines the minimum possible thickness of the shear band. Therefore, an analysis with a fine mesh could result in a narrower shear band. The shear band will form along element boundaries. The quadrilateral element mesh formation provides a greater freedom for the deformation to localize because of the large number and direction of element boundary (Tvergaard *et al.*, 1981). An equilibrium correction procedure is employed in this analysis to avoid drifting away from the true equilibrium path during the incremental procedure. Integrations with respect to time are computed using an explicit Euler integration method. Since the elements of the stiffness matrix are of the order of the elastic moduli, very small time steps have to be employed to achieve satisfactory convergence in the early stages of viscoplastic flow; however, at later stages of well-developed viscoplastic flow, much large steps may be used. For this reason we use an adaptive time stepping method proposed very recently by Van der Giessen and Neale (1993) and used in the numerical simulations of shear band propagation at large plane strain simple shear by Wu and Van der Giessen (1993d), in which the time step size Δt to be used for each increment is determined adaptively. The procedure uses a number of criteria which ensure that the shear stress drop and the plastic shear strain increment during a time increment remain within user-defined bounds. The procedure is rather heuristic, but extremely simple to implement in an incremental code. By employing this simple adaptive time stepping scheme we have been quite efficient in obtaining stable solutions with acceptable numbers of increments. For further details concerning the finite element method, we refer to Wu and Van der Giessen (1993d).

6.4. RESULTS

The problem described in Sec. 6.3 involves a number of dimensionless groups, and therefore we introduce the following nondimensional quantities:

$$\text{loading:}\quad \varepsilon = \frac{U_g}{B_0},\quad \sigma = \frac{F_x}{2A_0 s_0},\quad \kappa = \frac{A_N}{A_0},\quad \frac{\dot{\varepsilon}}{\sqrt{3}\dot{\gamma}_0}; \tag{6.17}$$

$$\text{geometry:}\quad B_0/A_0,\ L_0/B_0,\ L_e/L_0,\ H_0/A_0,\ Q; \tag{6.18}$$

$$\text{material:}\quad \frac{E}{s_0},\ \frac{s_{ss}}{s_0},\ \frac{As_0}{T},\ \frac{h}{s_0},\ \nu,\ \alpha,\ N,\ \frac{C^R}{s_0}. \tag{6.19}$$

The overall response of the specimen can be conveniently presented in terms of the applied strain ε, and the normalized nominal stress σ and the thickness-reduction ratio κ at the minimum section ($x = 0$).

6.4.1. A typical result

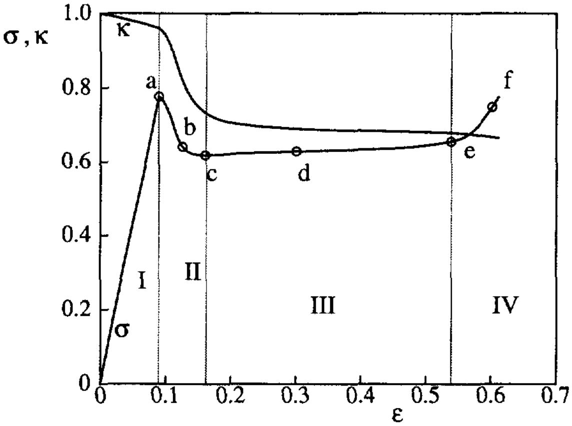

Fig. 6.2. Typical predicted plane strain tension behaviour for a specimen with $B_0/A_0 = 4$, $L_0/B_0 = 2$, $L_e/L_0 = 1/4$, $H_0/A_0 = 2$, $Q = 7.2$, $\zeta = 0.01$ and for the following values of the material parameters: $\dot{\varepsilon}/(\sqrt{3}\dot{\gamma}_0) = 2.89\times10^{-18}$, $E/s_0 = 9.38$, $h/s_0 = 5.15$, $s_{ss}/s_0 = 0.79$, $As_0/T = 79.2$, $\nu = 0.3$, $\alpha = 0.08$, $N = 2.8$, $C^R/s_0 = 0.132$. Stages a–f correspond to the plots shown in Fig. 6.3 and Fig. 6.4.

Figure 6.2 shows the predicted response for specimen dimensions specified by $B_0/A_0 = 4$, $L_0/B_0 = 2$, $L_e/L_0 = 0.2$, $H_0/A_0 = 2$, $Q = 7.2$. The following values of the material parameters were used: $\dot{\varepsilon}/(\sqrt{3}\dot{\gamma}_0) = 2.89\times10^{-18}$, $E/s_0 = 9.38$, $s_{ss}/s_0 = 0.79$, $As_0/T = 79.2$, $h/s_0 = 5.15$, $\nu = 0.3$, $\alpha = 0.08$, $N = 2.8$, $C^R/s_0 = 0.132$. These values, except for the value of E/s_0, were primarily used as representative values of the parameters, but are quite reasonable for polycarbonate among other amorphous glassy polymers. In Argon's (1973) model, the value of E/s_0 is determined uniquely by Poisson's ratio. However, here we consider it to be an independent material parameter, since the constitutive model described in Sec. 6.2 cannot account for the small strain viscoelastic behaviour observed in experiments, which results in a nonlinear stress-strain response prior to yielding. Now, as we are mainly interested in large plastic deformations, these viscoelastic effects need not be considered in detail, and we shall simply characterize the behaviour prior to yielding by an appropriate mean value of E (see also Wu and

Van der Giessen, 1993d). The intensity ξ of the initial imperfection (see Eq. (6.16)) is assumed to be 0.01. We will use these values of the parameters throughout Sec. 6.4, except were noted otherwise. It should be noted that the gauge section displacement U_g in (6.17) is determined as the average displacement over the section which was located at $x = B_0$ in the initial configuration.

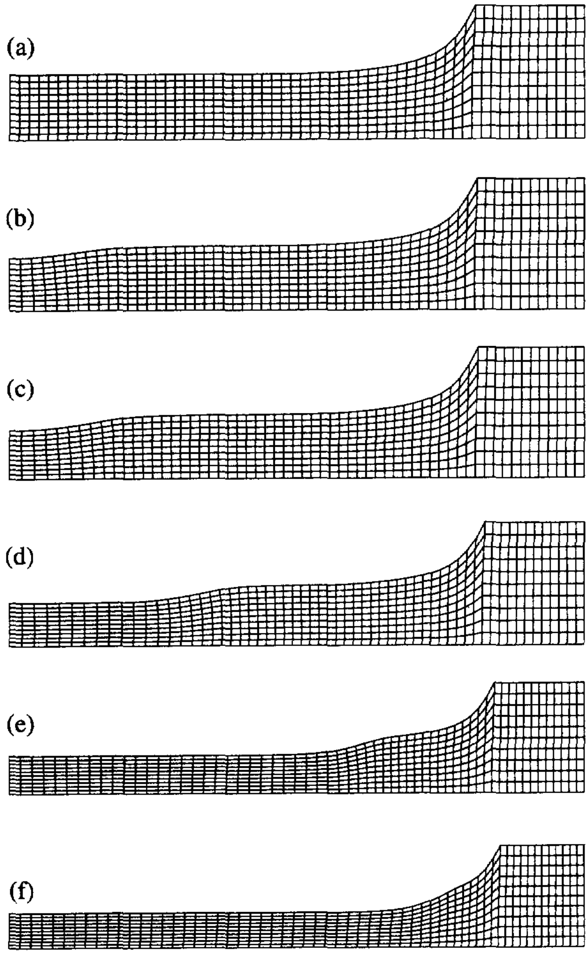

Fig. 6.3. Deformed meshes under plane strain tension at various deformation stages: (a) $\varepsilon = 0.09$, (b) $\varepsilon = 0.13$, (c) $\varepsilon = 0.16$, (d) $\varepsilon = 0.30$, (e) $\varepsilon = 0.54$, (f) $\varepsilon = 0.60$. All figures are scaled to the same apparent specimen length. The parameters are given in Fig. 6.2.

The four successive stages of the experimental force-elongation curve distinguished by Buisson and Ravi-Chandar (1990) are picked up qualitatively by the simulation (Fig. 6.2): (I) the elastic response ending at ε of about 0.10; (II) a significant force drop, spreading over a strain range from 0.10 to 0.16; (III) a plastic domain with a very small apparent slope, spreading over a strain range from 0.16 to about 0.54; (IV) large plastic flow of the sample with enhanced hardening. The calculation ended when the maximum plastic stretch approached the locking stretch $\sqrt{N}$ of the macromolecular chain network at some point in the specimen.

The process of neck localization and stabilization is also illustrated in Fig. 6.2, where the thickness-reduction ratio $\kappa = A_N/A_0$ at the minimum section ($x = 0$) is plotted as a function of the elongation $\varepsilon = U_g/B_0$. Here we see a rapid decrease in section thickness at the maximum axial force state, and thus represent the onset of localized necking. With further elongation this curve reaches a plateau indicating the stabilization of necking in the minimum section followed by neck propagation along the specimen. In the final stage with enhanced hardening, a somewhat faster decrease in section thickness is found.

The development of the neck is further depicted in Fig. 6.3 as a series of consecutive deformation states (deformed mesh), which clearly show the various stages of neck initiation (Fig. 6.3b), stabilization of neck and initiation of neck propagation (Fig. 6.3c) until locking up (Fig. 6.3f). Details of the process of neck propagation are illustrated in Fig. 6.4 which shows the contours of normalized plastic strain rate $\dot{\Sigma}^p$ defined by

$$\dot{\Sigma}^p = \frac{\dot{\gamma}^p}{\sqrt{3}}\left(\frac{\dot{U}}{B_0 + U_g}\right)^{-1} = \frac{(1+\varepsilon)}{\sqrt{3}}\frac{\dot{\gamma}^p}{\dot{\varepsilon}}.$$

In both Fig. 6.3 and Fig. 6.4 each state corresponds with states labelled (a) through (f) in the normalized force-elongation curve indicated in Fig. 6.2. The normalized plastic strain rate distributions indicate where in the specimen plastic flow is currently localized.

When the load reaches its maximum, a region of enhanced plastic flow occurs in the center of the specimen. This indicates the initiation of necking (Fig. 6.4a), although no neck is visible yet (see profile of the specimen in Fig. 6.4a and the deformed mesh in Fig. 6.3a). While the nominal stress decreases during stage II, a region of intense plastic strain rate develops, spread out over a region of finite extent (Fig. 6.4b). This is also demonstrated by the deformed mesh in which we observe that a finite region about the middle of the gauge section ($x = 0$) necks down more or less uniformly (Fig. 6.3b). A neck is visible at $\varepsilon \approx 0.13$ (Fig. 6.3b and Fig. 6.4b). In Fig. 6.4c the plastic strain rate distribution indicates two crossed, banded region of enhanced plastic flow. Although these regions do not exhibit all features of a shear band in the sense of a material instability, we shall refer to them as 'shear band' for simplicity. Note that there are *two* crossed sets of shear bands in the specimen, and the main band orients with the tensile loading axis at an angle of about 54° (rather than 45°). The neck stabilizes as orientation hardening starts to develop in the shear bands. This causes the neighbouring material to reach the local shear resistance and initiate substantial plasticity indicating neck propagation (Fig. 6.4d-f). This process continues until most of the specimen is well in the plastic, strain hardening regime (Fig. 6.4e and f). In this last stage, an apparent hardening also appears in the nominal stress-elongation curve (Fig. 6.2). During the process of neck propagation, the main shear band clearly indicates the front of the propagating neck. The maximum plastic strain rate always takes place at the symmetry line. Furthermore, the main shear band rotates from 54° to 64° with respect to the tensile axis during neck propagation (Fig. 6.4c-f). The reason for this rotation is perhaps the geometry of the specimen used here. When the shear band reaches the right end of the gauge section where the thickness of the specimen is smoothly increasing, the material on the right-hand side of the shear band will force the band to rotate away from the tensile axis.

Quite remarkably, our predicted neck is found to be very diffuse (See Fig. 6.3). This is in qualitative agreement with the experimental neck profiles for a typical amorphous polymer like polycarbonate (see eg. Buisson and Ravi-Chandar, 1990). However, it is noted that very sharp neck profiles have been observed for e.g. polyethylene (see e.g. G'Sell and Jonas, 1979), which is a semi-crystalline material.

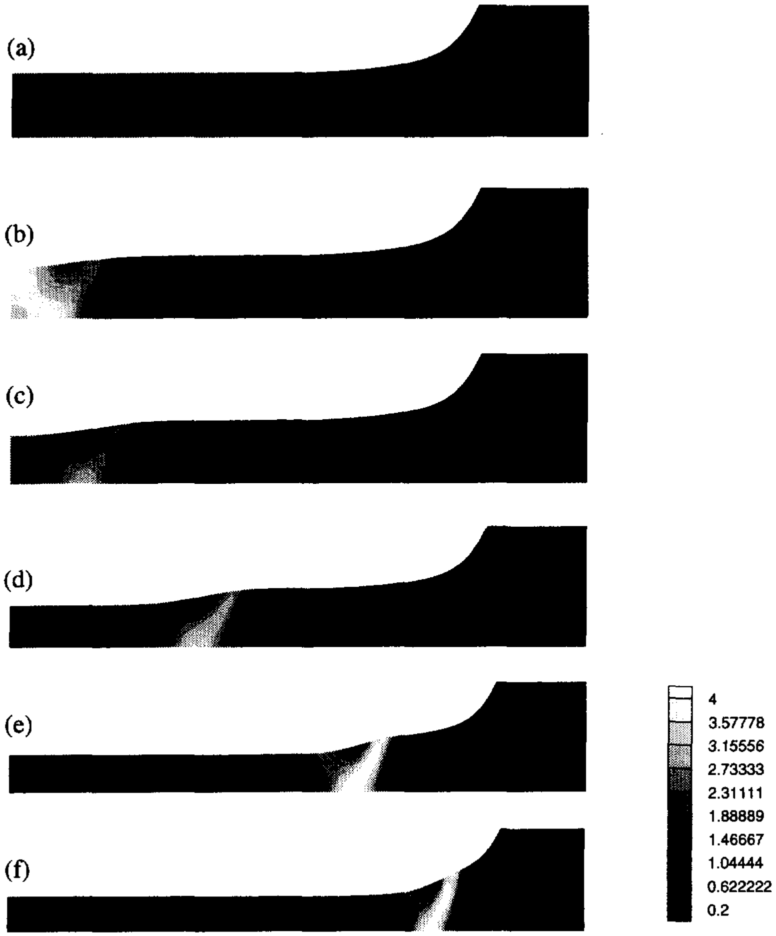

Fig. 6.4. Contours of normalized plastic strain rate $\dot{\Sigma}^{p}$ under plane strain tension at various deformation stages: (a) $\varepsilon = 0.09$, (b) $\varepsilon = 0.13$, (c) $\varepsilon = 0.16$, (d) $\varepsilon = 0.30$, (e) $\varepsilon = 0.54$, (f) $\varepsilon = 0.60$. All figures are scaled to the same apparent specimen length. The parameters are given in Fig. 6.2.

There are several other different ways to further demonstrate the initiation of necking and neck propagation. We have also depicted the stress and strain distributions across minimum section ($x = 0$) and along mid-plane ($y = 0$) at various stages of the deformation process. The numerical results are similar to those in Tugcu and Neale (1987).

At this point it is worthwhile to discuss very briefly the selection of the mesh. Since the material response according to the constitutive model of Sec. 6.2 is intrinsically rate-dependent, the mesh sensitivity frequently observed in computational modelling of plastic instability phenomena is not necessarily relevant for the problem under consideration here (see e.g. Needleman, 1988). However, the selection of a proper mesh does require attention because the element size defines the minimum possible thickness of the shear band which has been observed. We have used different meshes to simulate neck propagation under plane strain tension. Numerical experiments have shown that the overall response of the specimen, in terms of the overall nominal stress σ and the thickness-reduction ratio κ at the minimum section ($x = 0$) are not sensitive to the mesh. However, in order to clearly show the front of the propagating neck, a more or less fine mesh is needed. Based on a detailed analysis of the numerical experiments, we decided that a relatively fine mesh with 10×60 elements (10 equally sized elements in y direction, 60 in x direction) would be sufficiently accurate. We will use this mesh, as shown in Fig. 6.3a, except where noted otherwise.

6.4.2. *Effects of initial imperfection*

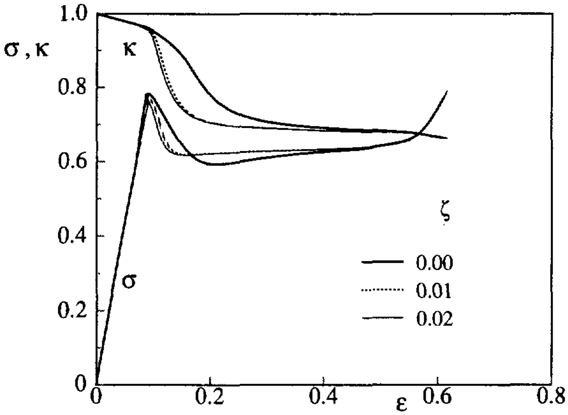

Fig. 6.5. Influence of an initial imperfection ζ on the predicted nominal stress response and thickness-reduction ratio under plane strain tension. All other parameters are as in Fig. 6.2.

To check the influence of the initial imperfection on necking and neck propagation, we have used different imperfection shapes and sizes in terms of the initial shear strength [cf (6.16)]. It was found in all cases that, within the strain-range considered and using the same relative imperfection size (ζ), the overall response is not sensitive to the initial imperfection shape. In fact, we hardly see the effect of the initial imperfection shape on the overall response from the predicted normalized load and thickness reduction. However, the initiation of necking is highly influenced by the amplitude of the initial imperfection. Figure 6.5 shows the predicted results by using the same imperfection shape, given by Eq. (6.16), but with different intensities ξ ranging from 0 to 0.02. It is found that, decreasing the initial imperfection increases the level of overall elongation at the onset of localization, and that an increasing defect amplitude has the effect of making the descending portion of the normalized load-elongation curve more abrupt (so that the propagation stages begins earlier).

After the neck has propagated far away from the central section, the influence of the initial imperfection on the overall responses in terms of σ and κ is no longer distinguishable. Detailed comparisons of deformed meshes using different initial imperfections at various stages of the deformation indicated also that the influence of initial imperfection is very small at large elongations. Furthermore, it should be noted that the specimen we used can be considered as a prismatic specimen having an intrinsic geometric imperfection caused by the grip sections. Therefore, it is not necessary with our specimen to apply an additional initial imperfection for triggering the initiation of necking. As is well-known, in the case of an idealized prismatic specimen (no initial imperfection) with shear free ends there is no evidence of necking and neck propagation.

6.4.3. *Effects of material properties*

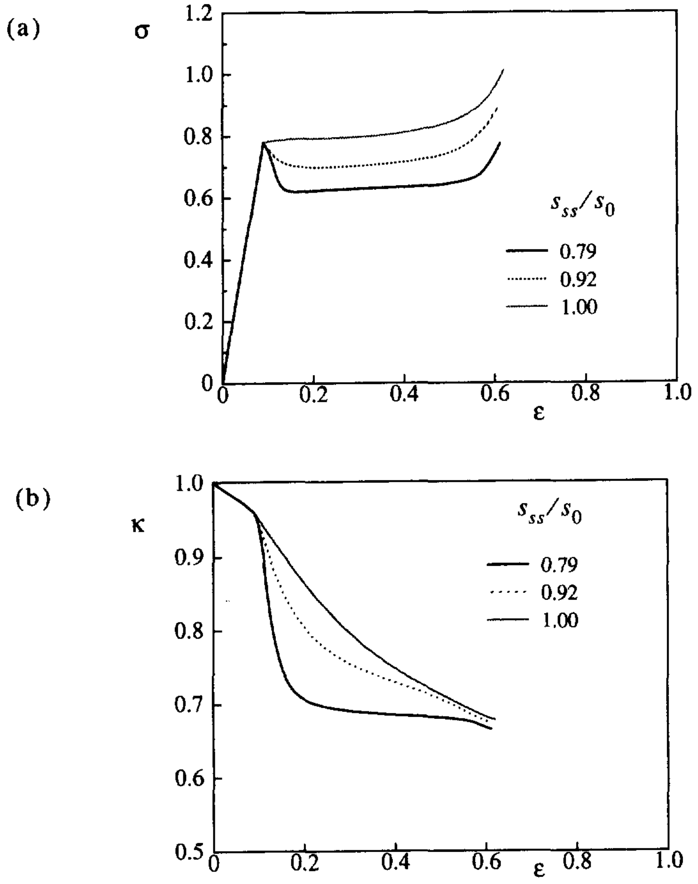

Fig. 6.6. Influence of the softening parameter s_{ss}/s_0 on the predicted nominal stress response (a) and thickness-reduction ratio (b) to plane strain tension. All other parameters are as in Fig. 6.2.

It is generally agreed that the yield and postyield behaviour of glassy polymers exhibit true strain softening [see e.g. Haward (1980)]. In the BPA model, the effects of softening are described in terms of the evolution equation of the athermal yield strength (6.2). We study the effects of softening on the initiation of necking and neck propagation by considering different intensities of softening, by taking $s_{ss}/s_0 = 0.79$ and 0.92, respectively. The associated value of the parameter h, the slope of the yield drop with respect to plastic strain, is adjusted in such a way that the initial slope of softening, $h\,(1 - s_0/s_{ss})$, remains constant. We also include the limiting case of no intrinsic softening by assuming $s_{ss}/s_0 = 1$.

Figure 6.6a shows the effects of softening on the predicted normalized nominal stress σ. Although the value of the parameter s_{ss}/s_0 determines the extent of intrinsic softening, it is noted that the apparent softening observed in the normalized force-elongation curve in plane strain tension is partly attributed to the intrinsic material behaviour (*intrinsic softening*), and partly to the occurrence of a reduction of the cross sectional area (*geometric softening*). With the values of the orientation hardening parameters C^R and N used here, the assumption of no intrinsic softening results in no apparent softening in the normalized load-elongation curve (see Fig. 6.6a).

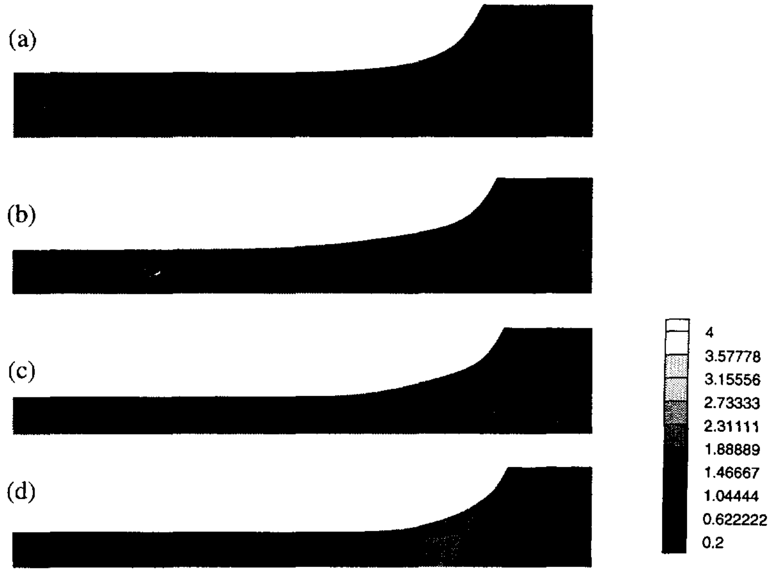

Fig. 6.7. Contours of normalized plastic strain rate $\dot{\Sigma}^p$ in the case of no intrinsic softening nor permanent softening under plane strain tension at various deformation stages: (a) $\varepsilon = 0.09$, (b) $\varepsilon = 0.38$, (c) $\varepsilon = 0.53$, (d) $\varepsilon = 0.60$. All figures are scaled to the same apparent specimen length.

The effect of intrinsic softening on the initiation of necking and neck propagation is more evident from the predicted thickness-reduction ratio κ at the minimum section $x = 0$ shown in Fig. 6.6b. Although almost the same minimum thickness-reduction ratio $\kappa_{min} \approx 0.66$ is obtained, the evolution curves of κ are quite different between specimens with different values of intrinsic softening. An increasing intrinsic softening amplitude tends to accelerate the process of neck localization. Detailed comparisons between the plastic strain rate distributions and that in Fig. 6.4 shows that, although neck propagation begins later, the pattern of necking and neck propagation in the specimen with less intrinsic softening ($s_{ss}/s_0 = 0.92$) is similar to that in Fig. 6.4. In the case of no intrinsic softening, the thickness-reduction ratio κ is a nearly linear function of applied elongation ε. Detailed analysis of the deformed profiles of the specimen at various stages of the deformation process indicates that there is no clear evidence of initiation of necking nor of neck propagation in this limiting case of no intrinsic softening (nor apparent softening). The contours of normalized plastic strain rate at various deformation stages in this case are presented in Fig. 6.7 and will be discussed later.

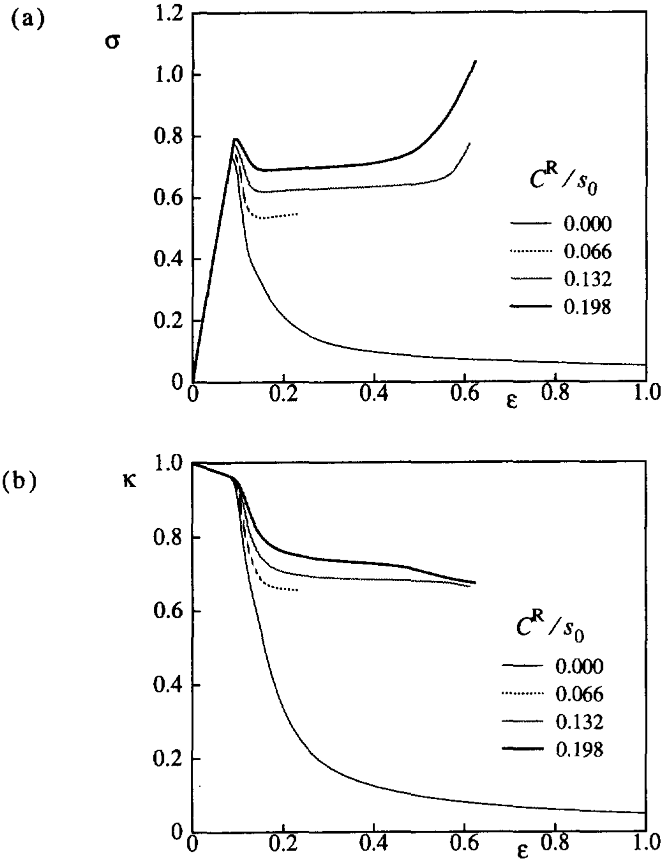

Fig. 6.8. Influence of the orientation hardening parameter C^R/s_0 on the predicted nominal stress response (a) and thickness-reduction ratio (b) under plane strain tension. All other parameters are as in Fig. 6.2.

The parameters N and C^R govern the orientation hardening through the non-Gaussian network model (6.6). In Fig. 6.8, we study the effect of orientation hardening by first using the same value of N ($N = 2.8$) but different values of C^R: $C^R/s_0 = 0.066$, 0.132, and 0.198, respectively. Furthermore, we include a limiting case of no orientation hardening by taking $C^R/s_0 = 0$. It is clear from the predicted nominal stress response that a larger value of C^R/s_0 increases the stiffness of the network and therefore increases the orientation hardening. The value of C^R/s_0 is observed to affect the maximum load too. The reason for this is that when the specimen reaches the maximum load state at an applied elongation $\varepsilon \approx 0.1$, significant plastic deformation has already occurred at some locations due to the intrinsic inhomogeneity of deformation. If C^R is large, orientation hardening will be already significant at that moment, resulting in a noticeable increase of the maximum load.

The effect of orientation hardening on the initiation of necking and neck propagation is also illustrated in Fig. 6.8b in terms of the predicted thickness-reduction ratio κ at the minimum section $x = 0$. It is observed that the larger value of C^R/s_0, the smaller the minimum normalized thickness $\kappa_{\min}$. It seems that the main effect of orientation hardening on neck localization and neck propagation shown in Fig. 6.8b is to shift the normalized thickness elongation curve vertically without changing its shape.

The predicted deformed meshes at various deformation stages with large value of $C^R/s_0 = 0.198$ are found to be similar to those shown in Fig. 6.3. The deformed meshes at various deformation stages obtained with $C^R/s_0 = 0$ (i.e. no orientation hardening) are given in Fig. 6.9. It is found that the initiated neck does not propagate as we observed in the cases with a positive value of C^R/s_0, but localizes progressively with further elongating (Figs. 6.9b and c). The strain is concentrated in the neck area, as is seen from the deformed meshes in Figs. 6.9b and c, while strains outside the neck region remain almost constant or even slightly decrease. This is also the reason why the predicted nominal stress continues to decrease at large elongations, as shown in Fig. 6.8a. Contour plots of plastic strain rate at various stages of the deformation also show no evidence of shear bands in the limiting case of no orientation hardening. In the case of small orientation hardening ($C^R/s_0 = 0.066$), the neck is found to propagate along the specimen but very slowly. All these results indicate that the orientation hardening is the driving force to promote neck propagation along the specimen.

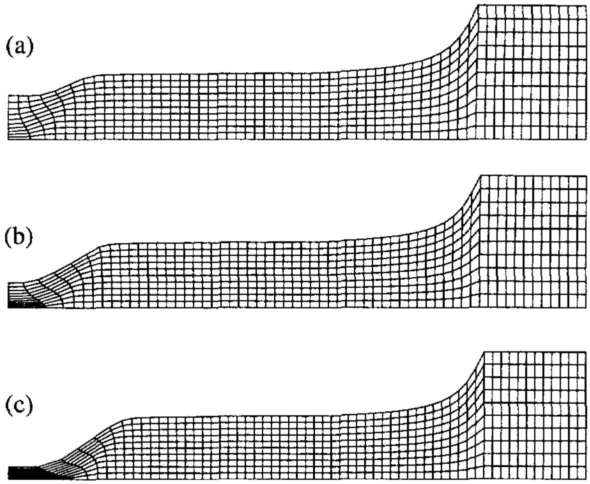

Fig. 6.9. Deformed meshes for $C^R/s_0 = 0$ at various deformation stages: (a) $\varepsilon = 0.13$, (b) $\varepsilon = 0.19$, (c) $\varepsilon = 0.28$. All figures are scaled to the same apparent specimen length.

We have also studied the effects of orientation hardening by using the same value of C^R ($C^R/s_0 = 0.132$) but different values of N: $N = 2.8, 4.2$ and 5.6. It was found that the effect of N on the overall response to plane strain tension of amorphous glassy polymers is not very strong, except for the fact that the limit stretches are reached at different elongation levels.

So far, we have studied the effect of intrinsic softening by using the same values of orientation hardening parameter $C^R/s_0 = 0.132$ and $N = 2.8$ but different values of the intrinsic softening parameter s_{ss}/s_0; and the effect of orientation hardening by using the same value of intrinsic softening parameter $s_{ss}/s_0 = 0.79$ but different values of the orientation hardening parameters C^R/s_0 and N. However, it is well-known that both intrinsic softening and geometric softening (reduction of the cross sectional area) affect the softening observed in the load-elongation curve in plane strain tension. Furthermore, the value of C^R/s_0 is observed to affect the apparent softening too. In order to further determine the effect of intrinsic softening on necking and neck propagation, we will consider here a material without intrinsic softening, but with different values of orientation hardening: $C^R/s_0 = 0.033$, and 0.132. The predicted overall responses are presented in Fig. 6.10 in terms of nominal stress σ and the thickness-reduction ratio κ. It is found that, as also demonstrated in Fig. 6.6a, in the case of larger orientation hardening ($C^R/s_0 = 0.132$), the orientation hardening effect suspends the geometric softening effect and excludes the apparent softening in the nominal stress-elongation curve. In this case there is no clear evidence of necking nor of neck propagation along the specimen as demonstrated before; also there is no indication of shear bands (see Fig. 6.7). In the case of smaller orientation hardening ($C^R/s_0 = 0.033$), there is an apparent softening in the nominal stress-elongation curve.

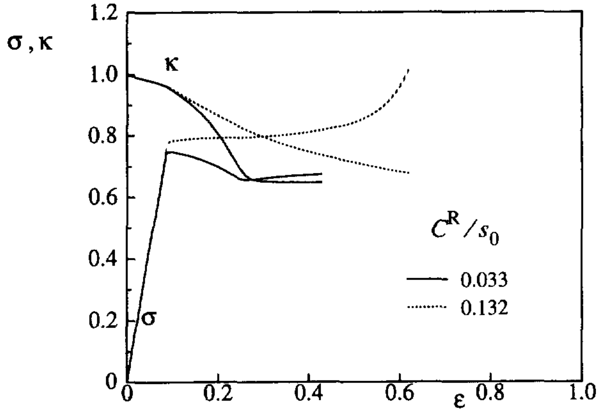

Fig. 6.10. Influence of the orientation hardening parameter C^R/s_0 on the predicted nominal stress response and thickness-reduction ratio under plane strain tension for a material without intrinsic softening ($s_{ss}/s_0 = 1$). All other parameters are as in Fig. 6.2.

Figure 6.11 shows the distributions of normalized plastic strain rate in the specimen with smaller orientation hardening ($C^R/s_0 = 0.033$) at various stages of the deformation. Comparing Fig. 6.11 with Fig. 6.4 and Fig. 6.7, it is seen that, at low elongations, the contours in the case without intrinsic softening but with a small apparent softening in nominal stress-elongation curve (Fig. 6.11) are similar to those in the case of no intrinsic softening nor apparent softening (Fig. 6.7); while at high elongations, the plastic strain rate distribution in the case without intrinsic softening but with a small apparent softening (Fig. 6.11) is roughly similar to that in the case with both intrinsic and apparent softening (Fig. 6.4). At large elongations and with apparent softening, the precise shear band patterns are different when comparing the cases with intrinsic softening (Fig. 6.4) and without intrinsic softening (Fig. 6.11). First of all, it is noted that the localization of deformation into what we call shear bands, in the case without intrinsic softening is significantly less pronounced than in the case with intrinsic softening. Furthermore, the main shear band in the case without intrinsic softening is oriented at an angle large than 90° with respect to the loading direction.

Fig. 6.11. Contours of normalized plastic strain rate $\dot{\Sigma}^p$ in the case of no intrinsic softening but with an apparent softening under plane strain tension at various deformation stages: (a) $\varepsilon = 0.09$, (b) $\varepsilon = 0.16$, (c) $\varepsilon = 0.30$, (d) $\varepsilon = 0.43$. All figures are scaled to the same apparent specimen length.

It is well-known that flow in amorphous glassy polymers is a viscous process and the yield stress is strongly strain-rate dependent. Figure 6.12 shows the overall responses to plane strain tension deformation at normalized applied strain-rates $\dot{\varepsilon}/(\sqrt{3}\dot{\gamma}_0)$ ranging over several orders of magnitude. The increase of the maximum load due to an increase of the strain rate is seen to be small, about 7% for one decade of strain-rate. It seems that the main effect of strain-rate is to shift the nominal stress elongation curve vertically without changing its shape, while the thickness-reduction ratio κ is found to be insensitive to the strain rate. The differences in deformed meshes and the distributions of normalized plastic strain rate under different strain-rates are found to be small, so that it is concluded that the initiation of neck and neck propagation are not sensitive to strain-rate within the range considered.

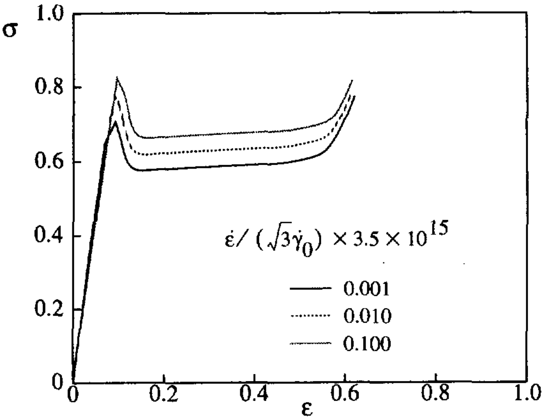

Fig. 6.12. Influence of the normalized applied strain-rate $\dot{\varepsilon}/(\sqrt{3}\dot{\gamma}_0)$ on the predicted nominal stress response under plane strain tension. All other parameters are as in Fig. 6.2.

6.4.4. *Effects of geometry and boundary condition*

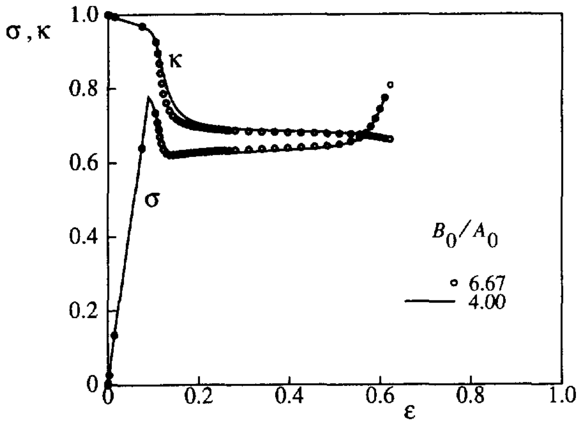

Fig. 6.13. Influence of the aspect ratio B_0/A_0 of the specimen's gauge section on the predicted nominal stress response and the thickness-reduction ratio under plane strain tension. The material parameters are as in Fig. 6.2.

From the point view of experiments, detailed analysis of the effects of specimen geometry and boundary conditions on the overall stress strain response and on the necking behaviour is of practical importance. We first study the effect of geometry of the specimen on the overall response in terms of nominal stress σ and thickness-reduction ratio κ. The numerical results with $B_0/A_0 = 4$ and 6.67 but with the same values of L_0/B_0, L_e/L_0, H_0/A_0 and Q are presented in Fig. 6.13. In the case of $B_0/A_0 = 6.67$ a regular mesh consisting of 16×90 elements is used. We have also analysed neck localization and propagation in terms of deformed meshes. It is observed that the effect of geometry on the initiation of necking and neck propagation is very small within the considered range of B_0/A_0.

Figure 6.14 shows the predicted overall responses to plane strain tension with different boundary conditions, namely shear-free ends and gripped ends. For the specimen with gripped ends, the rate boundary conditions at $x = L_0$ become

$$\dot{u}_x(L_0, y) = \dot{U}, \qquad \dot{u}_y(L_0, y) = 0 \tag{6.20}$$

instead of (6.14) and the boundary conditions at $x = 0$ are same as in (6.15), while the lateral surfaces of the specimen are also taken to be stress-free.

We have also plotted the deformed meshes and distributions of plastic strain rate at various deformation stages. It is found that with the shape of the specimen considered here, boundary conditions have a negligible effect on necking and neck propagation. In fact, we hardly see the effect of boundary condition on the overall response in terms of nominal stress σ and thickness-reduction ratio κ in Fig. 6.14. It is obvious that this is not true for a prismatic specimen.

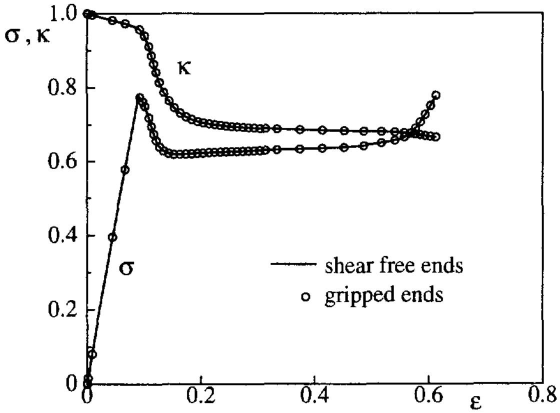

Fig. 6.14. Influence of the boundary conditions on the predicted nominal stress response and thickness-reduction ratio under plane strain tension. The material parameters are as in Fig. 6.2.

6.5. DISCUSSION AND CONCLUSION

In this chapter, 3-D constitutive model for large strain inelastic deformation of amorphous glassy polymers has been incorporated in finite element computations of a plane strain tension, focusing attention on the initiation of necking and neck propagation along the specimen. Results have been given for the overall load-elongation response and the thickness reduction-elongation response of the specimen. The effects of initial imperfection, strain softening, orientation hardening, strain-rate as well as the influences of geometry and boundary condition have been discussed in detail.

The predicted results have shown that the constitutive model is able to pick up qualitatively the four successive stages of the experimental force-elongation curve. The experimentally observed initiation of necking and neck propagation have also been predicted well qualitatively.

An important problem in polymer science and technology is to understand what are the driving factors that control the kinetics of necking and neck propagation. By incorporating the 3-D constitutive model of 6.2 in finite element simulations of the plane strain tension of amorphous glassy polymers, the parameter study performed here should be helpful in improving the understanding of the mechanisms of necking and neck propagation. In the simulations of shear band propagation in simple shear tests, Wu and Van der Giessen (1993d) concluded that the intrinsic softening is the driving force to promote initiation of the shear band and its propagation in the shear direction, while the orientation hardening is the driving force for widening of the shear band. The results presented here lead to concluding that for the adopted constitutive model, the orientation hardening is the driving force to promote neck propagation along the specimen. Is the intrinsic softening the driving force to promote the initiation of necking in plane strain tension too?

Details aside, it is well-known that necking in elastoplastic prismatic plane strain bars essentially coincides with a maximum in the load (or nominal stress) versus elongation curve. Even though our specimen is not prismatic, our results support the conclusion that a maximum followed by apparent softening in the nominal stress-elongation curve is necessary and sufficient for the initiation of necking. Our numerical results also demonstrate that intrinsic softening, geometric softening and orientation hardening determine, in a competitive way, whether or not apparent softening appears. In one of the cases presented, there was no intrinsic softening, but apparent softening occured; this supports the conclusion that intrinsic softening is a sufficient condition for necking, but not necessary.

For all material parameter combinations where we found necking, we observed what we called 'shear bands' in the propagating necked region. It is of interest to note that these bands were also observed in the absence of intrinsic softening, even though shear bands are commonly associated with a true material instability. However, the localization of deformation in those bands was less intense than when the material showed intrinsic softening, so that the terminology 'shear band' becomes somewhat questionable. All these aspects require further study, both experimentally and numerically, and both macroscopically and microscopically.

Concerning the constitutive aspects, it is noted that we used the affine network theory to model orientational hardening. The idea of using an affine network theory to model the stretching of the molecular network assumes that the junction points in the network remain in tact. However, it has been suggested in the literature [see e.g. Raha and Bowden (1972) and Botto *et al.* (1987)] that physical entanglements in amorphous polymers are being pulled out during deformation. In terms of our network model this would mean that the number of chains n reduces in the course of the deformation process, while the number of links N per chain increases, thus reducing the stiffness of the network. Also it cannot be ruled out that at large deformations, when chains are rotated towards a common axis to such an extent that they become lined up, intermolecular interactions are no longer negligible. Molecular dynamics simulations (Gao and Weiner, 1991) seem to indicate that this may be a significant effect already at relatively small deformation of the molecular chains in the Gaussian regime, and it may be expected to be even more important at the large strain levels in cold drawing considered here. All these constitutive aspects require further study.

Appendix

Here we give a brief summary of the central governing equations of the special element used in the torsion analysis in Chapter 4 (see Fig. 4.1b).

The radial velocity at a point $\xi \in [-1, 1]$ within the element is determined by a linear interpolation of $\dot{r}/r$:

$$\frac{\dot{r}}{r} = \frac{1}{2}(1-\xi)\frac{\dot{r}_1}{r_1} + \frac{1}{2}(1+\xi)\frac{\dot{r}_2}{r_2} \qquad \text{(A1)}$$

$$r = \frac{1}{2}(1-\xi)r_1 + \frac{1}{2}(1+\xi)r_2 \qquad \text{(A2)}$$

Within each element, two sampling points (Van der Giessen, 1987) are introduced at locations specified by $\xi_{\mathrm{I}} = -\sqrt{3}/3 \ (r = r_{\mathrm{I}})$ and $\xi_{\mathrm{II}} = \sqrt{3}/3 \ (r = r_{\mathrm{II}})$, respectively (these locations coincide with the 1-D Gaussian integration points). Each sampling point is attributed a volume fraction $\upsilon = r/(r_1 + r_2)$, and we define the vectors of generalized element strain-rates and stresses by,

$$\dot{\mathbf{E}} = \left[D^{\mathrm{I}}_{11}\ D^{\mathrm{I}}_{22}\ 2D^{\mathrm{I}}_{23}\ D^{\mathrm{I}}_{33}\ D^{\mathrm{II}}_{11}\ D^{\mathrm{II}}_{22}\ 2D^{\mathrm{II}}_{23}\ D^{\mathrm{II}}_{33}\right]^T, \qquad \text{(A3)}$$

$$\mathbf{\Sigma} = V^{\mathrm{e}}\left[\upsilon_{\mathrm{I}}\sigma^{\mathrm{I}}_{11}\ \upsilon_{\mathrm{I}}\sigma^{\mathrm{I}}_{22}\ \upsilon_{\mathrm{I}}\sigma^{\mathrm{I}}_{23}\ \upsilon_{\mathrm{I}}\sigma^{\mathrm{I}}_{33}\ \upsilon_{\mathrm{II}}\sigma^{\mathrm{II}}_{11}\ \upsilon_{\mathrm{II}}\sigma^{\mathrm{II}}_{22}\ \upsilon_{\mathrm{II}}\sigma^{\mathrm{II}}_{23}\ \upsilon_{\mathrm{II}}\sigma^{\mathrm{II}}_{33}\right]^T, \qquad \text{(A4)}$$

where $V^{\mathrm{e}} = \pi(r_2^2 - r_1^2)L$. For quasistatic deformations, the principle of virtual power states for each of these elements in the current configuration that:

$$V^{\mathrm{e}}[\upsilon_{\mathrm{I}}\boldsymbol{\sigma}_{\mathrm{I}} \cdot \mathbf{D}_{\mathrm{I}} - \upsilon_{\mathrm{II}}\boldsymbol{\sigma}_{\mathrm{II}} \cdot \mathbf{D}_{\mathrm{II}}] = \mathbf{\Sigma}^T\dot{\mathbf{E}} = \mathbf{F}^T\mathbf{V}.$$

It then follows from (A4) with (4.14), along with the principal of virtual power, that:

$$\dot{\mathbf{E}} = \mathbf{D}^T\mathbf{V}, \qquad \mathbf{D}^T\mathbf{\Sigma} = \mathbf{F}, \qquad \text{(A5)}$$

where

$$\mathbf{D} = \left[\mathbf{D}_{\mathrm{I}}\ \mathbf{D}_{\mathrm{II}}\right]^T, \qquad \text{(A6)}$$

$$\mathbf{D}_K = \begin{bmatrix} -(\zeta_K + r_1/b) & (\zeta_K + r_2/b) & 0 & 0 \\ \frac{1}{2}(1-\xi_K)\, r_K^2 & \frac{1}{2}(1+\xi_K)\, r_K^2 & 0 & 0 \\ 0 & 0 & r_K^2/L & 0 \\ 0 & 0 & 0 & 1 \end{bmatrix}; \qquad K = \mathrm{I}, \mathrm{II}, \tag{A7}$$

with $b = r_2 - r_1$.

The rate equations are derived by straightforward time differentiation of the equilibrium conditions (A5). Here it may be noted that due to the particular interpolation of the radial velocity field through (A1), the sampling points do not coincide with material points; but this difference may be neglected when the elements are sufficiently small and the total change of the radius of the bar remains small as compared with the initial outer radius R_{00}. After elimination of the stress rates which appear after differentiation by means of the constitutive relations (4.8), followed by elimination of the strain-rates by means of (A5), the finite element equations are found of the form

$$\mathbf{K}\mathbf{V} = \dot{\mathbf{F}} + \dot{\mathbf{F}}_{\mathrm{v}}, \tag{A8}$$

with

$$\mathbf{K} = \mathbf{D}^T \mathbf{S} \mathbf{D} + \mathbf{G}, \tag{A9}$$

$$\dot{\mathbf{F}}_{\mathrm{v}} = \mathbf{D}^T \dot{\boldsymbol{\Sigma}}_{\mathrm{v}}. \tag{A10}$$

Here, the matrix $\mathbf{S}$ is determined by the elastic moduli in the constitutive law (4.8). Due to symmetry of these moduli, the matrix is $\mathbf{S}$ symmetric. The matrix $\mathbf{G}$ contains contributions from the geometry dependence of the matrix $\mathbf{D}$ in the equilibrium equations (A5) as well as a contribution from the convective terms appearing in the Jaumann derivative of $\boldsymbol{\sigma}$, in (4.7) or (4.8). It is noted that this $\mathbf{G}$ matrix and, as a consequence, the $\mathbf{K}$ matrix are nonsymmetric; however, the final simple structure of the matrix $\mathbf{K}$ allows for a simple and efficient solution procedure. Furthermore, in (A10), $\dot{\boldsymbol{\Sigma}}_{\mathrm{v}}$ is defined in terms of the stress-rate $\dot{\boldsymbol{\sigma}}_{\mathrm{v}}$ completely similar to $\boldsymbol{\Sigma}$.

References

Anand, L. (1979). On H. Hencky's approximation strain-energy function for moderate deformation. *J. Appl. Mech.* **46**, 78-82.

Argon, A.S. (1973). A theory for the low-temperature plastic deformation of glassy polymers. *Phil. Mag.* **28**, 839–865.

Arruda, E.M. and Boyce, M.C. (1991). Evolution of plastic anisotropy in amorphous polymers during finite straining. In *Anisotropy and Localization of Plastic Deformation.* (Edited by J.-P. Boehler and A.S. Khan), pp. 483-488, Elsevier Applied Science, London.

Arruda, E.M. and Boyce, M.C. (1992). The anisotropy of large deformation in glassy polycarbonate. In: *Modelling of Plastic Deformation and its Engineering Applications.* (Edited by S.I. Andersen *et al.*), pp. 181-188, Roskilde, Denmark.

Arruda, E.M. and Boyce, M.C. (1993a). A three-dimensional constitutive model for large stretch behaviour of rubber materials. *J. Mech. Phys. Solids* **41**, 389-412.

Arruda, E.M. and Boyce, M.C. (1993b). Evolution of plastic anisotropy in amorphous polymers during finite straining. *Int. J. Plast.* **9**, 697-720.

Bailey, J.A., Haas, S.L. and Nawab, K.C. (1972). Anisotropy in plastic torsion. J. *Basic Engrg.* **94**, 231-237.

Ball, R.C., Doi, M., Edwards, S.F. and Warner, M. (1981). Elasticity of entangled network. *Polymer* **22**, 1010-1018.

Batterman, S.D. and Bassani, J.L. (1990). Yielding, anisotropy, and deformation processing of polymers. *Polym. Engng. Sci.* **30**, 1281-1287.

Besseling, J.F. and Van der Giessen, E. (1993). *Mathematical Modelling of Inelastic Deformation.* Chapman & Hall, London.

Billington, E.W. (1977). Non-linear response of various metals: II. Permanent length changes in twisted tubes. *J. Phys. D: Appl. phys.* **10**, 533-552.

Botto, P.A., Duckett, R.A. and Ward, I.M. (1987). The yield and thermoelastic properties of oriented poly (methyl methacrylate). *Polymer* **28**, 257-262.

Bowden, P.B. (1973). The yield behaviour of glassy polymers. In *The Physics of Glassy Polymers.* (Edited by R.N. Haward), pp.279-339, Applied Science Publishers, Essex.

Boyce, M.C. and Arruda, E.M. (1990). An experimental and analytical investigation of the large strain compressive and tensile response of glassy polymers. *Polym. Engng. Sci.* **30**, 1288-1298.

Boyce, M.C., Parks, D.M. and Argon, A.S. (1988). Large inelastic deformation of glassy polymers, Part I: rate dependent constitutive model. *Mech. Mater.* **7**, 15–33.

Boyce, M.C., Parks, D.M. and Argon, A.S. (1989). Plastic flow in oriented glassy polymers. *Int. J. Plast.* **5**, 593-615.

Brown, D.J. and Windle, A.H. (1984). Stress-orientation-strain relationships in non-crystalline polymers, Part 1. Strategy for a model. *J. Mat. Sci.* **19**, 1997-2012.

Buisson, G. and Ravi-Chandar, K. (1990). On the constitutive behaviour of polycarbonate under large deformation. *Polymer* **31**, 2071-2076.

Chadwick, P. and Creasy, C.F.M. (1984). Modified entropic elasticity of rubberlike materials. *J. Mech.*

Phys. Solids **32**, 337-357.

Coleman, B.D. (1983). Necking and drawing in polymeric fibres under tension. *Arch. Rat. Mech. Analy.* **83**, 115-137.

Dahoun, A. (1992). *Comportement Plastique et Textures de Deformation des Polymers Semi-crystallines en Traction Uniaxiale et en Cisaillement Simple.* Ph.D. Thesis, Institut National Polytechnique de Lorraine, Nancy, France.

Dahoun, A., G'Sell, C., Molinari, A. and Canova, G.R. (1993). Plastic behaviour and deformation textures of poly(ether ether ketone) under uniaxial tension and simple shear. (submitted for publication).

Doherty, O.S., Lee, K.L. and Treloar, L.R.G. (1980). Non-Gaussian effects in styrene-butadiene rubber. *Brit. Polym. J.* **12**, 19-23.

Duckett, P.A., Rabinowitz, S. and Ward, I.M. (1970). The strain-rate, temperature and pressure dependence of yield of isotropic poly(methylmethacrylate) and poly(ethylene terephthalate). *J. Mat. Sci.* **5**, 909-915.

Eyring, H. (1936). Viscosity, plasticity, and diffusion as examples of absolute reaction rates. *J. Chem. Phys.*, **4**, 283-291.

Fager, L.O. and Bassani, J.L. (1986). Plane strain neck propagation. *Int. J. Solids Structures* **22**, 1243-1257.

Ferry, J.D. (1980). *Viscoelastic Properties of Polymers.* Wiley, New York.

Flory, P.J. (1944). Network structure and the elastic properties of vulcanized rubber. *Chem. Rev.*, **35**, 51-75.

Flory, P.J. and Rehner, J. (1943). Statistical mechanics of cross-linked polymer networks. *J. Chem. Phys.* **11**, 512-520.

Gao, J. and Weiner, J.H. (1991). Chain force concept in systems of interacting chains, *Macromolecules* **24**, 5179-5191

Gil-Sevillano, J., Van Houtte, P. and Aernoudt, E. (1975). Deutung der schertexturen mit hilfe der Taylor-analyse. *Z. Metallkunde* **66**, 367-373.

Gopez, A.J. (1983). *Étude de la Déformation du Polycarbonate en Cisaillement Simple.* Thèse d'Ingenieur, CNAM, Nancy, France.

Grenet, J. and G'Sell, C. (1990). Observation and modelling of shear-band propagation in glassy polycarbonate. *Polymer* **31**, 2057-2065.

G'Sell, C. (1986). Plastic deformation of glassy polymers: Constitutive equations and macromolecular mechanisms. In *Strength of Metals and Alloys.* (Edited by H.J. McQueen *et al.*), pp. 1943-1982, Pergamon Press, Oxford.

G'Sell, C., Aly-Helal, N., Semiatin, S.L. and Jonas, J.J. (1992). Influence of deformation defects on the development of strain gradients during the tensile deformation of polyethylene, *Polymer* **33**, 1244-1254.

G'Sell, C., Boni, S. and Shrivastava, S. (1983). Application of the plane simple shear test for determination of the plastic behaviour of solid polymers at large strains. *J. Mat. Sci.* **18**, 903-918.

G'Sell, C. and Dahoun, A. (1993). Evolution of microstructure in semi-crystalline polymers under large plastic deformation. *Mat. Sci. Engng.* (submitted for publication).

G'Sell, C. and Gopez, A.J. (1985). Plastic banding in glassy polycarbonate under plane simple shear. *J. Mat. Sci.* **20**, 3462–3478.

G'Sell, C. and Jonas, J.J. (1979). Determination of the plastic behaviour of solid polymers at constant true strain rate. *J. Mat. Sci.* **14**, 583-591.

G'Sell, C. and Marquez-Lucero, A. (1993). Determination of the intrinsic stress/strain equation of thin polymer films from stretching experiments under plane-strain tension. *Polymer* **34**, 2740-2749.

Harren, S., Lowe, T.C., Asaro, R.J. and Needleman, A. (1989). Analysis of large-strain shear in rate-dependent face-centered cubic polycrystals: Correlation of micro- and macromechanics. *Proc. R.*

Soc. Lond. **A328**, 443-500.

Haward, R.N. (1980). The effect of chain structure on the annealing and deformation behaviour of polymers. *Coll. Poly. Sci.* **258**, 643-661.

Haward, R.N. and Thackray, G. (1968). The use of a mathematical model to describe isothermal stress-strain curves in glassy thermoplastics. *Proc. R. Soc. Lond.* ***A302***, 453–472.

Hutchinson, J.W. and Neale, K.W. (1983). Neck propagation. *J. Mech. Phys. Solids* **31**, 405-426.

James, A.G., Green, A. and Simposon, G.M. (1975). Strain energy function of rubber. I. Characterization of gun vulcanizes. *J. appl. Polymer Sci.* **19**, 2033-2058.

James, H.M. and Guth, E. (1943). Theory of the elastic properties of rubber. *J. Chem. Phys.* **11**, 455-481

Khen, R. and Rubin, M.B. (1992). Analytical modelling of second order effects in large deformation plasticity. *Int. J. Solids Structures* **29**, 2235-2258.

Kuhn, W. and Grun, F. (1942). Beziehuugen zwischen elastischen konstanten uud dehuungsdoppelbrechung hochelastischer stoffe. *Kolloidzeitschrift* **101**, 248-271.

Lee, E.H. (1969). Elastic-plastic deformation at finite strains. *J. Appl. Mech.* **36**, 1-6.

Li, J.C.M. and Gilman, J.J. (1970). Disclination loops in polymers. *J. Appl. Phys.* 41, 4248-4256.

Mark, J.E. and Erman, B. (1988). *Rubberlike Elasticity: A Molecular Primer.* Wiley, New York.

Marquez-Lucero, A., G'Sell, C. and Neale, K.W. (1989). Experimental investigation of neck propagation in polymers. *Polymer* **30**, 636-642.

Mitchell, G.R., Brown, D.J. and Windle, A.H. (1985). The interpretation of orientation-strain relationships in rubbers and thermoplastics. *Polymer* **26**, 1755-1762.

Meijer, H.E.H. (1993). Private communication.

Neale, K.W. and Shrivastava, S.C. (1985). Finite elastic-plastic torsion of a circular bar. *Engng. Fracture Mech.* **21**, 747-754.

Neale, K.W. and Shrivastava, S.C. (1990). Kinematic work hardening models and their implications for large strain plastic behaviour in torsion. In *Yielding, Damage and Failure of Anisotropic Solids* (Edited by J.P. Boehler), pp. 131-143, Mechanical Engineering Publications, London.

Neale, K.W. and Tugcu, P. (1985). Analysis of necking and neck propagation in polymeric materials. *J. Mech. Phys. Solids* **33**, 323-337.

Needleman, A. (1988).Material rate dependence and mesh sensitivity in localization problems. *Comp. Meth. Appl. Mech. Engrg.* **67**, 69-85.

Needleman, A. and Tvergaard, V. (1984). Finite element analysis of localization in plasticity. In *Finite Elements, Special Problems in Solid Mechanics.* (Edited by J.T. Oden and G.F. Carey), **Vol. V**, pp. 94-157, Prentice-Hall.

Ogden, R.W. (1984). *Non-linear Elastic Deformations.* Ellis Horwood Ltd., Chichester.

Peirce, D., Shih, C.F. and Needleman, A. (1984). A tangent modulus method for rate dependent solids. *Comput. Struct.* **18**, 875-887.

Perez, J. (1982). Deformation models in metallic polymeric glassy. In *Plastic Deformation of Amorphous and Semi-crystalline Materials.* (Edited by C. G'Sell and B. Escaig), pp. 265-285.

Raha, S. and Bowden, P.B. (1972). Birefringence of plastically deformed poly (methyl methacrylate). *Polymer* **13**, 174-183.

Rice, J.R. (1977). The localization of plastic deformation. In *Theoretical and Applied Mechanics.* (Edited by W.T. Koiter), pp. 207-220, North-Holland Publishing Company.

Robertson, R. (1966). Theory for the plasticity of glassy polymers. *J. Chem. Phys.*, **44**, 3950-3956.

Struik, L.C.E. (1990). *Internal Stresses, Dimensional Instabilities and Molecular Orientations in Plastics.* Wiley-Inter-Science, Chichester.

Swift, W. (1947). Length changes in metals under torsional overstrain. *Engineering* **163**, 253-257.

Tomita, Y., Takahashi, T. and Shindo, A. (1990). Necking and bulge propagation in polymeric cylinders. *Int J. Mech. Sci.* **32**, 335-343.

Treloar, L.R.G. (1944). Stress-strain data for vulcanized rubber under various types of deformation.

Trans. Faraday Soc. **40**, 59-70.

Treloar, L.R.G. (1946). The elasticity of a network of long-chain molecules.—III. *Trans. Faraday Soc.* **42**, 83-94.

Treloar, L.R.G. (1975). *Physics of Rubber Elasticity* (3rd edn). Oxford University Press.

Treloar, L.R.G. and Riding, G. (1979a). A non-Gaussian theory for rubber in biaxial strain. I. Mechanical properties. *Proc. R. Soc. Lond.* *A***369**, 261-280.

Treloar, L.R.G. and Riding, G. (1979b). A non-Gaussian theory for rubber in biaxial strain. II. Optical properties. *Proc. R. Soc. Lond.* *A***369**, 281-293.

Tugcu, P. and Neale, K.W. (1987a). Necking and neck propagation in polymeric materials under plane strain tension. *Int. J. Solids Structures* **213**, 1063-1085.

Tugcu, P. and Neale, K.W. (1987b). Analysis of plane-strain neck propagation in viscoplastic polymeric films. *Int. J. Mech. Sci.* **29**, 793-805.

Tugcu, P. and Neale, K.W. (1988). Analysis of neck propagation in polymeric fibers including the effect of viscoplasticity. *Trans. ASME, J. Engng. Mater. Tech.* **110**, 395-400.

Tvergaard, V., Needleman, A. and Lo, K.K. (1981). Flow localization in the plane strain tensile test. *J. Mech. Phys. Solids* **29**, 115-142.

Van der Giessen, E. (1987). FE-thermomechanics and material sampling points. *Comput. Meth. Appl. Mech. Engrg.* **64**, 447-465.

Van der Giessen, E. (1991). Some remarks on the analysis of large strain torsion-like problems. *Acta Mech.* **89**, 233-239.

Van der Giessen, E. and Neale, K.W. (1993). Analysis of the inverse Swift effect using a rate-sensitive polycrystal model. *Comp. Meth. Appl. Mech. Engng.* **103**, 291-313.

Van der Giessen, E., Wu, P.D. and Neale, K.W. (1992a). On the effect of plastic spin on large strain elastic-plastic torsion of solid bars. *Int. J. Plast.* **8**, 773-801.

Van der Giessen, E., Wu, P.D. and Neale, K.W. (1992b). Effect of plastic spin and deformation-induced anisotropy on large strain torsion of solid bars. In *Constitutive Relations for Finite Deformation of Polycrystalline Metals* (Edited by R. Wang and D.C. Drucker), pp. 233-248, Springer Verlag, Beijing/Berlin.

Vest, T.A., Amoedo, J. and Lee, D. (1987). Modeling of tensile stress strain behaviour in semi-crystalline and amorphous polymers. In *Constitutive Modeling for Nontraditional Materials* (Edited by V. Stokes and D. Krajcinovic), pp.71-85, ASME, New York.

Wang, M.C. and Guth, E. (1952). Statistical theory of networks of non-Gaussian flexible chains. *J. Chem. Phys.* **20**, 1144–1157.

Wang, T.T., Zupko, H.M., Wyndon, L.A. and Matsuoko, S. (1982). Dimensional and volumetric changes in cylindrical rods of polymers subjected to a twist moment. *Polymer* **23**, 1407-1409.

Ward, I.M. (1983). *Mechanical Properties of Polymers* (2nd edn). Wiley-Inter-Science, Chichester.

White, C.S., Bronkhorst, C.A. and Anand, L. (1990). An improved isotropic-kinematic hardening model for moderate deformation metal plasticity. *Mech. Mater.* **10**, 127-147.

Wu, P.D., Neale, K.W. and Van der Giessen, E. (1993). Large strain torsion of axially-constrained solid rubber bars. *Acta Mechanica Sinica* (in print).

Wu, W. and Turner, A.P.L. (1973). Shear bands in polycarbonate. *J. Polym. Sci.: Polym. Phys. Edition* **11**, 2199-2208.

Wu, P.D. and Van der Giessen, E. (1991a). Analysis of elastic-plastic torsion of circular bars at large strains. *Arch. Appl. Mech.* **61**, 89-103.

Wu, P.D. and Van der Giessen, E. (1991b). On large inelastic deformations of amorphous glassy polymers. Delft University of Technology, Lab. for Engng. Mech. Report no. 936.

Wu, P.D. and Van der Giessen, E. (1992a). On improved 3-D non-Gaussian network models for rubber elasticity. *Mech. Res. Comm.* **19**, 427-433.

Wu, P.D. and Van der Giessen, E. (1992b). A modified 3-D constitutive model for glassy polymers and its application to large simple shear of polycarbonate. In *Modelling of Plastic Deformation and its Engineering Applications.* (Edited by S.I. Andersen *et al.*), pp. 519-524, Roskilde, Denmark.

Wu, P.D. and Van der Giessen, E. (1993a). On improved network models for rubber elasticity and their applications to orientation hardening in glassy polymers. *J. Mech. Phys. Solids* **41**, 427-456.

Wu, P.D. and Van der Giessen, E. (1993b). Large strain visco-plastic torsion of circular bars of glassy polymers. In *Advances in Engineering Plasticity and its Applications.* (Edited by W.B. Lee), pp. 477-484, Elsevier Science Publishers B.V., Amsterdam.

Wu, P.D. and Van der Giessen, E. (1993c). On large strain inelastic torsion of glassy polymers. *Int. J. Mech. Sci.* **35**, 935-951.

Wu, P.D. and Van der Giessen, E. (1993d). Analysis of shear band propagation in amorphous glassy polymers. *Int. J. Solids and Structures* (in print).

Wu, P.D. and Van der Giessen, E. (1993e). On network descriptions of mechanical and optical properties of rubbers. *Phil. Mag.* (submitted for publication).

Wu, P.D. and Van der Giessen, E. (1993f). On neck propagation in amorphous glassy polymers under plane strain tension. *Int. J. Plast.* (submitted for publication).

Zbib, H.M., Shawki, T.G. and Batra, R.C. (eds.) (1992). *Material Instabilities, Appl. Mech. Rev.* **45**, no. 3, part 2.

Ziegler, H. (1977). *An Introduction to Thermomechanics.* North-Holland, Amsterdam.

SAMENVATTING

Dit proefschrift handelt over twee onderwerpen op het gebied van de constitutieve modelvorming van het gedrag van polymeermaterialen bij grote vervormingen, in het bijzonder grote elastische vervormingen van rubbers en grote niet-elastische vervormingen van amorfe glasachtige polymeren.

Allereerst worden theorieën voor drie-dimensionale molecuulnetwerken beschouwd die voor het elastische gedrag van de molecuulketens gebruik maken van modellen uit de niet-Gaussische statistische mechanica. Onder de aanname van affiene deformaties van het molecuulnetwerk wordt aangetoond dat de evolutie van het netwerk —bestaande uit een groot aantal molecuulketens per eenheid van volume met initieel willekeurige oriëntaties—wordt bepaald door een balansvergelijking in de orientatie-ruimte. Zowel Euler als Lagrange formuleringen van de balansvergelijking worden gegeven, en de analytische oplossing voor de zgn. Keten Orientatie Distributie Functie wordt afgeleid in gesloten vorm. Dit netwerkmodel wordt vervolgens gebruikt voor de constitutieve beschrijving van grote elastische vervormingen van rubbers. De resultaten worden voor verschillende typen vervormingen in detail vergeleken met experimentele gegevens, en tevens met twee benaderingsmodellen, t.w. het klassieke drie-keten model en het zeer recent voorgestelde acht-keten model.

Vervolgens wordt het netwerkmodel voor rubberelasticiteit opnieuw geformuleerd op een efficiëntere en meer micromechanica-gemotiveerde manier. Op basis van dit laatste netwerkmodel wordt een netwerkmodel voorgesteld voor foto-elastische rubbers waarin de individuele onvervormbare schakels in de keten gepolariseerd kunnen worden. Deze optische theorie kan gebruikt worden voor onderzoek naar de optische eigenschappen of naar de invloed van grote vervormingen op de dubbelbrekingsindex van rubbers in willekeurige driedimensionale vervormingstoestanden. De resultaten worden weer voor verschillende soorten vervormingen in detail vergeleken met experimentele gegevens, alsmede met het klassieke drie-keten model en het in dit proefschrift voorgestelde acht-keten model voor photoelastische rubbers.

Het netwerkmodel wordt vervolgens toegepast voor de modellering van het verstevigingsgedrag van amorfe glasachtige polymeren na vloei t.g.v. verstrekking van het entanglementnetwerk. Een driedimensionaal constitutieve model wordt voorgesteld voor het het niet-elastisch vervormingsgedrag van amorfe glasachtige polymeren bij grote vervormingen, waarbij tijds-, temperatuur- en drukafhankelijke vloei in rekening wordt gebracht, alsmede softening gevolgd door versteviging.

Eén van de toepassingen betreft de elastisch-viscoplastische torsie van cilindrische buizen bij grote vervormingen, zowel met ingeklemde als met vrije uiteinden. De oplossing van het probleem wordt numeriek verkregen door middel van eenvoudige, speciale eindige elementen. In het bijzonder wordt aandacht geschonken aan de verschillen in gedrag bij ingeklemde respectievelijk vrije uiteinden. De met behulp van het model berekende numerieke resultaten worden vervolgens vergeleken met experimentele waarden voor polycarbonaat uit de literatuur.

Koudtrekken, waarbij zich een insnoering door het materiaal voortplant, is een gangbare manier om polymeren te verstevigen. Eindige-elementenanalyse wordt toegepast voor de simulatie van éénassige trek bij vlakke vervorming, waarbij vooral aandacht wordt besteed aan de insnoering en de voortplanting ervan. De invloed van initiële imperfecties, intrinsieke softening, versteviging, vervormingssnelheid alsmede de geometrie en randvoorwaarden worden in detail besproken. Resultaten worden gegeven in de vorm van de algehele belastings-verlengingskromme en de diktereduktie- verlengingskromme van de responsie van het proefstuk. In enkele gevallen worden tevens de vervormde eindige elementen mazen en/of de verdelingen van de plastische reksnelheden gegeven. De mechanismen van het ontstaan van een insnoering en de voortplanting ervan worden in detail besproken op basis van een gedetailleerd parameteronderzoek.

Niet alleen bij trekbelasting doch ook bij afschuiving wordt vaak het ontstaan en de voortplanting van een afschuifband waargenomen. Eindige-elementenanalyse wordt toegepast voor de simulatie van eenvoudige afschuiving bij vlakke vervorming, waarbij weer vooral aandacht wordt besteed aan de afschuifband en de voortplanting ervan. De afhankelijkheid van de eindige-elementenmesh, initiële vormafwijkingen, softening, versteviging, reksnelheid alsmede de invloed van vrije randen van het proefstuk worden in detail besproken. Het blijkt dat de afschuifband en de voortplanting ervan in de richting van de afschuiving wordt veroozaakt door de inherente softening, terwijl de versteviging verantwoordelijk is voor de verbreding van de afschuifstrook loodrecht op de afschuifrichting. De numerieke resultaten worden weer vergeleken met experimentele waarden voor polycarbonaat uit de literatuur.